TU Delft

Master Thesis Project

MSc Marine Technology

Mastering Breaking Waves in the Multiphase Wave Lab at MARIN

Student:	Juan José Costas Brea
Professor:	Prof.Dr.ir. Jerry Westerweel
Daily supervisor:	Dr.-Ing. Sebastian Schreier (TU Delft)
Supervisor:	PdEng.ir. Vladimir Novakovic (TU Delft/MARIN)
3rd member:	Dr.ir. Arthur Vrijdag

April 13, 2020

MARIN

Contents

Chapter 1

Introduction

Shipping natural gas overseas is an inexpensive and reliable way to move large volumes of fuel. The advantages over other shipping methods, like pipelines or trucks, is that natural gas can be transported globally; and, despite its longer transit, is the most efficient manner for moving it across the world. In its gas state, natural gas density is about 0.8 kgm^{-3} at atmospheric conditions which would make ships highly inefficient for its transport. Nevertheless, when cooled down to its boiling temperature, approximately -162℃, the volume of the liquid drops to 1/600 of the gas volume at atmospheric pressure. To carry the cryogenic fluid in the tanks, a cargo containment system (CCS) is fit inside the cargo tanks to thermally insulate the fluid from the ship's structure. The CCS reduces the amount of boiled liquefied natural gas, known as boil-off, and prevents the structure from cooling down to unsafe temperatures—the steel would become brittle in direct contact with the cryogenic fluid.

Vessels transporting liquefied natural gas are known as LNG carriers. Despite being built, maintained and operated with higher standards than general ships, dry dock inspections have shown deformed and/or punctured CCS caused by the sloshing of the LNG in partially filled tanks. When a cargo tank is partially filled, the motion of the ship is transferred to the fluid and surface gravity waves are formed and propagate towards the walls of the tank. These incidents, along with the new market demands where maximizing the operational flexibility is sought—operating with partially filled tanks for instance—led to multiple research programs for updating the methodology used in the design of the CCS—the sloshing assessment methodology. Many authors have shown that the methodology is globally conservative in the long term whereas reality is not perfectly represented in the short term statistics, as pressure values at full scale were found to be sometimes larger than at model scale (Lund-Johansen et al., 2011; Bogaert, 2018). Having a methodology that gives accurate estimates of the expected loads on the structure is of high importance due to the existing trade-off between structural stiffness and insulation capacity.

The state-of-the-art sloshing assessment methodology is based on a structural reliability approach (Gervaise et al., 2009). The probability distribution of the sloshing impact loads is determined by model tests and compared to the structural capacity of the CCS to obtain the probability of failure. However, many repetitions of the test conditions are required to obtain converged probability distributions of the load maxima due to the transient nature of sloshing impacts. In an investigation to better understanding the physics of wave impacts, Bogaert (2018) divided the flow into two parts: the global and the local flow. The global flow being considered as the solution of the incompressible Euler equations for the liquid and gas in the tank; and the local flow as a perturbation of the global flow. The research was focused on the the local flow and its link to the impact pressures, and the structural response of the CCS. Nevertheless, the author found to be a challenge to generate repeatable global flows and, therefore, to determine the contribution of the local flow to the impact pressure variability. The challenges the author encountered were: (1) the inability of the wavemaker to mechanically follow the steering signal accurately, (2) the lack of accuracy in measuring the water depth due to low frequency waves in the flume and wind in the outdoor facility; and (3) the effect of wind on the propagation of waves through the flume.

In this scenario is where the SLING research program comes into play. One of the SLING project objectives is the extension of the physics in the numerical models to represent the phase change between the gas and the liquid, the development of free surface instabilities and the structural response. In order to achieve the objectives, a new facility is being established at MARIN: the Multiphase Wave Lab (MWL), where a 12.5m flume is installed inside a 15m long, 2.5m diameter autoclave, and where tests can be performed over a wide range of conditions—pressure, temperature, gas composition and water depth can be independently, accurately and automatically controlled. In addition, strict requirements in wave generation were demanded to reduce input variability to negligible levels.

1.1 Problem definition and objectives

Despite the numerous experiments, numerical simulations and theoretical analysis that have been conducted by the scientific community to investigate the local flow of liquid impacts, the physics of the local flow are still not fully understood (Bogaert, 2018).

The limitations of the numerical simulations concern the accurate implementation of the physics, whereas theoretical models lack physics and only describe a part of the impact pressures. Therefore, numerical simulations and theoretical models need to be combined with experiments to disentangle the physics of the local flow.

One of the main reasons why the analysis of the local flow does not result in definitive conclusions in the literature is that the local flow results in impact pressures that vary significantly. In consequence, many repetitions of the same global flow are needed in order to obtain converged statistics of the impact pressures. However, experimental studies of the local flow often result in a too small sample of the maximum impact pressures due to the difficulties researchers have to obtain repeatable global flows.

In the previous section, the challenges Bogaert (2018) encountered in the generation of repeatable global flows were enumerated. The main objective of this thesis is ”to obtain repeatable global flows in the MWL wave flume”. To achieve the objective, the following research questions are defined:

Q1. What are the main sources of variability affecting the global flow?

Q2. What is the influence of the sources of variability in the global flow?

Q3. When is the global flow considered to be repeatable?

Q4. How can repeatability be achieved experimentally in the MWL?

1.2 Research approach

To address the research questions formulated above, theoretical and experimental techniques have been required. A wave generation and propagation model has been developed based on linear wave/wavemaking theory. The model allowed for the evaluation of the sources of variability at different positions along the flume and also the generation of the control signals used experimentally. From the analysis of the variability introduced at the focal point by the sources of variability, a repeatability criterion has been derived. The criterion specifies the conditions under which repeatable global flows are expected experimentally. To validate the theoretical work, experimental tests were conducted for which image processing techniques have been required to quantify the global flow repeatability from video data. An overview of the research approach followed is shown in Figure 1.1.

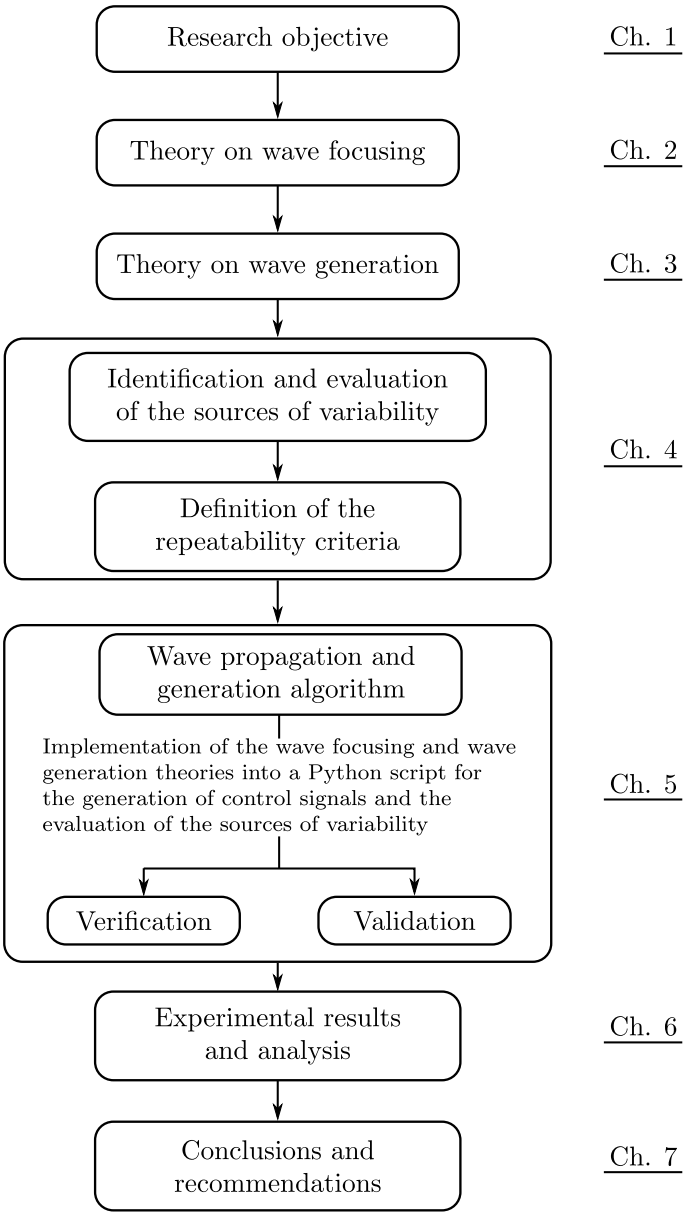

Figure 1.1: Research approach to address the research questions.

Chapter 2

Theory on wave focusing

The methodology to create breaking waves in a flume by means of linear or nonlinear superposition and phasing of wave components is known as wave focusing. The propagating velocity of a wave in a medium is function of its wavelength and period, characteristics that are linked through the dispersion relation. The dispersion relation is an expression obtained from substituting the wave potential into the free surface boundary conditions, which shows that longer waves travel faster than shorter waves. Wave focusing takes advantage of this effect to create a series of wave components with different wavelengths that *focus* at a point. Shorter waves are generated first followed by longer waves, which results in the longer waves catching up the shorter ones. Wave breaking occurs when the height of the focused wave is over the maximum stable height. Several criteria exist for the definition of this height, both empirical and theoretical, with common parameters in its definition: the wave period and the water depth.

This chapter covers the underlying theory on wave focusing. From the dispersion relation to the derivation of a wave train that would lead to wave focusing at a certain distance, the focal point; by briefly describing the different existing techniques on wave focusing.

2.1 Frame of reference

Considering a rectangular two-dimensional basin of length, L, and water depth, h, where the wavemaker is placed at the left side and the impact wall on the right, i.e., waves propagating towards the right; the origin will be located at the focal point at the mean free surface level with the positive x-direction pointing to the right and the positive z-direction up, see Figure 2.1.

Locating the origin at this position simplifies the definition of the wave shape, as the term kx in the linear wave elevation equation ($\eta(x,t) = a\exp\left[i\left(kx - \omega t + \phi\right)\right]$) vanishes at this position. Additionally, if the time at which focusing occurs, the focal time, is set to $t = 0$, meaning that wave generation and propagation happens at negative times; the term ωt also vanishes. This implies that, for a set of waves in phase at the focal time and position, setting $\phi = 0$, the theoretical free

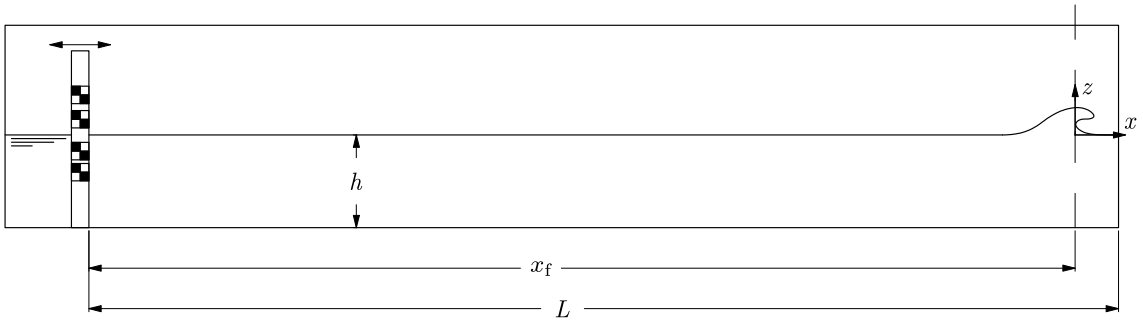

Figure 2.1: Frame of reference used for wave focusing.

surface elevation at that point is the sum of the amplitude of the individual components.

2.2 Governing equations

The flow field of free surface waves is described by a potential, Φ. Assuming the flow to be inviscid, irrotational and incompressible, this potential satisfies the Laplace equation:

$$\frac{\delta^2\Phi}{\delta x^2} + \frac{\delta^2\Phi}{\delta z^2} = 0 \tag{2.1}$$

The boundary conditions to this problem are given by:

- The impermeability condition at the bottom ($z = -h$):

$$\frac{\delta\Phi}{\delta z} = 0\bigg|_{z=-h} \tag{2.2}$$

- The kinematic condition at the free surface:

$$\frac{\delta\eta}{\delta t} + \frac{\delta\Phi\delta\eta}{\delta x\delta x} = \frac{\delta\Phi}{\delta z}\bigg|_{z=\eta} \tag{2.3}$$

- The dynamic condition at the free surface:

$$\frac{\delta\Phi}{\delta t} + \frac{1}{2}\left[\left(\frac{\delta\Phi}{\delta x}\right)^2 + \left(\frac{\delta\Phi}{\delta z}\right)^2\right] + g\eta = 0\bigg|_{z=\eta} \tag{2.4}$$

Conditions eq. (2.3) and eq. (2.4) can be linearized around the mean free surface level using the Taylor expansions:

$$\frac{\delta\Phi}{\delta x}\bigg|_{z=\eta} = \frac{\delta\Phi}{\delta x} + \eta\frac{\delta}{\delta z}\frac{\delta\Phi}{\delta x} + \mathcal{O}\left(\eta^2\right)\bigg|_{z=0} \tag{2.5}$$

$$\frac{\delta\Phi}{\delta z}\bigg|_{z=\eta} = \frac{\delta\Phi}{\delta z} + \eta\frac{\delta^2\Phi}{\delta z^2} + \mathcal{O}\left(\eta^2\right)\bigg|_{z=0} \tag{2.6}$$

Substituting a potential of the form:

$$\Phi = P(z)e^{i(kx-\omega t)} \tag{2.7}$$

into the Laplace equation, eq. (2.1), gives the form of the generic solutions:

$$P(z) = Ae^{kz+a} + Be^{-kz-b} \tag{2.8}$$

which substituted into the seabed condition, eq. (2.2), and solving for the constants gives the generic solution of the potential, valid for the linear and nonlinear problem:

$$\Phi = C\cosh\left(k(z+h)\right)e^{i(kx-\omega t)} \tag{2.9}$$

where C is a complex constant to be determined, k is the wavenumber of the free surface wave, ω its frequency and h the water depth of the flume.

2.3 The dispersion relation

Wave focusing is only possible in the presence of wave dispersion. In its absence, waves would propagate at the same speed and focusing would never occur. The dispersion relation is therefore the basis of wave focusing. There are two types of dispersion relations based on the wave theory from which it is derived:

1. The linear dispersion relation derived from the Airy wave theory; and
2. a nonlinear dispersion relation that accounts for nonlinear phenomena such as amplitude dispersion, i.e., higher waves propagating faster than lower waves; or the fact that the wave profile is not symmetric, the wave crests are sharper than the troughs.

A brief description of these theories is given below followed by a short discussion on the wave theory used in this thesis.

2.3.1 Linear theory

In the linear theory, quadratic and higher order terms are neglected. The linearized free surface conditions:

$$\frac{\delta\eta}{\delta t} = \left.\frac{\delta\Phi}{\delta z}\right|_{z=0} \tag{2.10}$$

and

$$\left.\frac{\delta\Phi}{\delta t} + g\eta = 0\right|_{z=0} \tag{2.11}$$

are obtained from substituting eq. (2.5) and eq. (2.6) into eq. (2.3).

By differentiating eq. (2.11) to time and substituting eq. (2.10):

$$\left.\frac{\delta^2\Phi}{\delta t^2} + g\frac{\delta\Phi}{\delta z} = 0\right|_{z=0} \tag{2.12}$$

If the general solution, eq. (2.9), is substituted into this expression and evaluated at $z = 0$, the linear dispersion relation is obtained:

$$\omega^2 = gk\tanh(kh) \tag{2.13}$$

The Airy wave solution only uses the real value (ω, k) pairs, obtaining the well-known free surface elevation expression from the substitution of the general solution, eq. (2.9), in the linear boundary condition, eq. (2.10):

$$\eta = ae^{i(kx-\omega t+\phi)} \tag{2.14}$$

Nevertheless, the imaginary solutions are also required when deriving the wavemaker's transfer function, section 3.1. Obtaining:

$$\eta = -\frac{i\omega}{g}C\cosh(kh)e^{i(\omega t-kx)} \tag{2.15}$$

The linear dispersion relation, eq. (2.13), shows that the relation (ω, k) does not depend on the wave amplitude. Additionally, it can be shown that in shallow and deep waters, the expression approximates to:

- Shallow water, $kh \ll 1$:

$$\omega^2 = ghk^2 \tag{2.16}$$

- Deep water, $kh \gg 1$:

$$\omega^2 = gk \tag{2.17}$$

Phase and group velocity

The phase velocity is the speed at which a wave component propagates. The expression is derived following a specific position of the wave in time. The wave phase at that location in the wave must be constant as the wave propagates. Taking the wave elevation determined by eq. (2.14) and choosing a position whose phase is zero for simplicity, the angle of the complex expression must be equal at two different points in time and space, leading to the phase velocity:

$$\begin{aligned} &kx_0 - \omega t_0 = kx_1 - \omega t_1 \\ &c_p = \frac{\Delta x}{\Delta t} = \frac{\omega}{k} \end{aligned} \tag{2.18}$$

The expression for the group velocity comes from the effects of superposing two waves with

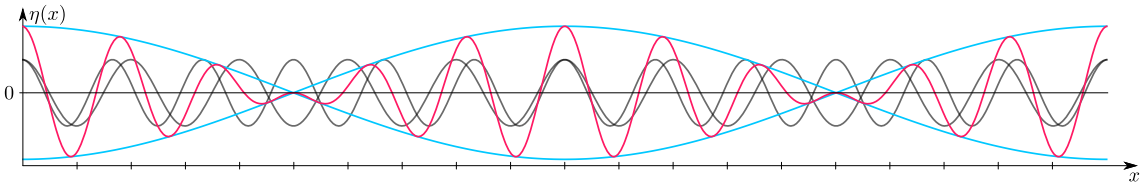

Figure 2.2: Two harmonic waves with slightly different frequencies (——) adding up to a series of wave groups (——). The envelope (——) propagates with the group celerity. In each group, waves are being formed at the tail and vanishing at the front due to the higher phase velocity.

the same amplitude and slightly different frequency. As a result of the interaction between them, these waves reinforce each other when they are in phase, but cancel out when they are 180° out of phase, see Figure 2.2. This effect repeats over creating a series of wave groups which travels at the same speed as the wave energy (Holthuijsen, 2010). If the difference between the frequencies is infinitely small, the group velocity is given by:

$$c_g = \frac{\partial \omega}{\partial k} \tag{2.19}$$

The substitution of the phase speed, eq. (2.18), and group speed, eq. (2.19), into the linear dispersion relation, eq. (2.13), results in:

$$c_p = \sqrt{\frac{g}{k}\tanh(kh)} \tag{2.20}$$

$$c_g = \frac{1}{2}c_p\left(1 + kh\frac{1-\tanh^2(kh)}{\tanh(kh)}\right) \tag{2.21}$$

In shallow and deep waters, these expressions simplify to:

- Shallow water:

$$c_p = c_g = \sqrt{gh} \tag{2.22}$$

- Deep water:

$$c_p = \sqrt{\frac{g}{k}} \tag{2.23}$$

$$c_g = \frac{1}{2}c_p \tag{2.24}$$

Which clearly shows the relation between wavelength and water depth on the propagation speed. In shallow waters there are not apparent dispersion effects. Waves propagate at the 'same' speed independently of the wavelength[1]. As a consequence, long waves that lie in the shallow water regime have to be generated almost simultaneously in wave focusing due to the small difference in propagating speed. On the other hand, on deep water conditions, wave components travel exactly at half their phase velocity independently of the water depth. As it will be seen later on, the wave components used in the MWL lie in the three regimes: shallow water, intermediate water and deep water; which makes wave focusing highly dependent on the control and measurement of the flume's water depth.

2.3.2 Nonlinear theory

There are two main nonlinear wave theories assuming an irrotational flow: the Stokes theory, suitable for waves which are not very long relative to the water depth; an the Cnoidal theory, suitable for long waves relative to the water depth. The steady waves derived from these theories are asymmetric, with the wave crest being sharper than the wave trough, Figure 2.3.

[1] Shallow and deep water are the asymptotic limits imposed in the dispersion relation and, therefore, they are never reached. There will always be wave dispersion even when its value is infinitely small.

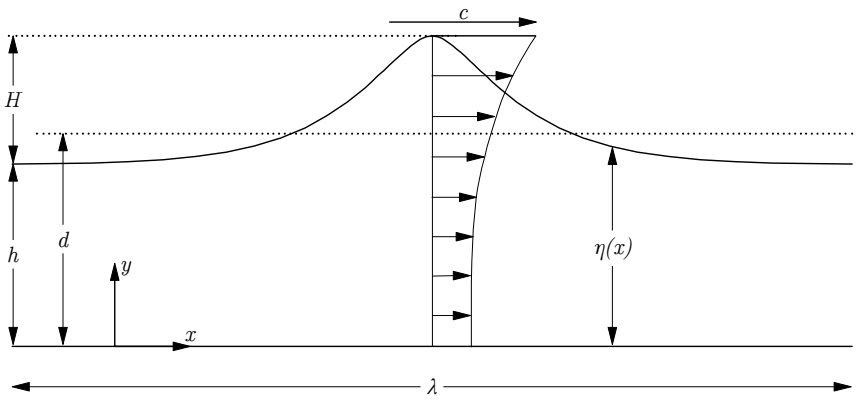

Figure 2.3: A nonlinear steady wave derived either from Stokes' or Cnoidal theory (Fenton, 1990). Consequence of the asymmetry of nonlinear waves, the still water depth, d in the figure, does not lie at half the wave height, H.

These theories can be approximated to any order, which depends on the application and the steepness of the wave under study. Le Méhauté (2013) studied the validity of the different analytical theories comparing them to experimental data, showing the range of validity and the required order, see Figure 2.4.

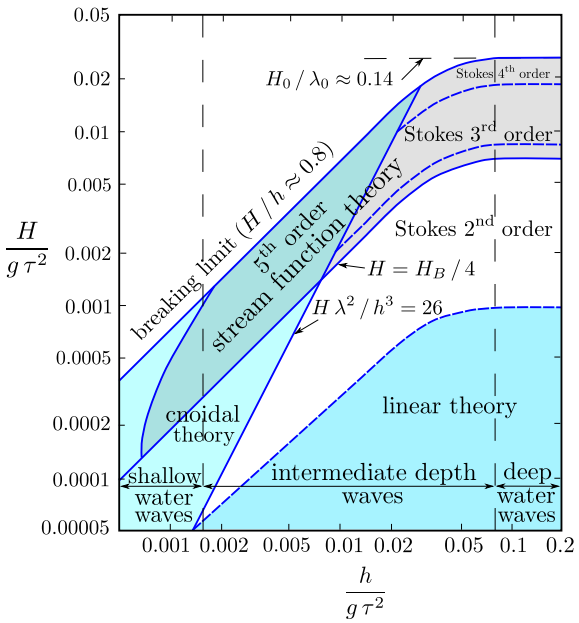

Figure 2.4: Validity theories for steady waves according to Le Méhauté (2013). The dashed blue lines demarcate the *required* order in the Stokes' wave theory.

Stokes assumed that all variation in the longitudinal direction of the wave can be represented by Fourier series and the coefficient of these series can be written as perturbation expansions in terms of the wave amplitude—Schwartz (1974) utilized the wave height instead because higher order expansions showed wave height convergence before the maximum wave height was reached. According to Stokes' second-order theory, the wave elevation on arbitrary depth is given by:

$$\eta\left(x,t\right)=a\left\{\cos\theta+\left(ka\right)\frac{3-\sigma^{2}}{4\sigma^{3}}\cos 2\theta\right\}+\mathcal{O}\left(\left(ka\right)^{3}\right) \tag{2.25}$$

And the substitution of the second-order Stokes' solution into the third-order equations of the perturbation series for the periodic wave problem (not shown here for the sake of simplicity) gives

the third-order dispersion relation[2]:

$$\omega^2 = (gk\tanh(kh))\left\{1 + \frac{9 - 10\sigma^2 + 9\sigma^4}{8\sigma^4}(ka)^2\right\} + \mathcal{O}\left((ka)^4\right) \tag{2.26}$$

with:

$$\sigma = \tanh(kh)$$

Due to the complexity of the math involved in its derivation, Cnoidal theory is not covered in this report. Nevertheless, Cnoidal theory must be used in those cases where Stokes' theory does not apply. The parameter defining the boundary between Stokes' and Cnoidal theory is the Ursell number:

$$\boldsymbol{U} = \frac{H/d}{(d/\lambda)^2} = \frac{\text{"Nonlinearity" (measure of height)}}{\text{"Shallowness" (measure of depth/length)}} \tag{2.27}$$

Hedges and Ursell (1995) showed that the reasonable boundary between the Stokes' and Cnoidal theory is:

$$\boldsymbol{U} = \frac{H\lambda^2}{d^3} = 40 \tag{2.28}$$

Those waves with larger Ursell number are generally long-high waves, and Cnoidal theory should be used. Smaller Ursell numbers correspond to deeper waters, relative to the wave length, and Stokes' theory is best. However, there is a discontinuity in the wave celerity predicted by these theories. Kirby and Dalrymple (1986) propose an empirical extension to the existing formulations which smoothly connects the Stokes' analytical results to the empirical formulation for shallow water of Hedges (1976). The second-order expression becomes:

$$\omega^2 = gk\left(1 + \sqrt{\tanh^5(kh)}\,(ka)^2\,D\right)\tanh\left(\frac{kh + (ka)}{1 + \sqrt{\tanh^5(kh)}\,(ka)^2\,D}\right) \tag{2.29}$$

Where the coefficient D is an expression in terms of hyperbolic functions.

Many other empirical formulations exist connecting both shallow and deep water theories. Further and more detailed information about the different dispersion relations can be found in van den Boomgaard (2003).

2.3.3 Discussion

It is clear from literature that predictions of wave celerity from linear theory lead to errors in the focal time and focal point due to waves propagating faster than predicted (Hofland et al., 2011; John R. Chaplin, 1996; Fernández et al., 2014). Linear theory is therefore inconvenient where waves of different heights or frequency are required at exactly the same point. Nevertheless, for repeatability studies, where a wave is created many times, the use of linear theory seems appropriate: it is simple and computationally cheap, which makes it ideal for sensitivity studies and wave modelling, section 2.5.

2.4 Wave focusing techniques

Knowing how dispersion affects wave propagation, it can be used for the generation of extreme events that would not be possible to create if waves propagated at the same speed. Examples of such events are the generation of freak waves (or rogue waves) in irregular sea states (Liu et al., 2011), or the generation of breaking waves (Kimmoun et al., 2010).

John R. Chaplin (1996) described the three different techniques that can be identified:

[2] The Stokes' second-order dispersion relation matches Airy's dispersion relation.

1. The phase speed method: wave trains of different frequencies, traveling at different speeds, add up producing reinforcement or cancellation of water surface displacements. The phases of each wave component can be adjusted such that a large wave builds up at a specific point in time, see Figure 2.5a.

   In this method, the wavemaker control signal is derived from the wave elevation time trace at the wavemaker's position, which is computed summing up each sinusoidal component whose phase is chosen to achieve reinforcement at the focal point. If focusing is set at $x = 0$, $t = 0$; and the wave maker is located at $x = -x_f$, as defined in section 2.1, the following expression gives the wave elevation time trace at the wavemaker's position derived from linear theory.

   $$\eta_{\mathrm{wm}} = \sum_{i=1}^{n} a_i e^{i(-k_i x_f - \omega_i t)} \tag{2.30}$$

2. The reverse dispersion method: from the release of an initial disturbance of the free surface, waves travel outwards in both directions. The wave elevation time trace at a distance from this releasing point can be used to derive the wavemaker's control signal on the basis that, if waves traveled in the opposite direction, they would lead to the same initial disturbance, see Figure 2.5b. However, from the initial disturbance waves travel in both directions and, therefore, having only one wavemaker would lead to a focused wave with half the energy of the initial disturbance.

   An analytical solution for this method was first presented by Cauchy and Poisson for the simple case of waves moving outward from an initial surface elevation shaped as a delta pulse. Many authors extended the work to include multidimensional propagation, intermediate water depth or a geometric distribution of the initial disturbance, among others (Lamb, 1923; Eckart, 1948; Unoki and Nakano, 1953; Wang et al., 1987).

3. The group celerity method: the front of a wave train propagates into still water at a speed equal to the group celerity. Assuming that the speed of energy propagation is related to the instantaneous frequency of the waves generated by the wavemaker, a continuous modulation in the frequency of the steering signal can lead to a concentration of energy at a particular point in the flume, see Figure 2.5c.

   Given the focal distance, the time domain $\left[t_{\mathrm{begin}}, t_{\mathrm{end}}\right]$ can be defined. The starting time, t_{begin}, is obtained from the wave celerity of the maximum frequency component in the wave train (the slowest of the components) via a dispersion relation. The end time, t_{end}, is given by either the celerity of the minimum frequency component in the set of waves or by the physical limit—no more waves can be generated that reach the focal point on time when the physically maximum possible group velocity is reached, eq. (2.22), (Hofland et al., 2011).

From the three techniques, the phase speed method has been used for the derivation of the wave elevation time trace at the wavemaker's position. To support the decision, Kimmoun et al. (2010) showed great results in wave focusing and wave crest stability using this technique in a similar flume. Additionally, it allows wave shape modelling at the focal point, which requires the use of complex math in the reverse dispersion method (Wang et al., 1987); and there is no need for phase adjustment like in the group celerity method (Hofland et al., 2011).

2.5 Wave modelling

Wave modelling will be referred to as the process of tuning the focused wave characteristics, i.e., period, height, focal point, etc; until the wave/impact of interest is obtained. Before the control signal for the generation of these waves can be derived, the wave elevation time trace at the wavemaker's position must be obtained. The phases of each wave component at this position can be computed using the phase speed method via a dispersion relation and the corresponding wave theory, and the free surface elevation obtained from the summation of each wave component elevation.

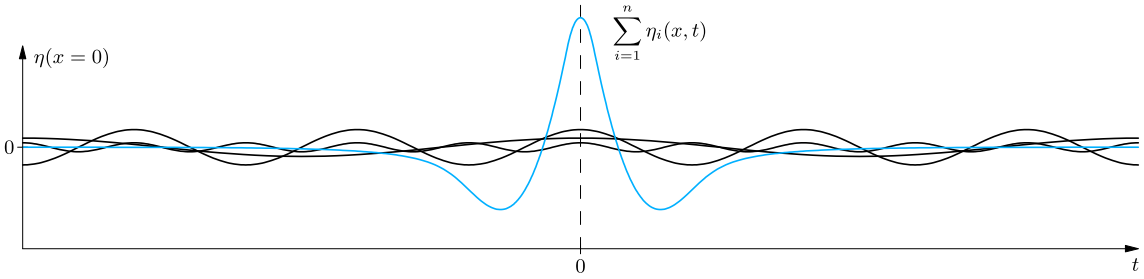

(a) Phase speed method

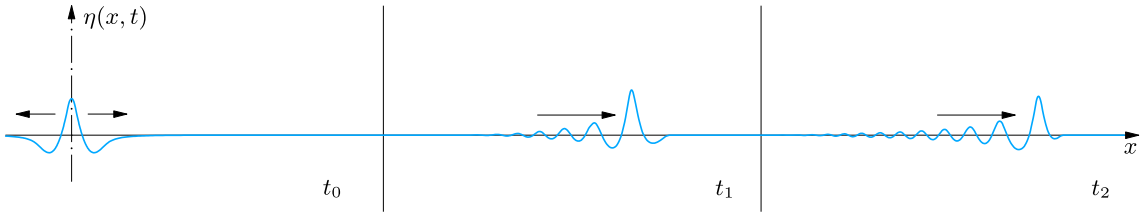

(b) Reverse dispersion method

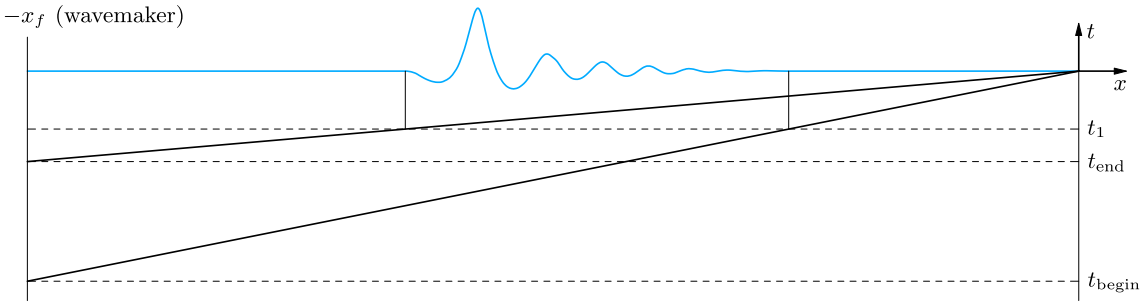

(c) Group celerity method

Figure 2.5: Illustrations showing the different methods for the derivation of the control signal

Due to its simplicity, linear theory is appropriate for wave modelling and sensitivity studies because it allows to perform many computations in affordable amounts of time. Time is a key factor in wave modelling as one would like to carry out as many test as possible. Typically, the waiting times between two tests in a flume of this characteristics range from 20 to 60 minutes (Kimmoun et al., 2010), so computing a control signal should be done, preferably, inside this time window. Any higher order theory would result unpractical due to the large number of components required in the derivation of the control signal, as will be discussed in section 3.2.1.

2.5.1 Frequency and amplitude distribution

A steady wave is characterized by a wavenumber, its frequency and the amplitude of the wave; with the wavenumber and frequency linked through the dispersion relation. When a breaking wave is sought, the energy of the wave train should lead to a focused wave height over the minimum wave height for breaking. This minimum wave height is given by the Miche criterion, which describes wave breaking when the limiting wave steepness is exceeded (Miche, 1944):

$$\frac{H_\mathrm{b}}{L_\mathrm{b}} = 0.14 \tanh\left(\frac{2\pi h_\mathrm{b}}{L_\mathrm{b}}\right) \tag{2.31}$$

Nevertheless, this is expression is valid for *one* steady wave, though a focused wave is formed by the interaction of many wave components. Therefore, this expression should be taken as a reference, realizing that wave breaking will occur at smaller wave heights (Southgate, 1988). With this in mind, there are two ways to achieve wave breaking:

1. Giving to each wave frequency a constant fraction of its minimum wave breaking height: this

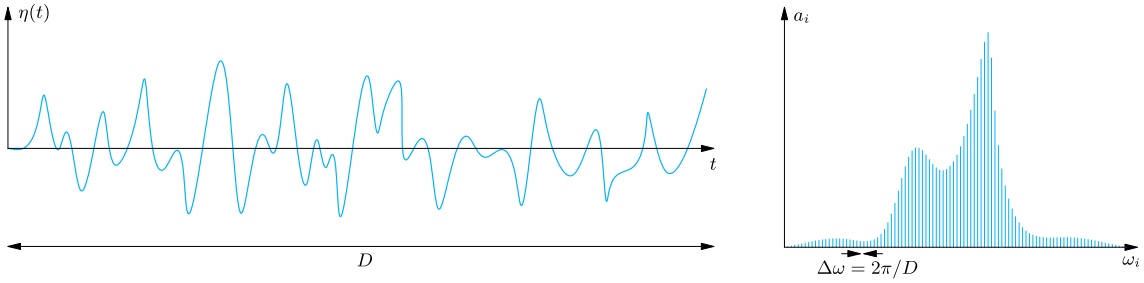

Figure 2.6: Discrete amplitude spectrum illustration from a wave elevation record.

approach is used by Hofland et al. (2011). However, due to wave-wave interactions early breaking of the higher frequency components was observed before the focal time; or

2. defining a wave amplitude spectrum whose total energy ensures wave breaking: this is the approach used by Kimmoun et al. (2010). The amplitude spectrum can be tweaked not only to avoid early breaking but also to modify the breaking wave characteristics (crest stability, crest thickness, gas pocket size, etc)

While both methods give a breaking wave, defining an amplitude spectrum offers extra flexibility in wave modelling.

The Ricker spectrum

The concept of wave spectrum is simple. Considering the surface elevation $\eta(t)$ at one location as function of time, with a certain duration D, the record can be reproduced as the sum of a large number of harmonic wave components (a Fourier series):

$$\eta(t) = \sum_{i=1}^{n} a_i \cos\left(\omega_i t + \phi_i\right) \tag{2.32}$$

Ignoring the phase spectrum, only the amplitudes, a_i, of each wave frequency, ω_i, remain to characterize the wave record. The pairs $(a_i,\ \omega_i)$ define the amplitude spectrum of a wave record, Figure 2.6. Therefore, if all wave components are in phase at the focal point, $\phi_i = 0$, the only requirement to determine the wave elevation at the focal point, or wavelet, is the amplitude spectrum. It can be derived by either: (1) defining the wavelet and computing its spectrum via a Fourier transform or (2) using existing spectrum formulations. The first method is subjected to the requirements and limitations of the Fourier transform. It requires an extremely long time record of the wavelet to increase the frequency resolution, and the amplitude of the zero frequency is forced to be zero. On the other hand, while the second method loses the control on the wavelet shape as it will be determined by the spectrum formulation, the frequency content in these analytically/empirically derived expressions is not predetermined and a non zero amplitude to the zero frequency can be given (the importance of the amplitude of the zero frequency is explained later). Thus, a spectrum formulation has been used to determine the amplitude distribution.

The most well-known and used spectrum formulations in coastal and maritime engineering are the Pierson-Moskowitz and the JONSWAP spectra (Holthuijsen, 2010). These spectra are empirically derived from measurements of ocean waves produced by wind and, therefore, are representative of real sea states. Nevertheless, the resulting wavelet from these spectra resembles a Morlet wavelet (a wave group). The issue with these wavelets is that, in an experimental flume, the wavelet front reflects on the impact wall before focusing occurs, leading to focusing issues and the development of free surface instabilities due to wave-wave interactions. In addition, the height of the smaller-shorter waves at the front could be above the minimum height for breaking, resulting in early breaking as seen in Hofland et al. (2011); Bogaert (2018). This problem was solved by Kimmoun et al. (2010) using the spectrum derived from the mexican hat wavelet, the Ricker wavelet. This wavelet is the negative second derivative of a Gaussian function. As a consequence,

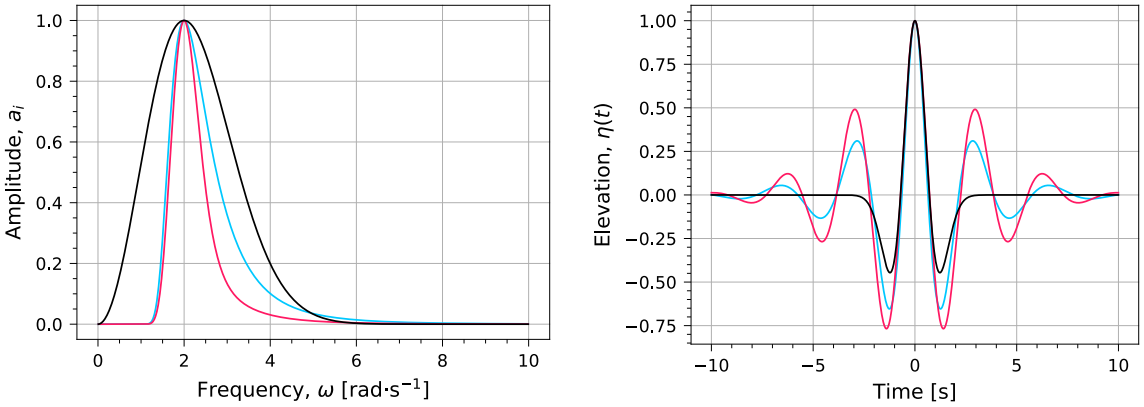

Figure 2.7: Representation of the normalized amplitude spectrum (left) and their respective wavelet (right) for the Ricker spectrum (——), the Pierson-Moskowitz spectrum (——) and the JONSWAP spectrum (——).

it results in a single crest preceded by a trough. Figure 2.7 compares the three amplitude spectrum shapes and their wavelet.

The Ricker wavelet is defined in the time domain as:

$$\eta_R(t) = \left(1 - 1\frac{1}{2}\omega_{\mathrm{p}}^2 t^2\right) \exp\left(-\frac{1}{4}\omega_{\mathrm{p}}^4 t^2\right) \tag{2.33}$$

where ω_{p} is the peak frequency of the event (in radians per second).

And its Fourier transform gives the Ricker wavelet amplitude spectrum (Wang, 2015):

$$a_{\mathrm{R}}(\omega) = \frac{2\omega^2}{\omega_{\mathrm{p}}^3\sqrt{\pi}} \exp\left(-\frac{\omega^2}{\omega_{\mathrm{p}}^2}\right) \tag{2.34}$$

However, when this amplitude spectrum is used for the derivation of a control signal and tested experimentally, it results in a surging wave (a non-breaking rounded wave) or in a spilling wave (a long and foamy breaking wave). The reason is the lack of energy in the lower part of the spectrum, essential for wave breaking (Kimmoun et al., 2010). Researchers usually derive a control signal using any method and introduce energy to the wave train by cutting out the last part of the control signal and introducing the control signal of a solitary wave, see Figure 2.8 from Hofland et al. (2011).

In this thesis, to introduce energy in the lower frequencies, avoiding hand-tweaking of the control signal and increasing wave modelling flexibility, two parameters were included to the formulation of the Ricker spectrum, eq. (2.34):

1. A parameter to increase the amplitude of the frequencies below the peak frequency by a constant fraction of the amplitude difference of each frequency w.r.t. the peak frequency amplitude; and
2. a parameter to compute the amplitude of the frequencies above the peak frequency from a shifted frequency, which increases or decreases energy in those frequencies.

Including these parameters result in a piecewise expression of the spectrum:

$$a_i(\omega) = \begin{cases} (1-\beta_l)\, a_{\mathrm{R}}(\omega_i) + \beta_l a_{\mathrm{R}}(\omega_{\mathrm{p}}) & \text{for: } \omega_i \leq \omega_{\mathrm{p}} \\ a_{\mathrm{R}}(\omega_i + \beta_h(\omega_{\mathrm{p}} - \omega_i)) & \text{for: } \omega_i > \omega_{\mathrm{p}} \end{cases} \tag{2.35}$$

where β_{l} and β_{h} are the low and high frequency parameters, respectively.

The control that these parameters offer in the spectrum and wavelet shape is shown in Figure 2.9. Notice how the zero frequency component has a non-zero amplitude now in the spectrum, equal to half the energy of the peak frequency, $\beta_{\mathrm{l}} = 0.5$; and the increase of energy in the higher

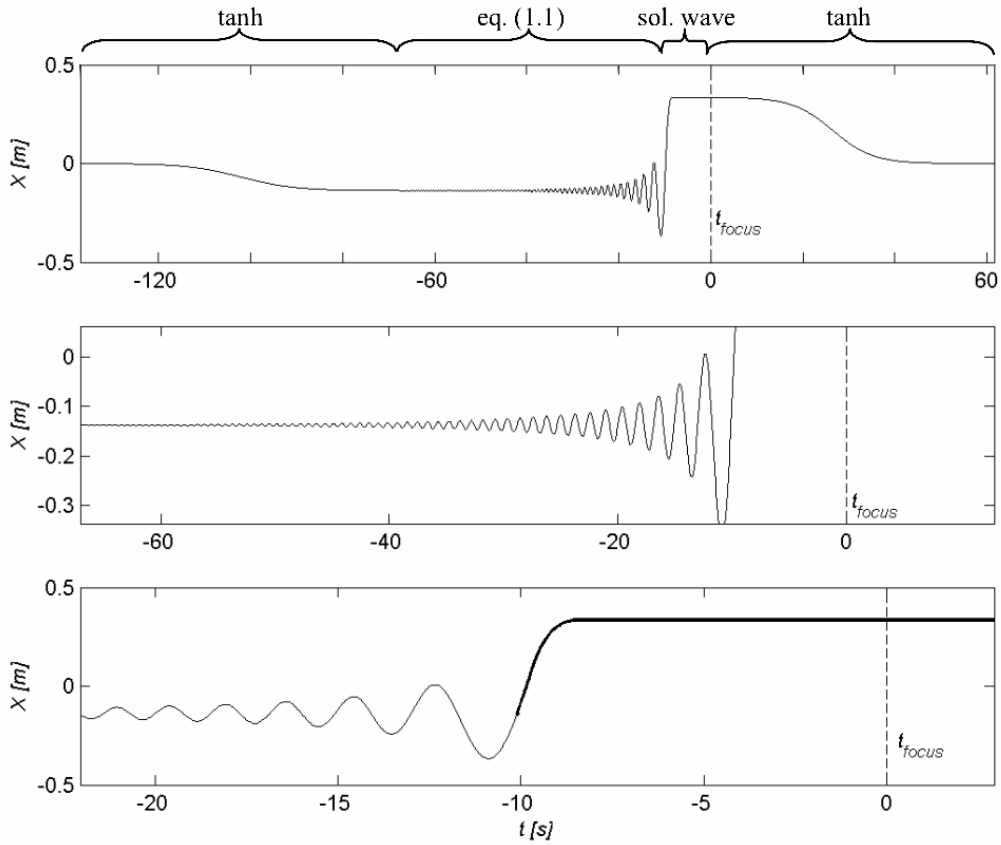

Figure 2.8: Example of a control signal and how Hofland et al. (2011) introduced energy to the wave train connecting the solitary wave solution (thick line).

frequencies, $\beta_{\mathrm{h}} = 0.45$. The original formulation is obtained when both parameters are equal to zero. It must be said that having a non-zero value at the zero frequency results in a positive shift of the wavelet equal to the amplitude of the frequency. This is not apparent in the figure because a large number of components (10.000) are being used, precisely to reduce the relative influence w.r.t. the wave height—as the number of wave components increases, the amplitude of each component reduces. In the limit $\Delta\omega \to 0$ the amplitude of each component is zero and, therefore, the relative importance of each component to the free surface elevation is zero.

2.5.2 Wave elevation at the wavemaker

The wave elevation at the wavemaker is obtained combining the linear dispersion relation, the wave elevation expression derived from linear theory, and the amplitude spectrum for the wave characteristics of interest. The procedure is as follows:

1. The peak period, ω_{p}, of the focused wave and its wave height is set. Then,
2. the amplitude spectrum for a number of wave frequencies is computed and scaled such that its area matches the wavelet height matches the previously defined wave height; and
3. the wavenumbers are determined from the linear dispersion relation, eq. (2.13).
4. Amplitude, wavenumber and frequency are used to compute the wave elevation time trace of each wave component at the wavemaker, eq. 2.14); and
5. by adding up the wave elevation time trace of all wave components, eq. (2.30), the wave elevation at the wavemaker is obtained.

In this thesis, the reference wave height defining the spectrum is the wave crest height, H_{c}, or the height from the mean free surface level to the crest of the wavelet. This has been done to

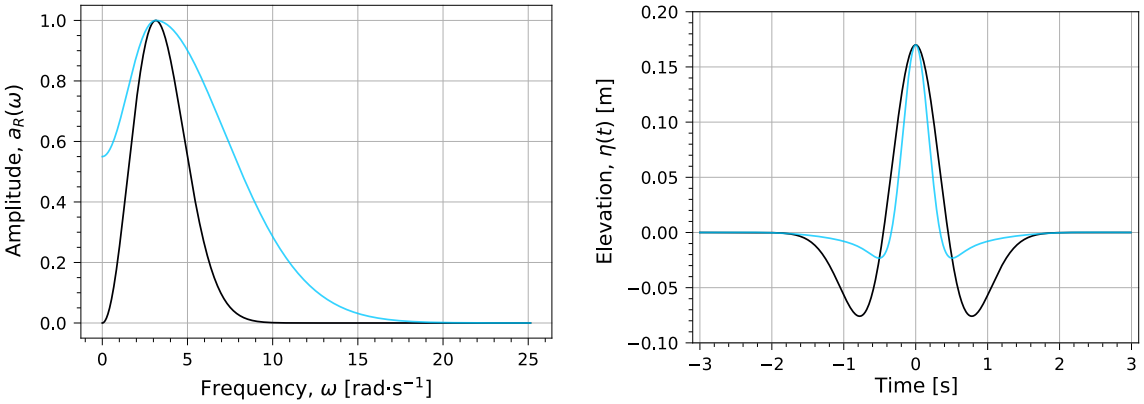

Figure 2.9: Original Ricker spectrum and wavelet formulation (——) compared to the spectrum and wavelet using eq. (2.35) (——).

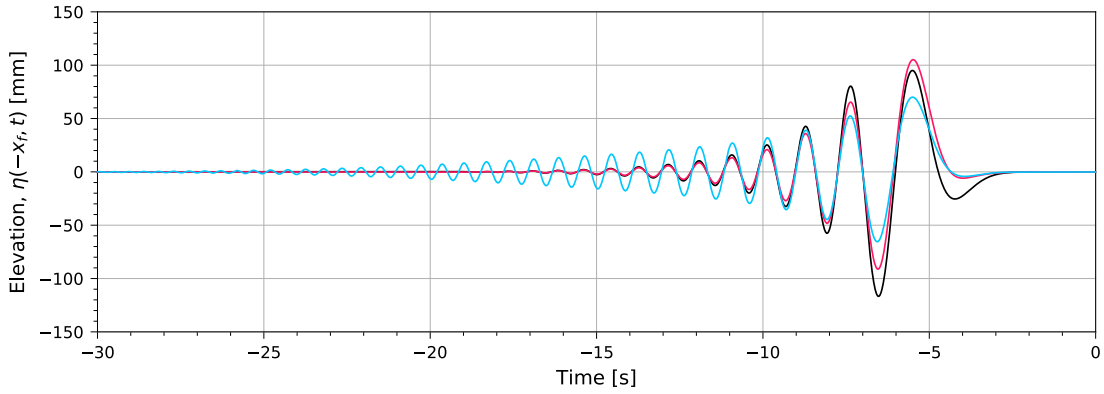

Figure 2.10: Time trace of the wave elevation at the wavemaker position from the original Ricker spectrum (——) and from the modified Ricker spectrum for $\beta_l = 0.5$ and $\beta_h = 0$ (——); and for $\beta_l = \beta_h = 0.5$ (——).

decouple the parameter β_l from the wave height of interest. As will be seen next, the parameter flattens the trough of the wavelet as it increases and therefore reduces the distance from trough to crest. If two waves with the same wave height were compared in this way for two values of β_l, the result would be two waves with the impact point at two different heights. Therefore being difficult to compare and evaluate the influence of the parameter in the wave shape.

The result of the previous operations is shown in Figure 2.10, comparing the obtained wave elevation from the original Ricker spectrum and from the modified one. It is clear the increase in amplitude of the high frequency components, consequence of the parameter β_h. The effect of increasing the energy in the lower frequencies is also evident. Increasing β_l results in a reduction of the trough's amplitudes in the last part of the record. Also note that the maximum wave height in the time trace gets reduced when the energy in the higher frequencies is increased (for the same focused wave crest height). The implication is that, when limited by the maximum stroke of the wavemaker, more energetic waves can be obtained increasing the energy in the higher frequencies of the spectrum—as long as the wavemaker is able to accurately move at those frequencies.

Once the wave train that leads to the desired focused wave is determined, the next step is to compute the paddle motion that generates the wave elevation time trace at the wavemaker position—the wavemaker control signal. Since this is a related but different problem, it will be covered in a separate chapter.

Chapter 3

Theory on wave generation

The wavemaker problem to determine the forced two-dimensional wave motion with outgoing surface waves at infinity, generated by a harmonically oscillating vertical plane immersed in water, was first solved by Havelock (1929). This is a first-order solution and, therefore does not account for second-order effects such as the wave set-down of the water level (Hansen et al., 1980), or spurious superharmonic waves that arise from wave interactions (Sulisz and Hudspeth, 1993). The current chapter covers the derivation of the linear wave making theory and its application to the wave elevation time trace obtained in the previous chapter to compute the wavemaker control signal.

The most extensive and detailed second-order wave making theory was given by Schäffer (1996), who derived a complete mathematical model for position-controlled wavemakers including the sub- and superharmonic effects. Posterior studies are on improving the wave generation techniques providing, for instance, active absorption to avoid spurious reflection, reducing the flume's stilling time; or the derivation of a second-order wavemaker theory using force-feedback control which further reduces the spurious harmonic content (Spinneken and Swan, 2009).

A simple theory that illustrates the generation of waves by a piston type wavemaker was proposed by Galvin Jr (1964) for shallow water. This is a very simple theory which does not consider the boundary problem for two-dimensional waves propagating in an incompressible, irrotational fluid—for which the governing equation for the velocity potential is the Laplace equation. Nevertheless, it helps as an introduction to get insight about wave generation and the parameters typically involved in higher-order theories: the reasoning is that the water displaced by the wavemaker should be equal to the crest volume of the propagating wave. Being the volume per unit width of water in a (linear) wave:

$$V_{\text{crest}} = \int_0^{L/2} \frac{H}{2} \sin(kx)\,\mathrm{d}x = \frac{H}{k} \tag{3.1}$$

and the volume displaced by the wavemaker per unit width:

$$V_{\text{wm}} = Sh \tag{3.2}$$

where S is the stroke of the wavemaker.

The expression for the wavemaker motion is found by equating both volumes, yielding:

$$\frac{H}{S} = kh \tag{3.3}$$

3.1 Linear wave making theory

Having the same frame of reference as the one described in section 2.1, the internal flow is still represented by eqs. (2.1–2.9).

If the wavemaker is piston type (MWL's wavemaker), the wave flap displacement is only time dependent, $\xi(t)$. As water cannot flow trough the flap, the impermeability boundary condition must be satisfied:

$$\frac{\delta \xi}{\delta t} = \left.\frac{\delta \phi}{\delta x}\right|_{x=\xi} \tag{3.4}$$

With the flap describing a unitary harmonic motion:

$$\xi(t) = e^{i\omega t} \tag{3.5}$$

the boundary condition, eq. (3.4), at the wave flap becomes:

$$\omega = -kC\cosh\left(k(z+h)\right) \tag{3.6}$$

Solving for the complex amplitude, C, requires decomposing the expression into a set of orthogonal basis functions ($\cosh(k(z+h))$):

$$\int_{-h}^{0} \cosh(k(z+h)) \cdot \omega \, \mathrm{d}z = \int_{-h}^{0} \cosh(k(z+h)) \cdot [-kC\cosh(k(z-h))] \, \mathrm{d}z \tag{3.7}$$

After some algebra:

$$C = \frac{-4\omega\left(\sinh(kh) + \dfrac{1-\cosh(kh)}{kh}\right)}{k\left(\sinh(2kh)+2kh\right)} \tag{3.8}$$

Substituting into the linear free surface elevation, eq. (2.15), results in the transfer function *from* flap excursion *to* wave elevation:

$$\zeta_{\text{piston}} = \frac{4i\omega^2\cosh(kh)}{gk}\left(\frac{\sinh(kh) + \dfrac{1-\cosh(kh)}{kh}}{\sinh(2kh)+2kh}\right) \tag{3.9}$$

From which ω^2 can be eliminated using the linear dispersion relation, eq. (2.13). Then the transfer function becomes:

$$\zeta_{\text{piston}} = \frac{4i\sinh^2(kh)}{\sinh(2kh)+2kh} \tag{3.10}$$

This transfer function suffices to compute the wavemaker control signal. Higher-order wave making theories would be required when the spectrum to be obtained experimentally is required to match the theoretical one. Nevertheless, the object of study is wave repeatability and, therefore, the wave making and wave theory used is not of high importance as long as wave focusing occurs. The spurious waves that form from the linear wave making theory lead to wave-wave interactions not accounted beforehand which shift the focal point. However, these interactions will be the same in different repetitions if the entire process of wave generation is exactly repeatable.

3.2 Wavemaker control signal

The equation defining the wave elevation time trace at the wavemaker, eq. (2.30), divided by the flap excursion to wave elevation transfer function, eq. (3.10), gives the control signal of the wavemaker.

$$X(t) = \sum_{i=1}^{n} a_i \exp\left[i(-k_i x_{\text{f}} - \omega_i t)\right] \cdot \frac{\sinh(2k_i h) + 2k_i h}{4i\sinh^2(k_i h)} \tag{3.11}$$

The obtained control signal for the original Ricker spectrum, eq. (2.34), and the expression of the spectrum used in this work, eq. (2.35), is shown in Figure 3.1. Three main differences are observed here:

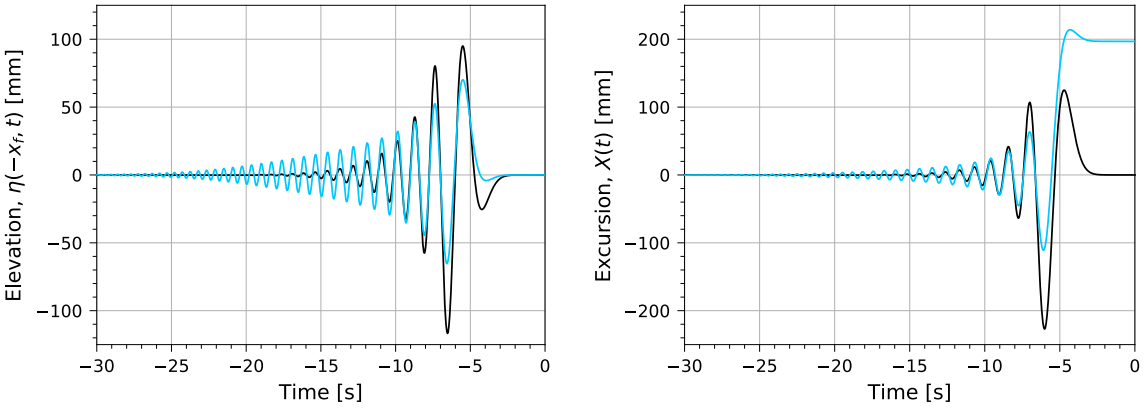

Figure 3.1: Wave elevation at wavemaker position (left) and wavemaker control signal (right) derived for the same focused wave crest height for $\beta_\mathrm{l} = \beta_\mathrm{h} = 0$ (——) and $\beta_\mathrm{l} = \beta_\mathrm{h} = 0.5$ (——).

1. The signal gets longer when increasing β_h, both in the wave elevation and in the control signal; this was already seen in the previous chapter.
2. The amplitude gets smaller in both signals. This is a combined consequence of increasing the energy of the lower and higher frequencies, β_l and β_h.
3. The last part of the wavemaker control signal shifts to a constant non-zero value when $\beta_\mathrm{l} \neq 0$. This is the most important characteristic, and the main reason, for choosing a spectrum that allows a non-zero amplitude of the zero frequency. Those frequencies which travel at the physical velocity limit ($c_\mathrm{p} = c_\mathrm{g} = \sqrt{gh}$) must leave the wavemaker simultaneously such that they reach the focal point on time, therefore shifting the amplitude of the wavemaker motion to a large value as the amplitudes add up. This value seems to be constant due to the extremely long wavelengths of the associated wave frequencies, nevertheless, it would come back to zero if the control signal were computed further in time.

   The importance of it is that the last part of this control signal resembles the one developed by Hofland et al. (2011), Figure 2.8, adding energy to the lowest frequencies without the necessity of hand-crafting the signal.

3.2.1 Number of wave components

The ”drawback” of the used amplitude spectrum formulation is the large number of wave components required to derive the control signal. The non-zero amplitude of the zero frequency leads to a positive mean displacement of the free surface as discussed in section 2.5.1—a zero frequency is infinitely long, extending along the entire flume with amplitude $a_\mathrm{R}(0)$. The wave elevation divided by the transfer function leads to a positive non-zero excursion of the paddle at the time of generation because the infinitely long wave must be already in the flume. Then, shorter wave components interact with the zero-frequency moving the wavemaker mean position backwards. The drift velocity of the wavemaker reduces as the number of wave components increases, being zero in the limit $\Delta\omega \to 0$, when the contribution (amplitude) of each wave component is zero, see Figure 3.2; which results in a constant negative offset of the paddle as shown in the figure for 50000 wave components. Since this offset is only a consequence of having a non-zero amplitude in the zero frequency component—the theory used does not account for constant volume of water in the flume—the signal is centered in practice such that it starts at the zero position of the paddle.

3.2.2 Control system requirements

To fulfill the requirements of the wavemaker control system, the signal must start and end at its zero position. Therefore, a sinusoidal signal was attached at the end of the control signal, slowly returning the wavemaker back to zero. Additionally, it may happen that the wavemaker control signal is not accepted by the control system because its motion is out of limits. This usually happens in the last stroke of the control signal, where its maximum forward motion almost doubles

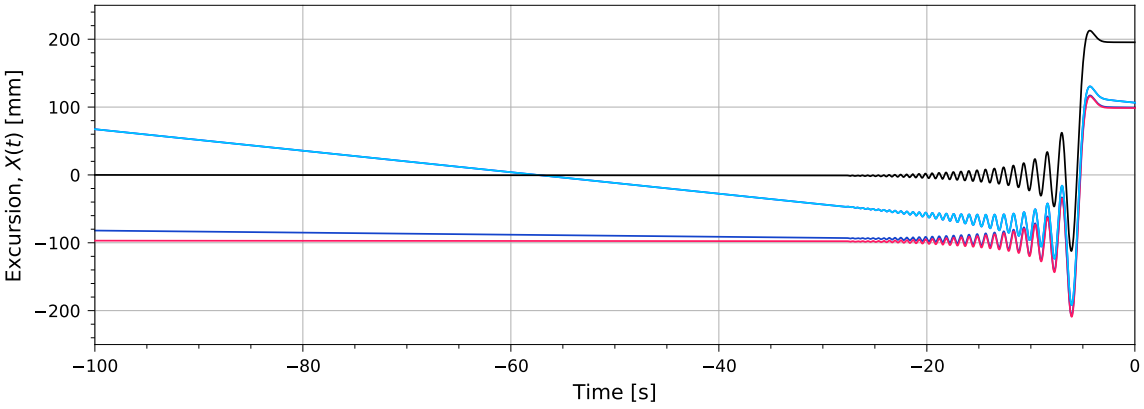

Figure 3.2: Wavemaker control signals obtained with the same focused wave characteristics with 500 wave components (——), 5000 wave components (——) and 50000 wave components (——). As the number of wave components increases the drift velocity of the wavemaker reduces due to wave interactions. When the number is sufficiently large, it results in a 'constant' mean deviation of the wavemaker, which can then be removed from the control signal (——).

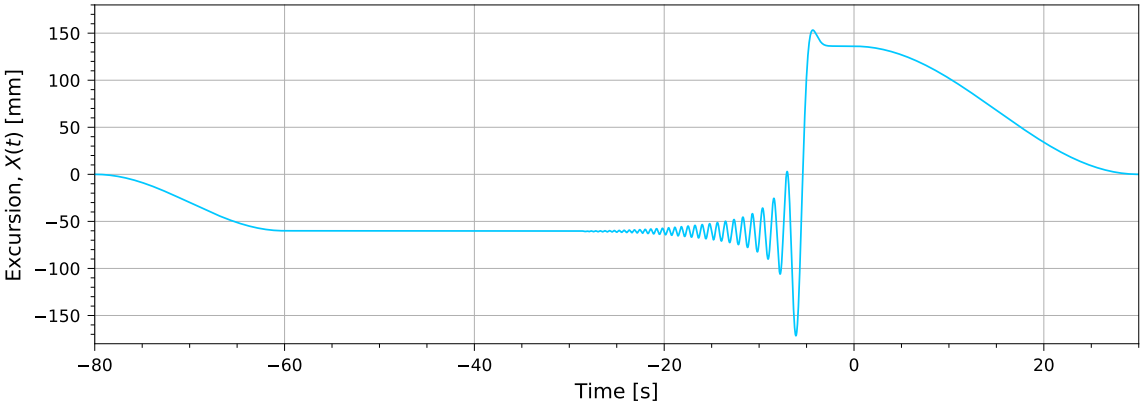

Figure 3.3: Wavemaker control signal combining the zero-amplitude requirement at both ends and the offset feature to deal with the asymmetry of the signal when it is over the maximum amplitude.

the maximum backward motion. Due to this large asymmetry of the control signal, a feature was included in the control signal algorithm that attaches a sinusoidal signal to the beginning of the control signal, slowly moving the wavemaker to an offset zero-position, allowing larger focused waves to be created, see Figure 3.3.

Chapter 4

Sources of variability

Repeatability issues in wave focusing techniques are quite often mentioned in the literature. Bogaert (2018) concluded that: *It was found to be a challenge to generate repeatable global flows due to (1) the inability of the piston to mechanically follow the control signal, (2) the lack of accuracy in measuring the water depth due to low frequency waves in the flume; and (3) the effect of wind in wave propagation*. Fernández et al. (2014) said: *The problem is that when a wave packet containing different wave frequencies is generated, the waves interact and new components that are not satisfying the linear dispersion relation are created. This means that small changes in the associated wavemaker control signal lead to large and unpredictable changes in the generated focused wave*.

It is clear from these statements that wave focusing is highly sensitive to small variations in the involved variables. It is therefore of crucial importance for the repeatability of breaking waves not only to identify these variables but to evaluate their relative importance in the wave focusing process and to provide effective means for their correction when possible.

The entire process of wave generation using a wave focusing technique has been covered in the previous chapters. The sources of variability can be identified by looking at this process from the generation of the first set of waves, with completely still water in the tank, until the moment a second test is carried out. An initial evaluation of the variables involved in wave generation and wave propagation resulted in four sources of variability:

1. Inaccuracy of the wavemaker motion,
2. uncertainty in the water depth measurements,
3. long bounded waves (seiching); and
4. residual currents.

Each source of variability is assessed in the present chapter in a similar way: the variability coming from these sources is introduced in the wave propagation and generation algorithm by means of linear theory. The objective is to derive the wavelets resulting from wave generation and propagation including variability effects and compute the error w.r.t. the undisturbed wavelet. The theoretical criteria of repeatability is also defined—the theoretical maximum error of a focused wave to be considered repeatable—which is then used to specify the experimental conditions to obtain repeatable results.

4.1 Wave characteristics

During a preliminary test campaign with Olivier Kimmoun in the MWL, a set of waves had been selected for future research work in the facility. These waves had similar characteristics: a peak period, T_{peak}, around 2.2 seconds, wave crest heights, H_{c}, ranging from 160 to 180 millimeters and the focal point spread around 10 meters to have different breaking wave shapes. To obtain meaningful results from the theoretical evaluation of the sources of variability, three waves have

been chosen based on the typical characteristics of the waves generated during these tests, only varying the wave crest height, Table 4.1.

Table 4.1: Wave characteristics used in the theoretical evaluation of the sources of variability presented in the following sections.

H_c	T_{peak}	β_l	β_h	x_f
mm	s	–	–	m
$[150, 170, 200]$	2.2	0.5	0.45	10.0

4.2 Inaccuracy of the wavemaker motion

The wavemaker is essential and the most important element in wave generation and wave focusing. Its importance in global flow repeatability relies in the distance to the focal point and the focal time. In the MWL flume the focal point is at approximately 10m from the wavemaker and the focal time is about 60s. This means that waves of a few centimeters in wavelength, for instance, have to propagate a distance three orders of magnitude larger to meet with other wave components in an event that takes place in milliseconds. Additionally, wave-wave interactions occur while waves propagate and non-linearities become important when the breaking wave is building up. Altogether, a slight difference in the paddle motion might lead to a large difference in the focused wave. A numerical evaluation of the variability introduced by the wavemaker is, therefore, a tough task. The reason is that the problem should include the description of the paddle motion and statistics of the error, wave generation—including the generation of spurious waves—and wave propagation considering wave-wave interactions and non-linearities.

To overcome its complexity, the problem was rethought: instead of considering the wavemaker motion as a source of variability of unknown magnitude, the design requirements of the wavemaker motion error were used to establish the uncertainty of the wavemaker motion, linking in this way theory and experiments. This simplifies the problem enormously: the uncertainty in wave generation can be used to derive a control signal that deviates the most from the original, that is then propagated by means of linear theory to the focal point. The error of the resulting wavelet w.r.t. the Ricker wavelet (not affected by variability) determines the 'maximum' error due to wavemaker motion uncertainty. Nevertheless, the 'maximum' error is expected to be smaller than if derived with non-linear theory as non-linearities would further deviate wave components. Though this offers one advantage: as the error is smaller than expected, it can be used to derive the repeatability criteria with a 'safety' factor. It will be further explained in the following sections.

4.2.1 Wavemaker motion design requirements

MARIN determined a series of design acceptance values from the results of the SLOSHEL project, function of the steering signal amplitude, which are given in Table 4.2. These values represent the maximum average motion error of the wavemaker design over a period of 5 seconds and were derived from the analysis of the repeatable impact-pressure tests performed by Bogaert (2018).

4.2.2 Repeatability criteria

One of the most challenging tasks during the project was the definition of the repeatability criteria: when is a breaking wave (or its global flow) considered to be repeatable. From the multiple discussions held with researchers in the topic, the conclusion is that there is no clear consensus on the repeatability criteria and that it is dependent on its final application. Ultimately, the MWL will be studying the effects of the development of crest instabilities on the impact pressures and the role environmental conditions (pressure, temperate, gas composition...) have on it. Clearly, the global wave shape must be *similar enough* to exclude wave generation and wave propagation from the obtained variability. Only then, conclusions about crest instabilities and environmental conditions could be drawn.

By establishing the maximum error of the wavemaker, which can be taken as the wavemaker motion uncertainty, MARIN also sets the uncertainty of the wavelet at the focal point since the error can be propagated to the focal point. This means that, if all other sources of variability were

Table 4.2: Maximum allowable average motion error vs. steering signal amplitude.

Steering signal amplitude mm	**Average motion error over 5 seconds** mm
0.25	0.025
1.00	0.075
2.00	0.100
5.00	0.175
10.0	0.25
20.0	0.30
50.0	0.40
Maximum amplitude	0.50
At zero positions	0.025

mitigated, there will always be some variability coming from the paddle motion that cannot be controlled—taking a measuring equipment as an analogy, the wavemaker uncertainty would be the resolution uncertainty of the equipment. In this context, it was decided that repeatability is achieved when the errors coming from all the sources of variability are smaller than the paddle motion uncertainty—or when the total measurement error is below the resolution uncertainty in the analogy.

4.2.3 Wavemaker motion uncertainty

The maximum wavemaker motion errors presented in Table 4.2 were used to derive the wavemaker uncertainty at the focal point. Firstly, the undisturbed wavemaker control signal was computed for each of the waves defined in section 4.1, see Figure 4.1. Then, the uncertainty region of the control signal was determined from the maximum wavemaker motion errors and a second wavemaker control signal was computed that deviates the most from the undisturbed signal, Figure 4.2. Lastly, both control signals were propagated through the flume resulting in two wavelets: the Ricker wavelet and the wavelet of maximum paddle motion error, Figure 4.3. In this last figure it is also shown the elevation errors of both wavelets and the absolute cumulative error. The average elevation error of the wavelet due to the maximum paddle motion error can be computed by dividing the cumulative error over its integration time. Instead of using an arbitrarily chosen integration time, like 5 seconds in Table 4.2, it was chosen a characteristic time of the wave, its peak period. As can be seen in the figure, the peak period covers an area where the 99.9% of the total cumulative error can be found and, additionally, the cumulative error curve is approximately linear; so it is reasonable to define the maximum time-averaged error as:

$$\bar{\epsilon}_{\mathrm{wlet,max}} = \frac{\epsilon_{\mathrm{cum}}(T_{\mathrm{peak}}/2) - \epsilon_{\mathrm{cum}}(-T_{\mathrm{peak}}/2)}{T_{\mathrm{peak}}} \tag{4.1}$$

and the theoretic repeatability criterion as:

$$\bar{\epsilon}_{\mathrm{sources}} < \bar{\epsilon}_{\mathrm{wlet,max}} \tag{4.2}$$

The data from Figure 4.3 gives the following maximum errors function of the wave crest height:

Table 4.3: Maximum time-averaged wavelet errors derived by linear theory for $T_{\mathrm{peak}} = 2.2\mathrm{s}$.

	Wave crest height			
	150	170	200	mm
$\bar{\epsilon}_{\mathrm{wlet,max}}$	$0.386(0.26)$	$0.405(0.24)$	$0.433(0.22)$	$\mathrm{mm}(\%H_{\mathrm{c}})$

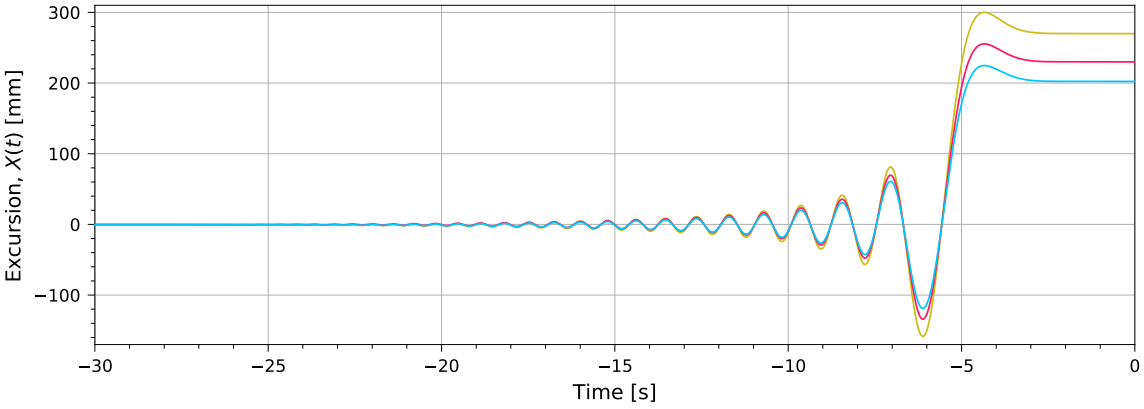

Figure 4.1: Wavemaker control signals for the generation of three waves with the same peak period, $T_{\text{peak}} = 2.2\text{s}$, and different wave crest height: $H_{\text{c}} = 150\text{mm}$ (—), $H_{\text{c}} = 170\text{mm}$ (—) and $H_{\text{c}} = 200\text{mm}$ (—).

The 'safety' factor mentioned at the beginning of the section can now be explained. The repeatability criterion, eq. (4.2), requires that the average error introduced in the wavelet by other sources of variability must be smaller than the maximum average error introduced by the wavemaker motion uncertainty to consider two tests repeatable. Nevertheless, linear theory was used to obtain the maximum average error introduced by the wavemaker. This error is, therefore, smaller than the error derived from a nonlinear theory as wave interactions would lead to larger errors as stated by Fernández et al. (2014). This means that:

$$\bar{\epsilon}_{\text{sources}} < \bar{\epsilon}_{\text{wlet,max,linear}} < \bar{\epsilon}_{\text{wlet,max,nonlinear}} \tag{4.3}$$

4.2.4 Experimental repeatability criterion

The repeatability criterion derived in the previous section presents a way to theoretically compute the limits in the sources of variability—how much a source of variability needs to be controlled experimentally to expect repeatable results. However, it cannot be used to directly determine experimental repeatability because the criterion is defined at the focal point, where nonlinearities become important and the breaking wave is no longer a smooth wavelet but an overturning wave. As the wave propagation algorithm, see chapter 5, allows to compute the wave elevation at any position in the flume given the control signal, the control signals derived shown in Figure 4.2 can be used to compute the wave elevations at the positions where the experimental measurements of the wave elevation are taken, at 5.2 and 7.7 meters from the wavemaker, $x = (-4.8, -2.3)\text{m}$, see Figure 4.4; which can be used to establish the experimental repeatability criterion.

Perlin and Bustamante (2016) presented *a method for the quantitative comparison of two signals, applicable to temporal and/or spatial extent in one or two dimensions*. The method returns a similarity parameter, Q, that has been normalized so that it lies between zero and one. When the quotient is zero both surfaces (signals) are in perfect agreement, whereas a value of one indicates perfect disagreement. The method is based on the Sobolev norm of the Fourier-space representation in conjunction with a normalizing denominator via the triangle inequality. The normalized error or similarity parameter, Q, is defined as:

$$Q(f_1, f_2) = \frac{\left(\int |F_1(\omega) - F_2(\omega)|^2 \, \mathrm{d}\omega \right)^{1/2}}{\left(\int |F_1(\omega)|^2 \, \mathrm{d}\omega \right)^{1/2} + \left(\int |F_2(\omega)|^2 \, \mathrm{d}\omega \right)^{1/2}} \tag{4.4}$$

where $F(\omega)$ is the usual Fourier transform of $f(t)$.

Note that the definition takes advantage of using the phase information as well as the amplitude in the frequency domain to quantify the difference between two signals.

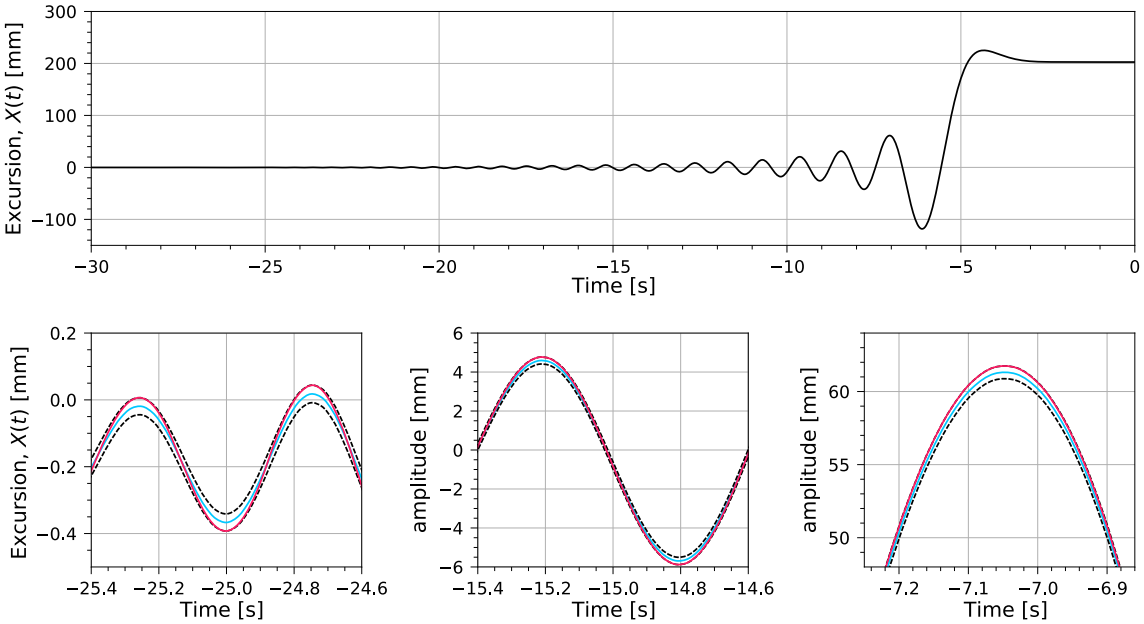

Figure 4.2: Derivation of the control signal used to compute the maximum error at the focal point due to paddle motion uncertainty. The maximum wavemaker motion error (- - -) is computed from the original Ricker control signal (——) to derive a control signal that maximizes the error without applying a phase shift (——).

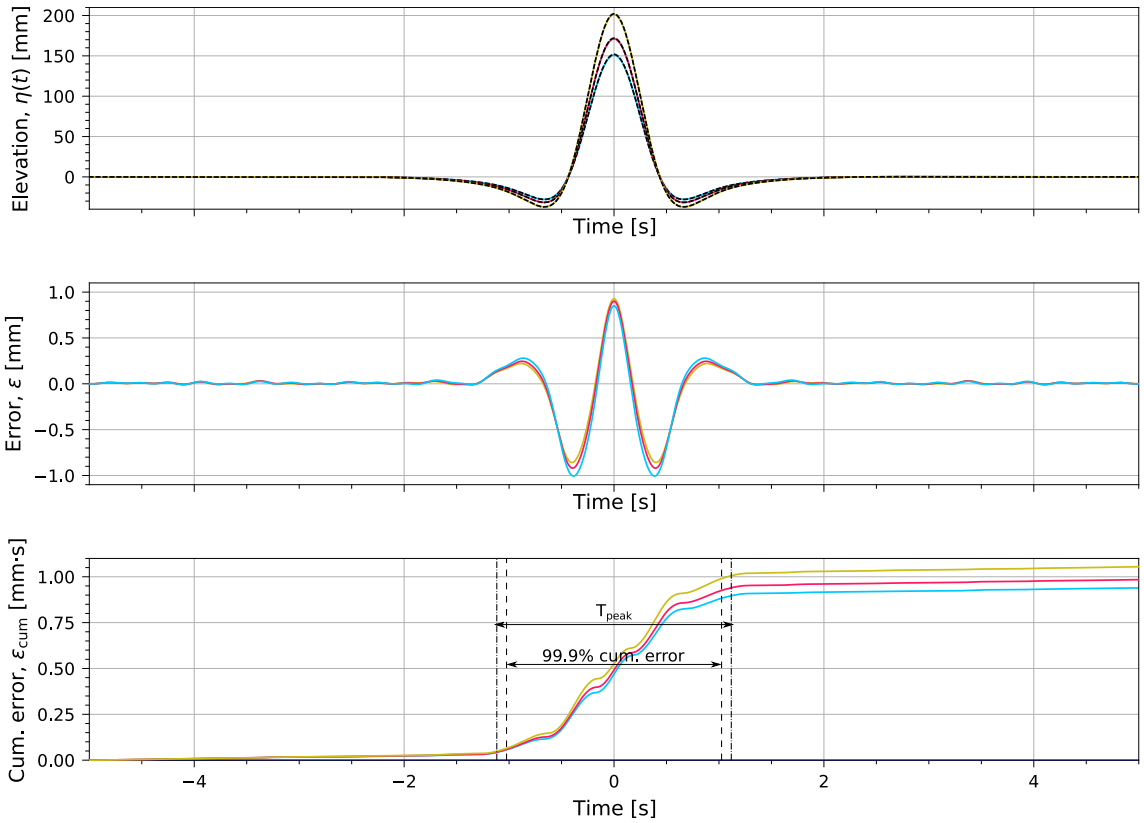

Figure 4.3: Comparison of the wavelets obtained from the undisturbed control signal and considering the design maximum error of the wavemaker: $H_c = 150\text{mm}$ (——), $H_c = 170\text{mm}$ (——), $H_c = 200\text{mm}$ (——), wavelet from max. wavemaker motion error (- - -). The elevation error is plotted due to the small differences obtained, $< 1\text{mm}$. The absolute cumulative error is also shown, from which the average elevation error, as defined in Table 4.2, can be computed over the peak period.

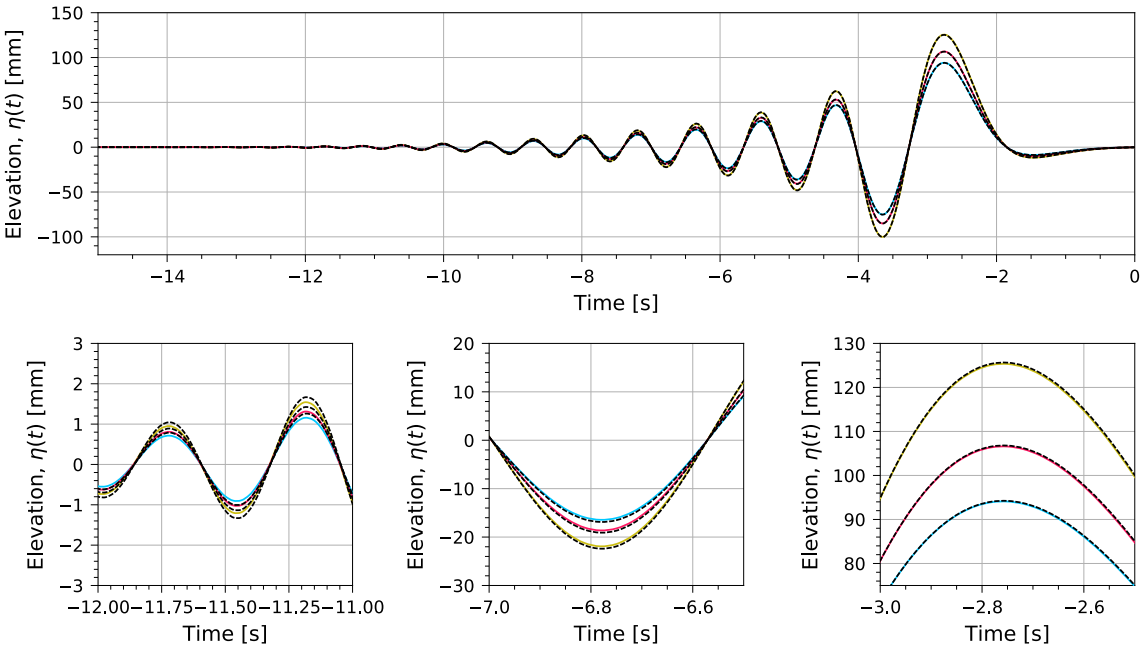

(a) Free surface elevations at $x = -4.8\text{m}$.

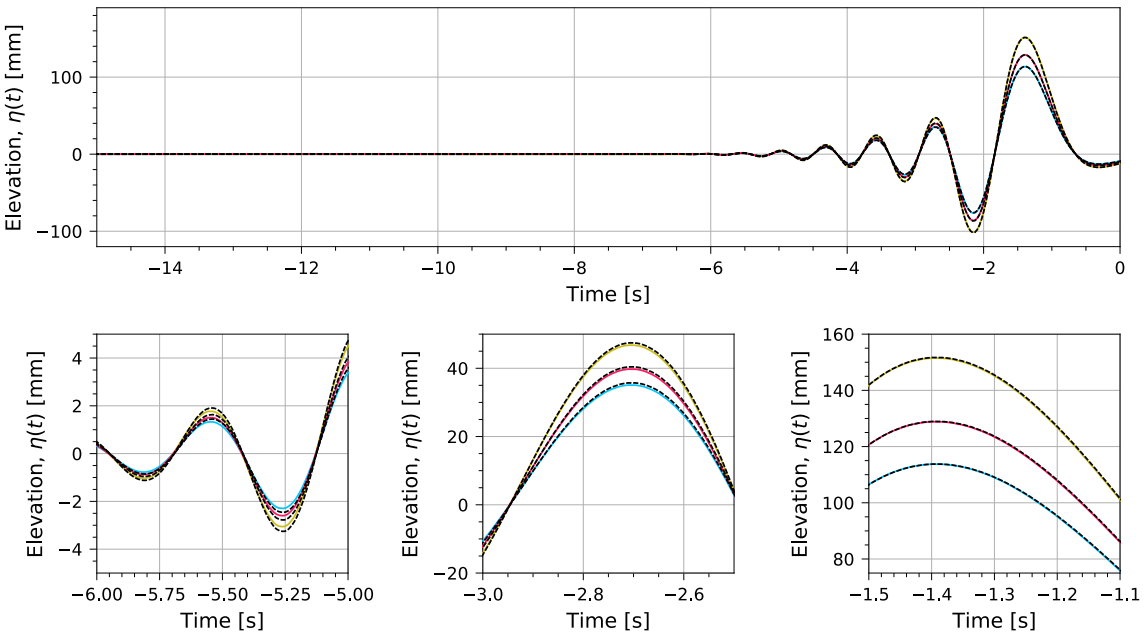

(b) Free surface elevations at $x = -2.3\text{m}$.

Figure 4.4: Theoretical wave elevations at the positions where the experimental measurements are taken, 4.8m and 2.3m from the impact wall. The solid lines represent the wave elevations from the Ricker spectrum for $H_c = 150\text{mm}$ (——), $H_c = 170\text{mm}$ (——) and $H_c = 200\text{mm}$ (——). The dashed lines the elevations obtained from the control signal of the maximum paddle motion error (- - -). Three zoomed-in plots have been included at each position to perceive the small differences in wave elevations due to the maximum motion error of the wavemaker design.

Table 4.4: Maximum similarity parameter, $Q_{\max}$, derived by linear theory for $T_{\text{peak}} = 2.2\text{s}$ at two intermediate positions along the flume to obtain repeatable focused waves.

		Wave crest height			
		150	170	200	mm
$Q_{\max}$	$x = -4.8\text{m}$	0.003	0.003	0.003	—
	$x = -2.3\text{m}$	0.003	0.003	0.003	—

The application of the expression to the wave elevations computed at the intermediate positions along the flume, Figure 4.4, yields the similarity values shown in Table 4.4.

These results clearly show that the differences in wave propagation remain constant along the flume by using linear theory. $Q_{\max}$ is the maximum 'dissimilarity' due to the design requirements of the wavemaker. Therefore, the repeatability criterion, eq. (4.2), can be rewritten in terms of the similarity parameter to evaluate experimental repeatability:

$$Q_{\text{sources}} \leq Q_{\max} \tag{4.5}$$

as:

$$Q_{\text{exp}} = Q_{\text{wm}} + Q_{\text{sources}} \tag{4.6}$$

and:

$$Q_{\text{wm}} \leq Q_{\max} = 0.003 \tag{4.7}$$

then:

$$Q_{\text{exp}} \leq 2Q_{\max} = 0.006 \tag{4.8}$$

This value has been used in chapter 6 to evaluate the experimental wave focusing repeatability.

4.3 Uncertainty in the water depth measurements

If the wavemaker was considered the most important element in wave generation, wave focusing and wave repeatability; the water depth is also a very sensitive parameter. In chapters 2 and 3 the (linear) theory in wave focusing and wave generation was presented. A common parameter in the expressions defining the theory is the water depth. It appears in wave generation through the transfer function and in wave propagation through the dispersion relation—only in deep water conditions wave propagation would be independent of the water depth. In linear theory, water depth affects wave propagation by altering the wave speed of the different components. Higher frequencies are less sensitive to a change in water depth because they 'are' in a deep water regime. On the other hand, lower frequencies are more sensitive to a water depth change, speeding up when the water depth is increased, see Figure 4.5a. Water depth also affects wave generation by increasing the amplitude of the generated wave. Higher frequencies are less affected by water depth changes because the small wavenumbers dominate over the water depth in eq. (3.10) and the paddle motion tends to zero, see Figure 4.5b.

4.3.1 Evaluation of the variability

The procedure for the evaluation of the variability introduced by uncertainties in the water depth measurements is similar to the method used for the evaluation of the paddle motion uncertainties. The goal is to obtain the wavelet resulting from the control signal considering the uncertainties in the water depth.

The control signal derived from the Ricker spectrum at the design water depth, $h = 400\text{mm}$, is used to compute the wave train that will propagate to the focal point—multiplying by the transfer function, eq. (3.10). Although the water depth used in the transfer function would range from 395 to 405 millimeters, i.e., $h \in 400 \pm 5\text{mm}$. The wave train is then propagated by linear theory to

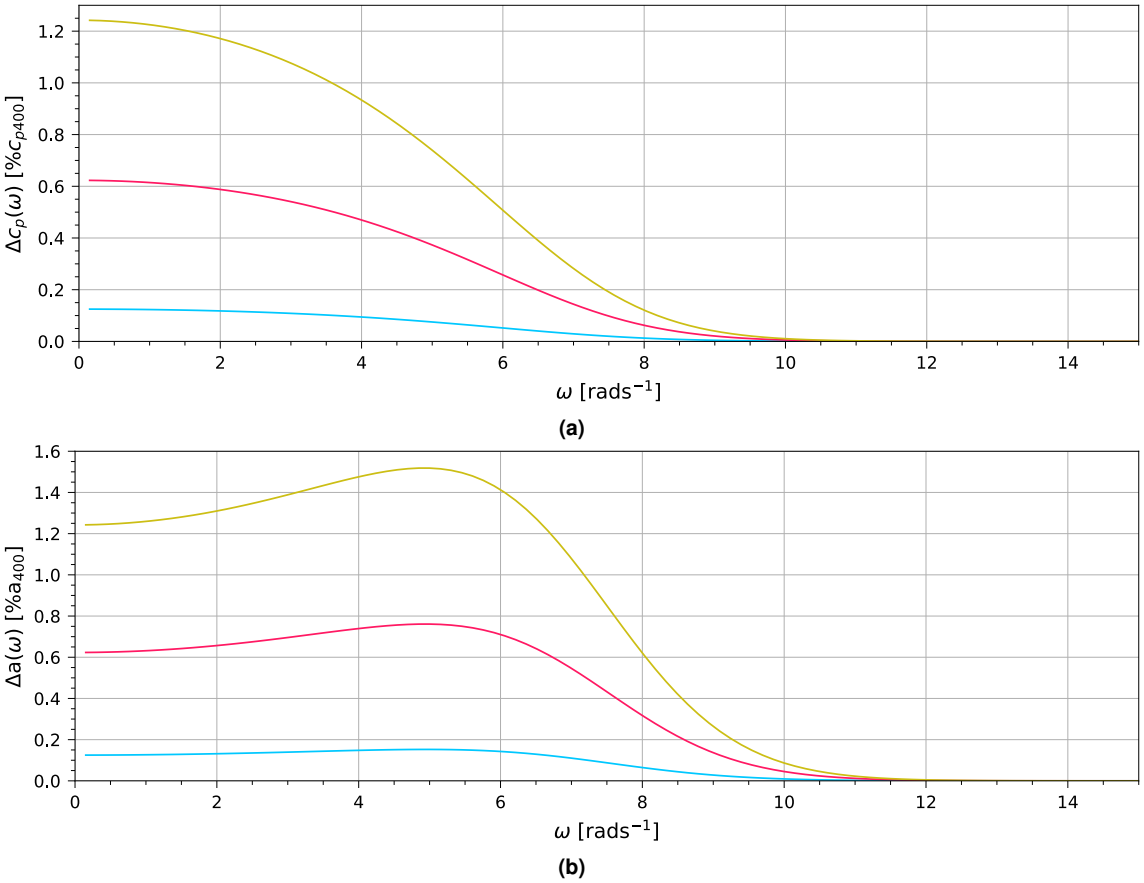

Figure 4.5: Effects of the water depth on the phase velocity **(a)** and in the amplitude of the generated wave component **(b)** in function of the wave frequency for $h = 401\text{mm}$ (—), $h = 405\text{mm}$ (—) and $h = 410\text{mm}$ (—). Shown in percentage of the phase velocity and wave amplitude at $h = 400\text{mm}$.

the focal point, with its corresponding water depth, resulting in different wavelets which are then compared in the same way as the paddle motion uncertainty, Figure 4.3. The expression used to obtain the wavelets considering water depth uncertainties is[1]:

$$\eta_{\text{wlet}}(h,t) = \sum_{i=1}^{n} a_i \exp\left[i\Big((k_{i,h} - k_{i,400})x_{\text{f}} - \omega_i t\Big)\right] \cdot \frac{\zeta(h)}{\zeta(400)} \tag{4.9}$$

where $k_{i,400}$ and $k_{i,h}$ are, respectively, the wavenumbers obtained at the design water depth and considering a Δh between ± 5 millimeters and $\zeta(400)$ and $\zeta(h)$ are the transfer functions from flap excursion to wave elevation, eq. (3.10), at the design water depth and Δh.

The results of applying the equation to five water depths are depicted in Figure 4.6 for a 200 millimeter wave crest height. The first thing that draws the attention is the deviation that water depth introduces: approximately five times larger than the maximum allowable error derived in the previous section for only 2 millimeters difference, $\Delta h = 2\text{mm}$; and over ten times larger for 5 millimeters difference, $\Delta h = 5\text{mm}$, which clearly shows the importance of the water depth and how carefully and precise it must be measured and controlled. Also note that the cumulative errors at $h = 395\text{mm}$ and $h = 405\text{mm}$ are not exactly the same. Increasing/reducing the water depth leads to differing errors due to less/more wave components 'feeling' the bottom of the flume, i.e., the wave components are displaced towards a deep/shallow water regime respectively. Lastly, the effects of water depth on the wave celerity as shown in Figure 4.5a are also appreciable. Increasing the water depth shifts the wavelet to the left (negative times) which means the focused wave arrives sooner at the focal point, therefore propagating faster. Another conclusion that can

[1] The mathematical derivation of the equation can be found in chapter 5.

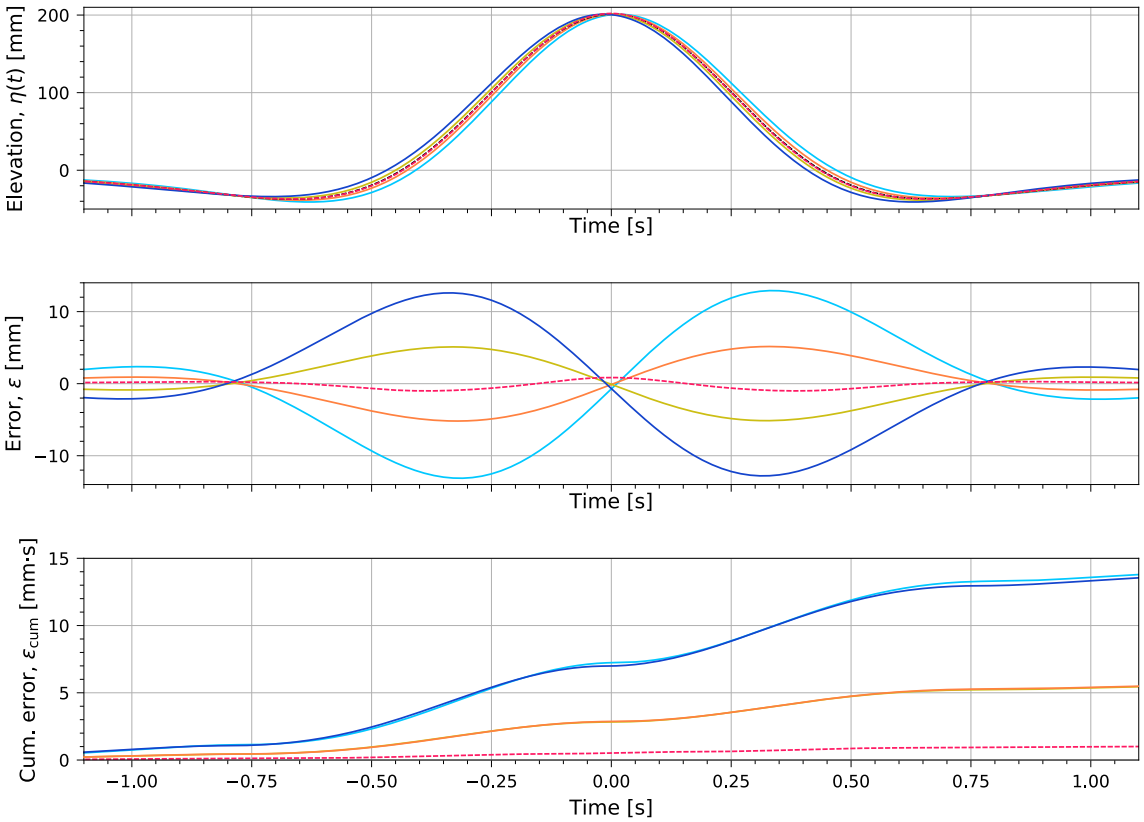

Figure 4.6: Resulting wavelets for $H_c = 200\text{mm}$ after adding a $\Delta h = -5\text{mm}$ (——), $\Delta h = -2\text{mm}$ (——), $\Delta h = 0\text{mm}$ (- - -), $\Delta h = 2\text{mm}$ (——) and $\Delta h = 5\text{mm}$ (——) to the design water depth. The maximum error computed in previous section (- - -) is also shown to give insight about the required control over the water depth.

be drawn combining Figures 4.5a and 4.6 is that the focal point shifts with the water depth. The propagation velocity of the lower frequencies is more sensitive than the higher ones to a change in the water depth, which means that the focal time of the higher frequencies remains almost constant, whereas the focal time of the lower frequencies reduces as the water depth increases and vice versa. This implies that the waves must meet before/after the focal point depending on the water depth change.

The averaged errors of the wavelets over a peak period are shown in Table 4.5. An important result from the table is that water depth variability is a linear function of the wave crest height, which means that the error can be derived for any intermediate wave crest height multiplying the normalized error by the wave crest height.

Table 4.5: Time-averaged wavelet errors due to water depth variability.

Crest Height	**Water depth**											
mm	395	396	397	398	399	400	401	402	403	404	405	mm
150	4.52	3.61	2.70	1.80	0.90	0.00	0.89	1.78	2.66	3.54	4.42	mm
	3.01	2.41	1.80	1.20	0.60	0.00	0.59	1.19	1.78	2.36	2.94	$\%H_c$
170	5.12	4.09	3.06	2.04	1.02	0.00	1.01	2.02	3.02	4.02	5.01	mm
	3.01	2.41	1.80	1.20	0.60	0.00	0.59	1.19	1.78	2.36	2.94	$\%H_c$
200	6.03	4.81	3.60	2.40	1.20	0.00	1.19	2.37	3.55	4.73	5.89	mm
	3.01	2.41	1.80	1.20	0.60	0.00	0.59	1.19	1.78	2.36	2.94	$\%H_c$

From Table 4.3 and 4.5 the maximum uncertainty in the water depth measurement and control,

in the absence of any other source of variability, can be obtained by means of a simple linear interpolation, Table 4.6.

Table 4.6: Maximum uncertainty in water depth measurement and control, $U_{\mathrm{h,max}}$, in the absence of other sources of variability, to satisfy the repeatability criterion defined in the previous sections.

	Crest Height			
	150	170	200	mm
$U_{\mathrm{h,max}}$	0.43	0.41	0.37	mm

4.4 Long bounded waves—seiching

Seiches are long-period standing oscillations in an enclosed basin or in a locally isolated part of a basin, commonly initiated from atmospheric processes or from the non-linear interaction of waves or swell. In fact, wave generation in an enclosed flume will cause seiching due to wave reflections or wave grouping effects that can transfer wave energy to low frequencies (Haller and Dalrymple, 2001). While the term typically used to describe the free-surface oscillations occurring in storage tanks or basins is *sloshing*, in this work the term *seiching* will be used instead. Sloshing refers to any movement of liquid inside another object. However, the motion under consideration in this section occurs at the natural resonant periods of the basin, known as seiches.

The periods of the seiches are determined by the basin geometry. The mode with lowest frequency is referred to as the fundamental mode (Mei, 1989). These 'eigen' frequencies are independent of the external mechanism forcing the oscillation. They are a fundamental property of a particular basin. In closed basins, energy losses of seiches are mostly associated with dissipation (Rabinovich, 2010). Beaches at the end of wave flumes provide a mechanism to dissipate the wave energy. Nevertheless, the extremely long period and small amplitude of these standing waves makes beaches highly inefficient against them. As a consequence, these waves stay in the wave flume for a long time, altering the conditions found in still water by: (1) making the local water depth a function of time and the longitudinal position in the flume, $h(x,t)$; and (2) pulling mass from one end of the flume to the other due to the oscillatory motion, therefore inducing a current.

4.4.1 Eigen periods

The elevation of a standing wave, η_{s}, in a closed, long and narrow rectangular basin of length, L, and uniform depth, h, has a single trigonometric form (Wilson, 1972):

$$\eta_{\mathrm{s}}(x,t) = a_{\mathrm{s}} \cos(kx) \cos(\omega t) \tag{4.10}$$

As shown in chapter 2, the angular frequency and wave number are linked through the following relation:

$$c_{\mathrm{p}} = \frac{\omega}{k} \tag{4.11}$$

where c_p is the long-wave phase speed derived from the Airy wave theory for shallow water regime, eq. (2.22)—shallow water can be assumed because the wavelength is much longer than the water depth.

The impermeability condition at $x = 0$ and $x = L$ yields the wave numbers:

$$k = \frac{\pi}{L}, \quad \frac{2\pi}{L}, \quad \frac{3\pi}{L}, \ldots, \frac{n\pi}{L} \tag{4.12}$$

From where the Merian's expression, for the natural periods of a standing wave in a rectangular basin of uniform depth, is found combining both relations, eq. (4.11) and eq. (4.12) (Rabinovich, 2010):

$$T_n = \frac{2L}{n\sqrt{gh}} \quad \text{where: } n = 1, 2, 3, \ldots \tag{4.13}$$

Table 4.7: Eigen periods of the MWL flume for $h = 400\text{mm}$.

	Mode			
	$n = 1$	$n = 2$	$n = 3$	
Period	10.1	5.0	3.4	s

This relation shows that the longer the basin length or the shallower the basin depth, the larger the seiche period. The fundamental mode, $n = 1$, and the odd modes are antisymmetric: when at one side the water is at its maximum the opposite side is at its minimum. This means that a nodal point is found at $x = L/2$. The nodal points or lines are those positions where $\eta(x, t) = 0$ for all time, see Figure 4.7.

The eigen periods of the first three seiche modes are shown in Table 4.7.

4.4.2 Seiching-induced currents

In addition to the disturbance of the free surface, seiches induce a current due to mass being pulled from one side of the flume to the other. The maximum seiche-induced current is located at the nodal point of the seiche and can be roughly estimated by eq. (4.14)—conservation of momentum (Rabinovich, 2010).

$$V_{\max} = a_{\text{s}}\sqrt{\frac{g}{h}} \tag{4.14}$$

Assuming an amplitude of the first seiche mode, $a_{\text{s}} = 0.5\text{mm}$, and the design water depth, $h = 400\text{mm}$, results in $V_{\max} \approx 2.5\text{mms}^{-1}$; which might seem a small current velocity. However, the last generated wave reaches the focal point in approximately 5 seconds, see Figure 4.2 for instance, which is half the period of the first seiche mode of the MWL flume. This means that, in the presence of a seiche in the flume, the last wave might propagate in an opposing or following current at all time. A (too) simple calculation, multiplying the focal time of the last wave by the maximum velocity of the seiche-induced current, results in a shift of the focal point of $\Delta x_{\text{f}} = V_{\max} t_{\text{f}} \approx 12\text{mm}$.

Potential theory can be used to determine the velocity field of a seiche mode. A standing wave is formed by the superposition of two waves, with the same frequency, propagating in opposite directions. As superposition is valid in potential theory, the velocity potential of the standing wave is found adding up the velocity potentials of both waves. Assuming shallow water, the velocity potential of the waves is:

$$\Phi_{\text{r}} = \Im\left\{a_{\text{r}}\frac{1}{kh}\frac{\omega}{k}\exp\left[i(kx - \omega t)\right]\right\} \tag{4.15}$$

$$\Phi_{\text{l}} = \Im\left\{a_{\text{l}}\frac{1}{kh}\frac{\omega}{k}\exp\left[i(-kx - \omega t)\right]\right\} \tag{4.16}$$

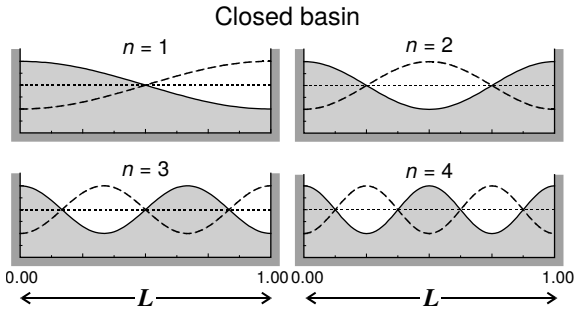

Figure 4.7: Surface elevations for the first four seiche modes in a closed rectangular basin of uniform depth (Rabinovich, 2010).

where the subindices r and l refer to a right and left propagating wave, repectively.

Superposition yields the velocity potential of the standing wave:

$$\Phi_\mathrm{s} = \Phi_\mathrm{r} + \Phi_\mathrm{l} \tag{4.17}$$

$$\Phi_\mathrm{s} = a_\mathrm{s} \frac{1}{kh} \frac{\omega}{k} \cos(kx) \sin(-\omega t) \tag{4.18}$$

and its derivative w.r.t. the x-axis gives the horizontal velocity in the flow:

$$u_x(\boldsymbol{x}, t) = \frac{\partial \Phi_\mathrm{s}}{\partial x} \tag{4.19}$$

$$u_x(\boldsymbol{x}, t) = a_\mathrm{s} \frac{\omega}{kh} \sin(kx) \sin(\omega t) \tag{4.20}$$

As shallow water was assumed, the horizontal velocities are depth-independent and the result of eq. (4.20) is equal to the depth-averaged horizontal velocity.

4.4.3 Evaluation of the variability

The procedure for the evaluation of the variability introduced by a seiche in the wave flume is similar to the method used in the previous sections. The objective is the same: obtaining the wavelet at the focal point resulting from propagating the wave train generated by the control signal. This time, the fundamental seiching mode is placed in the flume while waves are being generated and propagated—it was assumed that higher modes damp much faster than the fundamental mode, being the latter the main source of seiching variability.

The control signal derived from the Ricker spectrum at the design water depth, $h = 400\mathrm{mm}$, is used to compute the wave train that will propagate to the focal point. However, the process is not as straightforward as it was in the previous section. It is assumed that the fundamental mode was not completely damped and, therefore, the water depth at the wavemaker oscillates around the design water depth.

$$h_\mathrm{wm}(t) = h_\mathrm{d} + \eta_\mathrm{s}(-x_\mathrm{f}, t) \tag{4.21}$$

Thus, the wave train generated by the control signal considering the fundamental seiching mode is determined by:

$$\eta_\mathrm{wm}(t) = \sum_{i=1}^{n} a_i \exp\left[i(-k_{i,400} x_\mathrm{f} - \omega_i t)\right] \frac{\zeta(h_\mathrm{wm}(t))}{\zeta(400)} \tag{4.22}$$

At this point, a new phenomenon must be introduced: the Doppler shift of the frequency of a propagating wave in the presence of a current. A constant current (in depth and length) adds up to the flow, increasing or decreasing the horizontal fluid velocities in a way that two people, one of them in a stationary frame of reference and the other one moving with the current, would measure two different wave periods. When the current is constant in depth but its magnitude depends on the longitudinal position—as is the case of a seiche-induced current—the horizontal fluid velocities are accelerated in the direction of the gradient of the current—the wave elevation would also be affected due to mass conservation. Consequence of the acceleration, the wave period is progressively increasing or reducing as the wave propagates. However, for an observer from a stationary frame of reference, it is the wave length which gets shorter/longer. This means that, in a Lagrangian frame of reference, the Doppler shift occurs in the wave period, whereas in an Eulerian frame of reference the shift occurs in the wave length, see Figure 4.8.

The combined effects of seiching were included in the wave propagation algorithm by allowing the wave to change its wavenumber as it propagates in an oscillating water depth and in the presence of a current. The equation to propagate the wave train, $\eta_\mathrm{wm}(t)$, to the focal point is[2]:

$$\eta_\mathrm{wlet}(t) = \sum_{i=1}^{n} a_i \exp\left[i\left(\int_{-x_\mathrm{f}}^{0} k_i(x,t)\,\mathrm{d}x - \omega_i t + \phi_{i,\mathrm{wm}}\right)\right] \frac{\zeta(h_\mathrm{wm}(t))}{\zeta(400)} \tag{4.23}$$

[2]The mathematical derivation of the equation can be found in chapter 5.

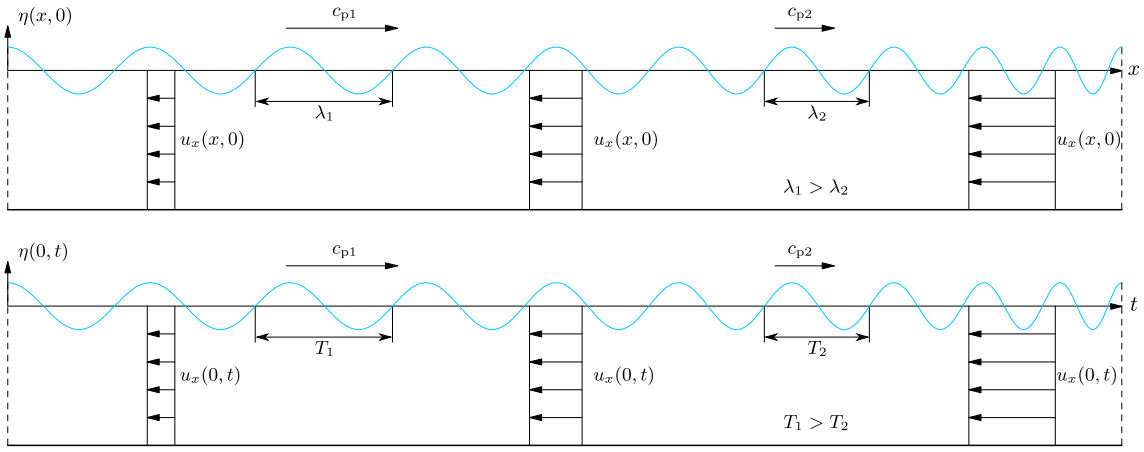

Figure 4.8: Effects of an opposing current—uniform over depth and non-uniform over time/space—in the wave characteristics depending on the frame of reference.

where $k_i(x,t)$ is obtained from:

$$\omega_i = \sigma_i - k_i(x,t)u_x(\boldsymbol{x},t) \tag{4.24}$$

$$\sigma_i^2 = k_i(x,t)g\tanh\left(k_i(x,t)\Big(h_{\mathrm{d}} + \eta_{\mathrm{s}}(x,t)\Big)\right) \tag{4.25}$$

with σ_i the intrinsic frequency, i.e., the frequency of the wave relative to the current; and $\phi_{i,\mathrm{wm}}$ the phase of each wave component at the wavemaker at $t = 0$, which are obtained from the phases of the wave train, $\eta_{\mathrm{wm}}(0)$:

$$\phi_{i,\mathrm{wm}} = -k_{i,400}x_{\mathrm{f}} \tag{4.26}$$

Computing the wavelet requires a numerical method because the dispersion relation is an implicit equation. The domain has been discretized in 1000 elements, which corresponds to a $\Delta x = 10\mathrm{mm}$. The shortest of the wave components, approximately a frequency of $3.5\mathrm{Hz}$, has a wave length of approximately 125 millimeters. Therefore, a discretization at centimeter level ensures having at least 10 integration points per wavelength in all wave components. Bisection method was used to compute the wave numbers and Simpson's rule to integrate the wave numbers along the flume.

The results obtained from including the fundamental seiching mode in wave generation and propagation are depicted in Figure 4.9 for $H_{\mathrm{c}} = 200\mathrm{mm}$. The introduced seiche amplitude ranged from 0 to 5 millimeters. Additionally, the seiche *focal*-phase was set to 0 and $\pi/2$ radians to evaluate the effects of a leading/opposing current in the lower frequencies—it is important to remark that the phase of the seiche is specified at the focal time, $t = 0$, because the initial time of the control signal is not fixed, it can be extended/shortened. Overall, these results show that seiches are less important than the accurate measurement and control of the water depth. The errors from the uncertainties in the paddle motion and from seiching are in the same order of magnitude—although seiches of 5 millimeters amplitude are never found in the flume with typical waiting times (20 minutes), which indicates that seiching is not expected to be a problem in the experimental flume unless wave-wave interactions are highly sensitive to wave-current interactions. It is also found that the errors of a propagating wave train in a seiche with focal phase $\phi_{\mathrm{s}} = 0$ lead to smaller errors than when the focal phase is $\phi_{\mathrm{s}} = \pi/2$. This is in agreement with the results from the evaluation of the water depth uncertainties. A seiche with $\phi_{\mathrm{s}} = 0$ is at its maximum amplitude at the focal time at the focal point. This means that those waves with a focal time smaller than half the period of the seiche will propagate on a free surface elevation that is, at all times, above the mean water level; therefore increasing the mean water depth. The conclusion of the previous section was that an increase in the water depth leads to a smaller error than a decrease, which is also shown in this section.

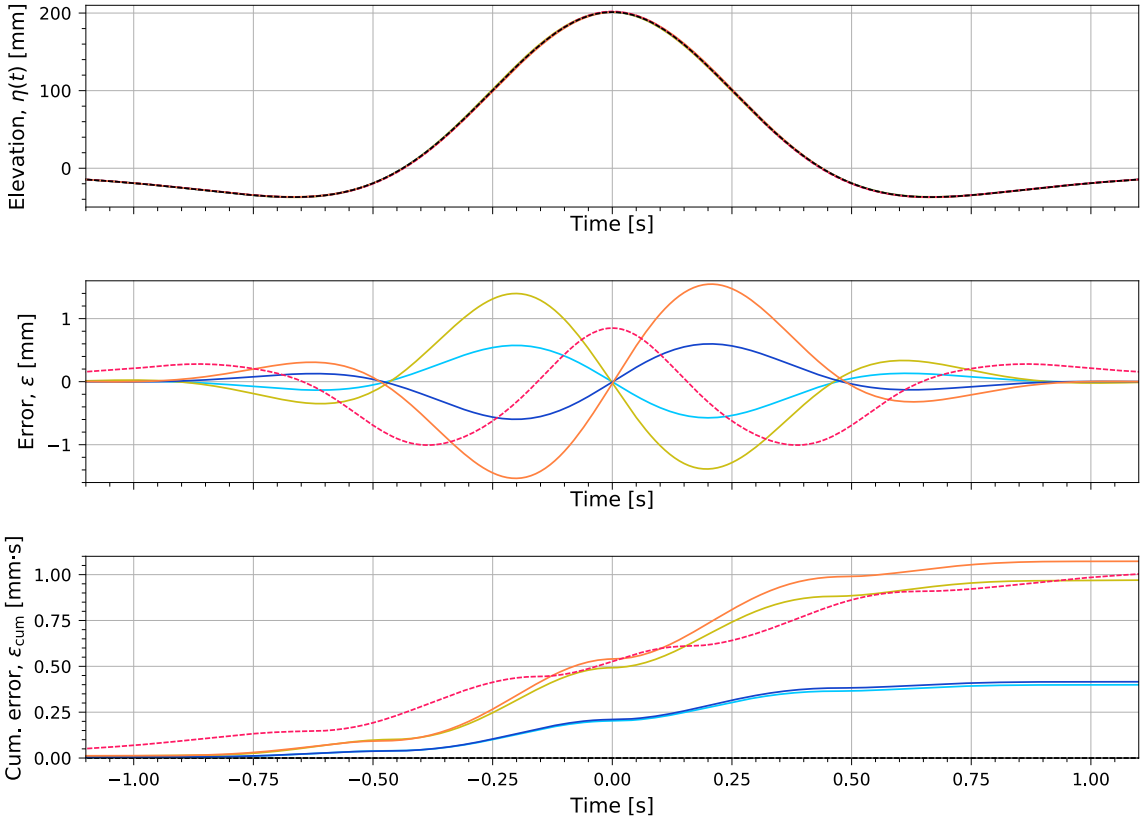

Figure 4.9: Resulting wavelets for $H_c = 200\text{mm}$ after introducing the fundamental seiching mode in the wave propagation algorithm: $a_s = 0\text{mm}$ and $\phi_s = 0$ (- - -), $a_s = 2\text{mm}$ and $\phi_s = 0$ (——), $a_s = 2\text{mm}$ and $\phi_s = \pi/2$ (——), $a_s = 5\text{mm}$ and $\phi_s = 0$ (——); and $a_s = 5\text{mm}$ and $\phi_s = \pi/2$ (——). The maximum error derived from the paddle motion uncertainty (- - -) is shown to give insight about the importance of seiching.

The averaged errors of the wavelets over a peak period are shown in Table 4.8. As can be seen, seiching variability is a linear function of the wave crest height, which means that the error could be derived for any intermediate wave crest height multiplying the normalized error by the wave crest height.

Table 4.8: Time-averaged wavelet errors due to seiching variability.

Crest Height	**Seiche amplitude**											
	$\phi_s = 0$						$\phi_s = \pi/2$					
mm	5	4	3	2	1	0	1	2	3	4	5	mm
150	0.33	0.26	0.20	0.13	0.07	0.00	0.07	0.14	0.21	0.29	0.36	mm
	0.22	0.18	0.13	0.09	0.05	0.00	0.05	0.09	0.14	0.19	0.24	$\%H_c$
170	0.37	0.30	0.23	0.15	0.08	0.00	0.08	0.16	0.24	0.32	0.41	mm
	0.22	0.18	0.13	0.09	0.05	0.00	0.05	0.09	0.14	0.19	0.24	$\%H_c$
200	0.44	0.35	0.27	0.18	0.09	0.00	0.09	0.19	0.28	0.38	0.48	mm
	0.22	0.18	0.13	0.09	0.05	0.00	0.05	0.09	0.14	0.19	0.24	$\%H_c$

4.5 Combined effect of water depth and seiching

The set of equations derived in the previous section can be used to evaluate the repeatability of a focused wave when the effects of seiching and water depth uncertainty are combined. For this, the design water depth, h_d, in eq. (4.21) and eq. (4.25) is taken as $h \in 400 \pm 5\text{mm}$, and the same procedure is followed.

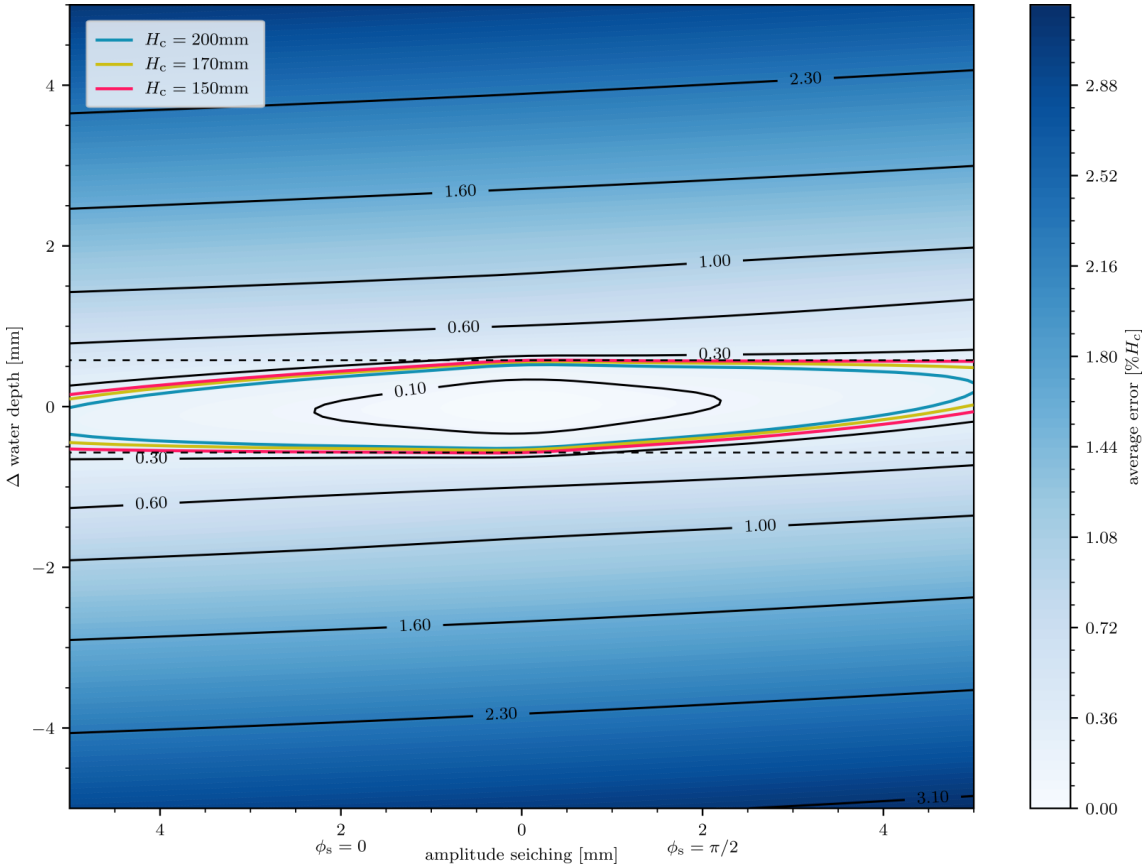

Figure 4.10: Time-averaged wavelet errors due to seiching and water depth uncertainty. The repeatability criteria defined at the beginning of the chapter is also included.

The normalized time-averaged errors of the resulting wavelets are shown in Figure 4.10. These results are in agreement with the conclusions from water depth variability and seiching. The tilt in the contours indicate that seiche–water-depth interaction lead to larger errors when both effects interact constructively. Neglecting the effects on the higher frequencies—shorter waves are barely affected by water depth and the seiching effects average to zero—it can be explained with those wave components whose focal time is shorter than half the period of the seiche, the longer waves of the spectrum. These waves propagate at all times in a leading or opposing current and the mean water depth they propagate on deviates from the design water depth. Thus, when the focal phase of the seiche is $\phi_s = 0$ and the change in water depth is negative, $\Delta h < 0$, the seiche wave induces a positive current increasing the propagation velocity of the wave components; and the water depth change slows them down due to the stronger interaction with the bottom—the effect is exactly the opposite when $\phi_s = \pi/2$ and $\Delta h > 0$. The combined effect is a time-averaged error of the wavelet that is smaller than if seiching and water depth interact constructively, $\phi_s = 0$ and $\Delta h > 0$, or $\phi_s = \pi/2$ and $\Delta h < 0$; which results in inclined contour lines.

The repeatability criterion derived in section 4.2.3 is also included in Figure 4.10. These contour lines clearly show that the importance of seiching in wave repeatability is not as relevant as the accurate control and measurement of the water depth. Nevertheless, an accurate measurement of the water depth cannot be done if the water surface is not completely still. A solution would be to place the measurement device in the nodal point of the fundamental mode, but disturbances of the symmetric modes are unavoidable.

4.6 Residual currents

When a test is carried out in an experimental flume, shear stresses inside the boundary layer—which develops in the vicinity of the walls of the flume due to viscosity—eddy generation from

the breaking wave and the wave impact introduce vorticity to the flow. Swan (1990) investigated the velocity beneath a series of progressive gravity waves breaking in a beach, concluding that: *convection does play an important part within an experimental flume. The vorticity generated at the end conditions is convected backwards with the mass transport velocity.* As a result, *the near shore region progressively influences the entire length of the wave flume. The convective processes eventually dominate the flow behaviour and the assumption of irrotationality breaks down.* However, these conclusions are drawn after 3 hours of wave generation, which gives the energy and time required for vorticity to be convected and develop a drift velocity field in the flume. In the discussion of the results it is stated that: *in the early stages, the motion in the interior of the flow field remains irrotational and therefore the drift velocity is very similar to the back flow predicted by Stokes' solution.*

While the experimental set-up is not the same—the presence of a beach in the breaking region changes the way vorticity is being generated and convected—the time scale difference between these two experiments has been decisive to assume that residual currents due to convected vorticity from a previous experiment is negligible in wave focusing. Wave generation in the MWL flume takes approximately 60 seconds. During this time, vorticity is being generated at the side walls and the bottom due to viscosity, and convected through the flow. Once wave generation finishes, the vorticity introduced by the walls, the breaking wave and the wave impact diffuses as there is no longer an energy source for convection. Therefore, as vorticity is convected for about a minute, compared to hours in the previous publication, it has been assumed that any particle motion introduced in the flow from a previous experiment rapidly decays due to diffusion and its magnitude is negligible compared to the seiche-induced current.

Chapter 5

Code implementation

The previous chapter has proposed a theoretical method to compute and evaluate the variability introduced by the sources of variability at different positions along the flume. The method relies on the wave focusing technique used—the phase speed method—to alter the propagation velocity of the different wave components as the water depth varies or a current develops. The differences in the wave celerity results in the phase shift of some wave components which leads to differences in the focal point/time and in the amplitude of the wavelet.

This chapter is dedicated to describe the implementation of the expressions presented in the previous chapters into the programming language Python by means of open-source libraries. It has been considered a modular approach in its development, such that if, for instance, another spectrum formulation is of interest, the user only has to define a new function in the script and call it instead of the Ricker formulation.

5.1 Generation of control signals

The control signal is obtained by solving eq. (3.11). The amplitude spectrum and the wavenumbers corresponding to each frequency are required before it can be computed. These are readily determined taking advantage of basic array manipulations of Numpy arrays in Python. Numpy is a package used for scientific computing with Python and, besides its scientific uses, it can also be used as an efficient multidimensional container of generic data (van der Walt, 2011). The basic array manipulations used in the following sections are:

- Attributes of arrays: determining the size, shape, memory consumption and data type of the array.
- Indexing of arrays: getting and setting the value of individual array elements.
- Slicing of arrays: getting and setting smaller subarrays withing a larger array.
- Reshaping of arrays: changing the shape of a given array.
- Joining and splitting of arrays: combining multiple arrays into one, and splitting one array into many.

The amplitude spectrum

First of all, the spectrum properties must be defined to compute the Ricker spectrum expressed by eq. (2.35), i.e., the wave crest height, H_c, the peak period, ω_p, the parameters controlling the spectrum shape, β_l and β_h; and the number of wave components into which the spectrum is discretized, n. Then, an evenly spaced 1D-array containing the frequencies in the interval of interest is defined. During the thesis, the (arbitrarily) chosen interval has been $[0,\ 8\omega_\mathrm{p}]\,\mathrm{rad/s}$. The higher frequency of the interval (upper bound) has to be large enough such that its amplitude can be neglected. Note that zero amplitude in the Ricker spectrum is an asymptotic limit only reached at $\omega = +\infty\ \mathrm{rad/s}$—although it rapidly decreases from the peak frequency—which means that

all wave components participate in obtaining the characteristic wavelet and cannot be drastically removed.

The piecewise expression of the amplitude spectrum is implemented using the slicing attribute of Numpy arrays and the possibility to be used with boolean arrays. An initial zero 1D-array is defined which will store the amplitudes of each wave component. The piecewise condition is expressed by means of a boolean mask array which takes a TRUE value at the positions where the frequency is smaller or equal than the peak frequency and a FALSE value when otherwise. Once the amplitude spectrum is computed, each amplitude is summed-up yielding the wave crest height of the wavelet. As this value differs from the predefined wave crest height—the original Ricker formulation is derived from the normalized Ricker wavelet and the implementation of β_l and β_h change the total energy of the spectrum—a correction value is computed ($H_\mathrm{c}/H_\mathrm{c,Ricker}$) and multiplied by the spectrum. The pseudocode of the required steps to obtain the amplitude spectrum is shown below:

```
Given H_c, ω_p, β_l, β_h and n
Set ω_list = linspace from 0 to 8ω_p, num=n
Initialize a_list = zeros(n)
Set mask = ω_list ≤ ω_p     # boolean array:  [1, 1, ···, 1, 0, 0, ···, 0]
Set a_list where mask==1 to a_R(ω ≤ ω_p)
Set a_list where mask==0 to a_R(ω > ω_p)
Set H_c,Ricker = sum(a_list)
Set correction = H_c/H_c,Ricker
Update a_list = correction · a_list     # results in a wavelet with crest height H_c
```

The wavenumbers

Approximately 100.000 wave components are used to derive a control signal. Computing the wavenumbers requires the use of a numerical solver because the dispersion relation is an implicit equation, resulting in the most expensive task in the algorithm. Bisection method was used due to its simplicity and because it resulted in faster convergence of the solution compared to built-in solvers. Nevertheless, the computational times were still too high to compute the variability introduced by seiching when written in pure Python. In consequence, the task was written in TensorFlow, an open-source library for Python used for machine learning. The library builds a dataflow graph with the operations to be done highly optimizing its parallelization. In addition, it was used to perform the computation in the GPU (CUDA cores) instead of in the CPU. As an example of the differences in computational power, the latest GPU's have over 3000 CUDA cores compared to 4-8 cores in an average CPU.

The control signal

The wavemaker control signal was computed in Python rewriting eq. (3.11) into a matrix equation that makes use of broadcasting—a property of Numpy arrays to perform arithmetic operations on arrays with different shapes. It resembles the mathematic operation known as dyadic product, outer product or tensor product:

$$\boldsymbol{ab} \equiv \boldsymbol{a} \otimes \boldsymbol{b} \equiv \boldsymbol{ab}^\top = \begin{pmatrix} a_1 \\ a_2 \\ a_3 \end{pmatrix} \begin{pmatrix} b_1 & b_2 & b_3 \end{pmatrix} = \begin{pmatrix} a_1b_1 & a_1b_2 & a_1b_3 \\ a_2b_1 & a_2b_2 & a_2b_3 \\ a_3b_1 & a_3b_2 & a_3b_3 \end{pmatrix}$$

with the advantage that Numpy broadcasting extends it to any arithmetic operation. As a result, the expression used in Python to compute the wavemaker control signal is:

$$\boldsymbol{X} = \left[\boldsymbol{a} \oslash \boldsymbol{\zeta}\right] \cdot \left[\exp\left(i(-\boldsymbol{k}^\top x_\mathrm{f} - \boldsymbol{\omega}^\top \boldsymbol{t})\right)\right] \tag{5.1}$$

with:

$$\boldsymbol{\zeta} = \Big[4i\sinh^2(\boldsymbol{k}h)\Big] \oslash \Big[\sinh(2\boldsymbol{k}h) + 2\boldsymbol{k}h\Big] \tag{5.2}$$

where all vectors are row vectors $1 \times n$ with exception of $\boldsymbol{t}$, which is a row vector whose length is given by the duration of the control signal and its resolution. The symbol $\cdot$ is the scalar product and $\oslash$ represent the Hadamard division, or the element-wise matrix division.

The result of eq. (5.1) is a 1D-array with the same shape as $\boldsymbol{t}$ where the element X_i is the paddle excursion at time t_i.

As discussed in chapter 3, the last part of the wavemaker control signal shifts to a constant non-zero value when $\beta_1 \neq 0$. Nevertheless, the wavemaker control system requires that the signal starts and ends with zero values for a duration of at least two seconds. At the beginning of the signal, this is obtained attaching a zero 1D-array whose length is equal to $2F_\mathrm{s}$, where F_s is the sampling frequency of the control signal. At the end of the control signal, a sinusoidal shape must be first attached to it slowly bringing the paddle back to its zero position. In Python, this is achieved concatenating the vector:

$$\boldsymbol{X}_\mathrm{end} = X_n\left(\frac{1}{2} + \frac{1}{2}\cos\left(\frac{\pi}{D_\mathrm{end}}\boldsymbol{t}_\mathrm{end}\right)\right) \tag{5.3}$$

to the end of the vector $\boldsymbol{X}$. Where X_n is the last element of $\boldsymbol{X}$, D_end is the duration of the control signal to bring the paddle back to the zero position and $\boldsymbol{t}_\mathrm{end}$ is a row vector from 0 to D_end with the same time resolution as the control signal.

As also mentioned in chapter 3, due to asymmetry of the control signal—the paddle excursion forward is larger than backwards—it may happen that the control signal is rejected by the wavemaker control system due to the motion being out of limits—it usually occurs when the wave characteristics are too large, for instance the wave crest height or its period; or when the spectrum is too narrow, which means the wave energy must be concentrated over a small number of wave components. To tackle this issue and extend the range of waves that can be generated, the possibility to shift the control signal was included. As the shift results in a change of the zero position of the wavemaker, the focal point has to be adjusted to account for the later shift of the control signal. For example, if the focal point is expected at $10\mathrm{cm}$ from the impact wall, a shift of $5\mathrm{cm}$ backwards in the control signal will result in the focal point at $15\mathrm{cm}$ from the impact wall. Thus, the focal point is modified given the shift that is desired in the control signal by:

$$x_\mathrm{f} = x_{\mathrm{f},0} + \Delta\boldsymbol{X} \tag{5.4}$$

where $x_{\mathrm{f},0}$ is the focal point considering the frame of reference depicted in Figure 2.1 and $\Delta\boldsymbol{X}$ is the shift in the zero position of the wavemaker, being positive forward. Then, a sinusoidal signal is attached to the beginning of the control signal, slowly moving the paddle from the mechanical zero position to the shifted zero position. In Python it is achieved concatenating the vector:

$$\boldsymbol{X}_\mathrm{beg} = \Delta\boldsymbol{X}\left(\frac{1}{2} - \frac{1}{2}\cos\left(\frac{\pi}{D_\mathrm{beg}}\boldsymbol{t}_\mathrm{beg}\right)\right) \tag{5.5}$$

in front of the vector $\boldsymbol{X}$. Where D_beg and $\boldsymbol{t}_\mathrm{beg}$ are, respectively, the duration of control signal to bring the wavemaker to the shifted zero and a row vector from 0 to D_beg, with the same time resolution as the control signal.

The previous series of steps result in a control signal as depicted in Figure 3.3. The pseudocode to obtain the control signal is shown below:

```
Given x_{f,0}, ΔX, ω, a, k, ζ, t, t_beg, t_end, D_beg and D_end
Set x_f = x_{f,0} + ΔX
Compute X      # Eq. (5.1)
Compute X_beg      # Eq. (5.5)
Compute X_end      # Eq. (5.3)
Update X = concatenate(X_beg, X, X_end)
Update X = 0-padding(X, len=2F_s, side=both_ends)
```

5.2 Sources of variability

The sources of variability were evaluated in the previous chapter propagating the wave train generated by the control signal, at different water depths and current conditions, to the focal point; obtaining wavelets that slightly differed from the Ricker wavelet. This section explains how the expressions presented in chapter 4 were implemented in the wave propagation algorithm as a module that can be activated when the variability effects are to be evaluated.

Water depth variability

The wavelet at the focal point considering errors in the water depth measurements are obtained with eq. (4.9). Note that the control signal (in time domain) is not explicitly included in this expression. The reason is that, if the control signal were the input of the algorithm to get the wavelets, a Fourier analysis would be required to get the amplitude spectrum of the signal, leading to errors when compared to the Ricker spectrum due to the finite length and discrete resolution of the input signal. Instead, the Ricker amplitude spectrum was divided by the transfer function from paddle excursion to wave elevation at the design water depth but, instead of adding up the result which would lead to a time domain signal, the result is multiplied again by the transfer function, this time considering a different water depth. These operations model the (linear) variability introduced in the amplitude spectrum by the wavemaker, due to the fact that the control signal was derived at the design water depth but wave generation occurred at a different water depth. Then, knowing the phase of each wave component at the wavemaker, $x = -x_\mathrm{f}$, at $t = 0$ and $h = 400\mathrm{mm}$; the components are propagated to the focal point at a different water depth, which affects the dispersion relation and results in a phase shift. Adding up all wave components over time results in the wavelets considering errors in the measurement of the water depth.

The mathematical derivation of the expression is shown below.

- The free surface elevation of a linear wave is determined by:

$$\eta(x,t) = a\exp\left[i\left(kx - \omega t + \phi\right)\right] \tag{5.6}$$

- The paddle excursion to produce the wave elevation at the wavemaker, $x = -x_\mathrm{f}$, given the initial phase, $\phi = 0$, is determined by:

$$X(-x_\mathrm{f},t) = a\exp\left[i\left(-k_{400}x_\mathrm{f} - \omega t\right)\right]\frac{1}{\zeta(400)} \tag{5.7}$$

  where k_{400} is the wavenumber at the design water depth, $h = 400\mathrm{mm}$; and $\zeta(400)$ is the transfer function from flap excursion to wave elevation at the design water depth, eq. (3.10).

- To obtain the free surface elevation at the wavemaker position considering water depth variability, the previous expression is multiplied by the transfer function at the new water depth:

$$\eta_\mathrm{wm}(h,t) = a\exp\left[i\left(-k_{400}x_\mathrm{f} - \omega t\right)\right]\frac{\zeta(h)}{\zeta(400)} \tag{5.8}$$

- Propagating the wave back to the focal point at a different water depth results in a phase shift, $\phi \neq 0$:

$$\phi = -k_{400}x_\mathrm{f} + k_\mathrm{h}x_\mathrm{f} \tag{5.9}$$

where h_{h} is the wavenumber at the different water depth. When the water depth is the same both wavenumbers cancel out and the phase shift is zero. On the other hand, when the water depth increases, the wavenumber reduces (longer wavelength) and the phase shift becomes negative, i.e., the wave crest has already passed the focal point (the wave arrives earlier); the opposite applies when the phase is positive.

- Result of the differences in phase, the wave elevation at the focal point, $x = 0$, becomes:

$$\eta_0(h,t) = a \exp\left[i\Big((k_{\mathrm{h}} - k_{400})x_{\mathrm{f}} - \omega t\Big)\right] \frac{\zeta(h)}{\zeta(400)} \tag{5.10}$$

- When multiple waves are found in the flume, the free surface elevation is the sum of all wave components, resulting in eq. (4.9):

$$\eta_{\mathrm{wlet}}(h,t) = \sum_{i=1}^{n} a_i \exp\left[i\Big((k_{i,h} - k_{i,400})x_{\mathrm{f}} - \omega_i t\Big)\right] \frac{\zeta(h)}{\zeta(400)} \tag{5.11}$$

Taking advantage of the Numpy array attributes presented in the previous section, the implementation of the equation is straightforward. The expression can be rewritten in a matrix form:

$$\boldsymbol{\eta}_{\mathrm{wlet}}(h) = \left[\boldsymbol{a} \circ \boldsymbol{\zeta}_{\mathrm{h}} \oslash \boldsymbol{\zeta}_{400}\right] \cdot \left[\exp\left(i\left(\left(\boldsymbol{k}_{\mathrm{h}}^{\top} - \boldsymbol{k}_{400}^{\top}\right) x_{\mathrm{f}} - \boldsymbol{\omega}^{\top}\boldsymbol{t}\right)\right)\right] \tag{5.12}$$

where all vectors are row vectors $1 \times n$ with exception of $\boldsymbol{t}$, which is a row vector defining the time domain of the wavelet. The symbol $\cdot$ is the scalar product and $\circ$ and $\oslash$ represent, respectively, the Hadamard product and division, or the element-wise matrix product and division.

Seiching variability

Seiching was covered in section 4.4. The variability introduced in the wavelet was computed considering a residual standing wave in the flume—the fundamental seiching mode—which introduces a space-time-dependent current and a space-time-dependent water depth which oscillates around the mean water depth. Consequence of the space-time dependency, a numerical approach was required to obtain the wavelets at the focal point. The expression that has been computed numerically is eq. (4.23). Like in the previous section, the basis is to compute the variability introduced in the Ricker spectrum by the wavemaker, due to the fact that wave generation occurred at a water depth different than the design water depth. This operation is time dependent. Therefore, the amplitude spectrum needs to be updated at every time step. Then, the phase shift at the focal point and focal time resulting from the different water depths is determined. The step requires the discretization of the space and time domains to compute the wavenumbers at every position and time in the flume—function of the local water depth and current. Lastly, the wavelet is computed.

Mathematically, eq. (4.23) is derived as follows:

- The (general) free surface elevation of a linear wave is:

$$\eta(x,t) = a \exp\left[i\left(\int_0^x k(x,t)\,\mathrm{d}x - \omega t + \phi\right)\right] \tag{5.13}$$

when the wavenumber is independent of the position, $k = k(t)$ (or $k = \mathrm{const}$), and the lower limit is zero, $x_0 = 0$, eq. (5.6) is obtained.

- The amplitude of the wave resulting from wave generation at a different water depth than the one used for the derivation of the control signal is:

$$a(t) = a_0 \frac{\zeta(h_{\mathrm{wm}}(t))}{\zeta(400)} \tag{5.14}$$

where a_0 is the desired wave amplitude, $\zeta(400)$ is the wavemaker transfer function at the design water depth and $\zeta(h_{\mathrm{wm}}(t))$ is the time-dependent transfer function of the wavemaker at the instant water depth at the wavemaker position.

- At the focal point, eq. (5.13) becomes:

$$\eta(0,t) = a_0 \exp\left[i\left(\int_{-x_\mathrm{f}}^{0} k(x,t)\,\mathrm{d}x - \omega t + \phi_\mathrm{wm}\right)\right]\frac{\zeta(h_\mathrm{wm}(t))}{\zeta(400)} \tag{5.15}$$

  where ϕ_wm is the phase of the wave at the wavemaker position at $t = 0$ due to the bounds of the integral, given by:

$$\phi_\mathrm{wm} = -k_{400}x_\mathrm{f} \tag{5.16}$$

- Combined, when multiple waves are found in the flume, eq. (4.23) is obtained:

$$\eta_\mathrm{wlet}(t) = \sum_{i=1}^{n} a_i \exp\left[i\left(\int_{-x_\mathrm{f}}^{0} k_i(x,t)\,\mathrm{d}x - \omega_i t - k_{400}x_\mathrm{f}\right)\right]\frac{\zeta(h_\mathrm{wm}(t))}{\zeta(400)} \tag{5.17}$$

The expression was implemented in the algorithm in the matrix form:

$$\boldsymbol{\eta}_\mathrm{wlet} = \left[\boldsymbol{a} \circ \boldsymbol{\zeta}_\mathrm{hwm} \oslash \boldsymbol{\zeta}_{400}\right] \cdot \left[\exp\left(i\left(\boldsymbol{K}^\top - \boldsymbol{\omega}^\top \boldsymbol{t} + \boldsymbol{\phi}_\mathrm{wm}\right)\right)\right] \tag{5.18}$$

where $\boldsymbol{K}$ is the result of integrating the wavenumbers from $x = -x_\mathrm{f}$ to $x = 0$. $\boldsymbol{a}$, $\boldsymbol{\zeta}_{400}$, $\boldsymbol{\omega}$, $\boldsymbol{t}$, and $\boldsymbol{\phi}_\mathrm{wm}$ are row vectors $1 \times n$, with n the number of wave components. $\boldsymbol{\zeta}_\mathrm{hwm}$ and $\boldsymbol{K}$ are matrices $m \times n$, with m the length of the discretized time domain and n the number of wave components.

As can be seen, the dimensions to perform the operations do not match. For instance, the Hadamard product $\boldsymbol{a} \circ \boldsymbol{\zeta}_\mathrm{hwm}$ is a $[1 \times n] \circ [m \times n]$ operation, while it would require $\boldsymbol{a}$ to be a $m \times n$ matrix. As introduced in the beginning of the chapter, Numpy arrays have the property of broadcasting, which automatically complete the missing dimensions in an array. In the example:

$$\boldsymbol{a} \circ \boldsymbol{\zeta}_\mathrm{hwm} = \begin{bmatrix} a_1 & \cdots & a_\mathrm{n} \end{bmatrix} \circ \begin{bmatrix} \zeta_{1,1} & \cdots & \zeta_{1,\mathrm{n}} \\ \vdots & \ddots & \vdots \\ \zeta_{\mathrm{m},1} & \cdots & \zeta_{\mathrm{m},\mathrm{n}} \end{bmatrix} = \begin{bmatrix} a_1\zeta_{1,1} & \cdots & a_\mathrm{n}\zeta_{1,\mathrm{n}} \\ \vdots & \ddots & \vdots \\ a_1\zeta_{\mathrm{m},1} & \cdots & a_\mathrm{n}\zeta_{\mathrm{m},\mathrm{n}} \end{bmatrix} \tag{5.19}$$

Eq. (5.18) is, however, the last step when computing the wavelet resulting from having the fundamental seiching mode in the flume. The amplitudes must be computed for each time step, as well as the transfer functions and the integration of the wavenumbers along the flume. The pseudocode to compute the required values is shown below:

```
Given x_f, ω, a, ζ_400, x, t and ω_seich
Set k_seich = solve(disp_relation, ω=ω_seich, current=0)    # Eq. (4.25)
Set k_400 = solve(disp_relation, ω=ω, current=0)    # Eq. (4.25)
Set φ_wm = −k_400 x_f
Initialize ζ_hwm = K = zeros(m × n)
for t_i in t:
  Set η_seich = a_seich cos(k_seich x) cos(ω_seich t_i)    # x is the discretized space vector
  Set h = h_400 + η_seich
  Compute u_x(x, t_i)    # Seiche current at each position, eq. (4.20)
  Set k = solve(disp_relation, ω=ω, current=u_x(x, t_i))    # Eq. (4.25)
  Set K[i, :] = integrate(k, vector=x, method=Simpson)
  Compute ζ_hwm[i, :]    # Eq. (3.10)

Compute η_wlet    # Eq. (5.18)
```

Water depth and seiching combined variability

The previous set of expressions can be used to compute the combined variability from water depth and seiching. The only requirement is to change the water depth when computing the seiche-induced current and the wavenumbers at the discretized positions. The pseudocode is very similar to the one shown above:

```
Given x_f, ω, a, ζ_400, x, t and ω_seich
Set k_seich = solve(disp_relation, ω=ω_seich, current=0)    # Eq. (4.25)
Set k_400 = solve(disp_relation, ω=ω, current=0)    # Eq. (4.25)
Set φ_wm = −k_400 x_f
Initialize ζ_hwm = K = zeros(m × n)
for t_i in t:
   Set η_seich = a_seich cos(k_seich x) cos(ω_seich t_i)    # x is the discretized space vector
→  Set h = h_var + η_seich    # h_var ∈ 400 ± 5mm
   Compute u_x(x, t_i)    # Seiche current at each position, eq. (4.20)
   Set k = solve(disp_relation, ω=ω, current=u_x(x, t_i))    # Eq. (4.25)
   Set K[i, :] = integrate(k, vector=x, method=Simpson)
   Compute ζ_hwm[i, :]    # Eq. (3.10)

Compute η_wlet    # Eq. (5.18)
```

5.3 Verification and validation

The aim of this section is to verify the numerical model used for the evaluation of the sources of variability, which in the end is used for the derivation of the repeatability criteria; and to validate the model with measurements of the free surface elevations obtained in the experimental flume. What is to be understood by verification and validation in this context has been well expressed in Roache (1998): verification is a purely mathematical exercise that intends to show that "the equations are being solved right", whereas validation is a science/engineering activity that intends to show that "the right equations are being solved".

Code verification

Verification is used in numerical computations to establish the credibility of the numerical results. Eça and Hoekstra (2014) split the verification process in two different activities: code verification and solution verification. The former intends to verify, by error evaluation, that a given code solves correctly the equations that the model contains. The latter intends to estimate the error/uncertainty of a given calculation for which, in general, the exact solution is not known.

This section treats code verification of the wave propagation model used for the evaluation of seiching variability and the combined effects of seiching and water depth. The equations used for the derivation of the control signal and the evaluation of the water depth variability are analytic expressions and, therefore, the magnitude of the expected errors in these calculations is the machine truncation error.

A test case for which the solution is known has been used to verify the numerical model. In the absence of a seiche in the flume and a still water depth equal to the design water depth, the resulting wavelet from the numerical model must be the same as the wavelet obtained from the Ricker spectrum:

$$\eta_{\text{wlet}} = \sum_{i=1}^{n} a_{\text{R}}(\omega_i) \exp\left(-i\omega_i t\right) \tag{5.20}$$

This expression is considered to be simple enough to not require verification.

Next step is to use eq. (5.18) with the same initial amplitude spectrum to derive the numerical wavelet considering $\boldsymbol{\eta}_{\text{seich}} = 0$ and $h = 400\text{mm}$. This verifies that the space discretization is

enough to capture the wave shape of all wave components, ensuring the accurate integration of the wavenumbers. Figure 5.1 shows the comparison of the resulting wavelets as presented in the same kind of graph as in the previous chapter. As can be seen, the error of the numerical wavelet compared to the analytical one is zero—computing the amplitude error of the individual frequencies also shows an exact zero value, meaning that if there is an error it is smaller than a 64-bit float number—which verifies the numerical model for wave propagation in the absence of a seiche.

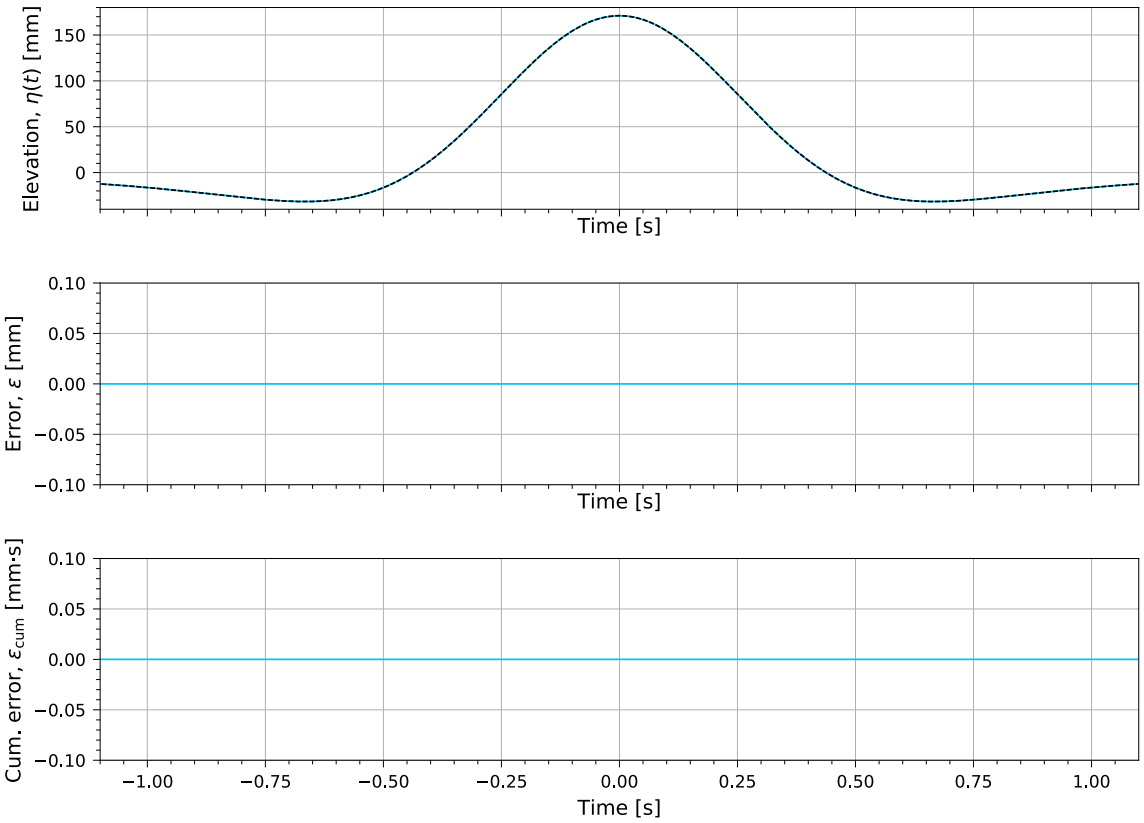

Figure 5.1: Comparison of the analytical wavelet (- - -) obtained with eq. (5.20), and numerical wavelet (——) obtained with eq. (5.18) in the absence of a seiche. The spectrum characteristics are: $T_\mathrm{p} = 2.2\mathrm{s}$, $H_\mathrm{c} = 170\mathrm{mm}$, $\beta_\mathrm{l} = 0.5$ and $\beta_\mathrm{h} = 0.45$.

To verify the numerical model in the presence of a seiche, the computed velocity field of the standing wave will be compared to the maximum seiche-induced current estimated by eq. (4.14). It is assumed that if the seiche current and elevation is computed right, the previous verification of the propagation model ensures that the resulting wavelet is correct. Thus, considering a fundamental seiching mode of amplitude $a_\mathrm{s} = 1\mathrm{mm}$, three conditions must be satisfied: (1) when the seiche is with the maximum amplitude at one end of the flume, the velocities in the flow must be zero. (2) when the elevation of the seiche is zero along the entire flume, the velocities at the node are maximum and, according to eq. (4.14), its magnitude is approximately $V_\mathrm{max} \approx 5.0\mathrm{mm/s}$; and (3) the boundary conditions must be satisfied, i.e., the velocities at the side walls must be zero at all times. Figure 5.2 clearly shows that the three conditions are satisfied and, therefore, the current and the seiche elevations are also correctly computed.

Code validation

The wave propagation algorithm presented in the previous section was used to compute the control signals, the (theoretical) variability at the focal point and also to derive the experimental repeatability criterion at the positions where the cameras are located ($x = [-4.8, -2.3]\mathrm{m}$). The verification step showed that the equations of the model are being solved right. Nevertheless, the

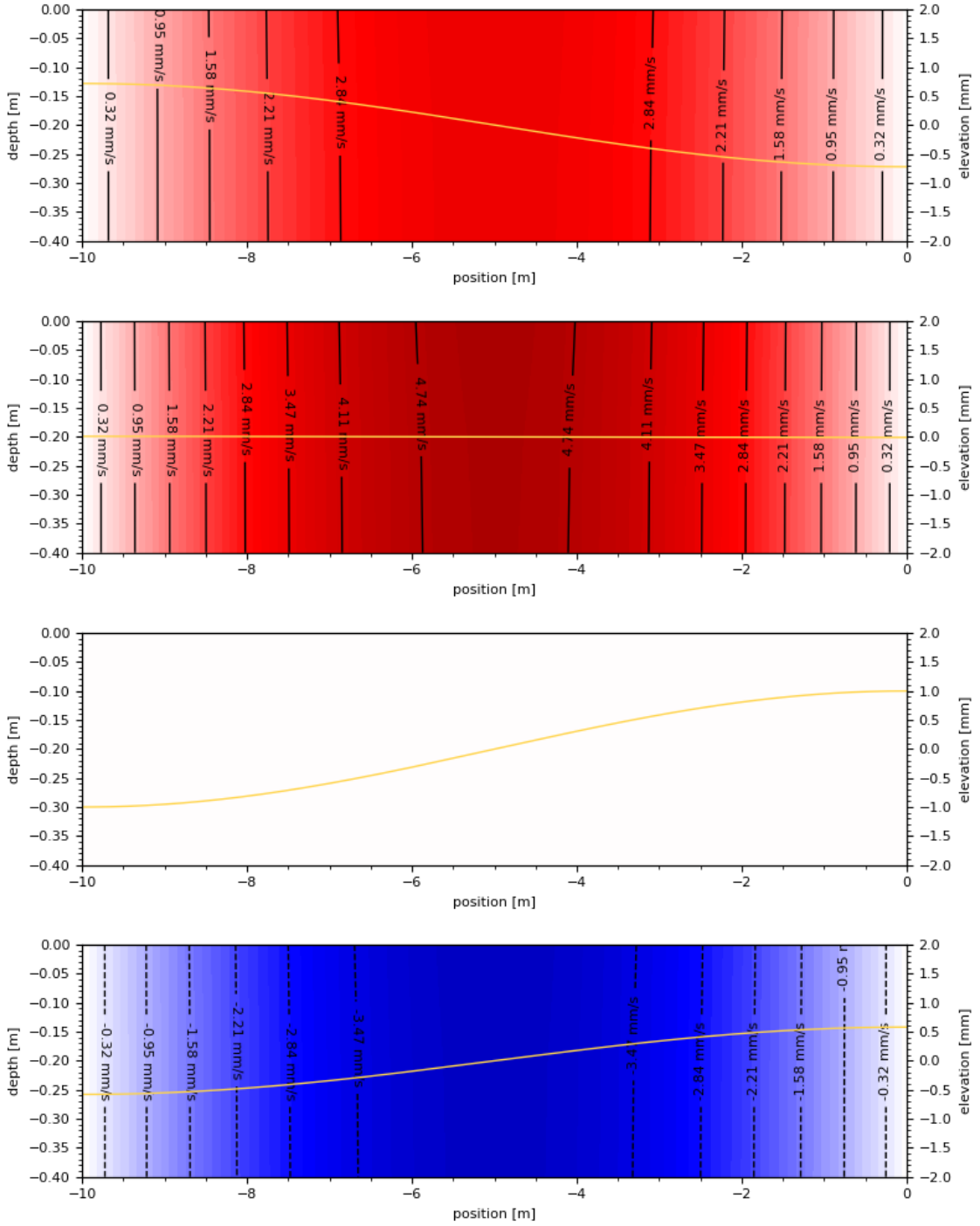

Figure 5.2: Horizontal velocity field of the fundamental seiching mode and corresponding elevation of the seiche at four instants. Contours show the magnitude of the horizontal velocities. In red positive in the direction of propagation and, in blue, opposing to the wave propagation. The seiche elevation is shown with an orange line.

model is used to link theory and experiments and, therefore, must be also validated.

The goal of validation is to quantify the modelling uncertainty, i.e., how well the model represents the physical world. The first task in any validation process is to determine the quantities of interest. The model may be adequate to accurately determine some quantities and give poor estimations on others. Once the decision has been made, a second challenge appears: determining the most appropriate validation metric. This is still a research topic and there are several proposals available in the literature (Eça and Hoekstra, 2013).

Models that are subjected to validation are mathematical expressions that try to represent the physical world with high fidelity. The series of expression used in this thesis are, however, simple expressions derived from linear theory that were never intended to give an accurate estimate of a flow quantity. Therefore, a quantitative validation of the model does not make any sense, since the assumptions made in its derivation are off from reality. For instance, linear wave theory fails in estimating the wave shape. Real waves have a flatter trough and sharper crest and, therefore, a higher order theory should have been used if an accurate estimation of the wave elevations were required for the application. Thus, the validation of the model will be qualitative, comparing the free surface elevations obtained experimentally and numerically at the camera positions.

While linear theory fails in predicting the wave shape and linear wavemaking theory does not account for higher order effects, such as the generation of superharmonic waves that arise from wave interactions, the propagation velocity is expected to be accurate—at least in those components where the relative importance of non-linearities is small, i.e., the shorter waves. A comparison between the free surface elevations obtained numerically and a measurement obtained experimentally is shown in Figure 5.3. It is clear the large differences obtained in the amplitudes of the higher frequencies. The wave elevations are larger experimentally than numerically which can only be explained by a shift of the spectrum towards higher frequencies due to wave generation, meaning that linear wavemaking theory does not accurately generate the desired spectrum or that the spectrum shape is not realistic. To check that this is the case, the numerical and experimental amplitude spectra were computed, see Figure 5.4. The figure confirms a shift of the spectrum, with the experimental peak frequency being almost three times higher than the theoretical one. Regarding the wave propagation velocity, it can be seen that the phases of the waves are aligned, with the exception of last wave of the train. As the energy of the lower frequencies is higher in the theoretical spectrum, the apparent frequency of the last wave is lower, resulting in a wave that is being generated later in time and, therefore, reaches the camera positions also later.

Considering the theoretical model valid or not is a difficult task. Looking at the wave elevations, it is obvious that the model does not accurately predict the wave elevations. Nevertheless, as stated at the beginning of the section, in model validation one should first determine the quantities of interest. The ”quantity” used in the theoretical work to derive the experimental repeatability criterion was the Fourier-space of the elevations. As depicted in Figure 5.4, the amplitude spectrum of the elevations shifts experimentally and, therefore, should be considered not valid. However, assuming there is a transformation vector, $\boldsymbol{T}$, such that:

$$a_{\mathrm{exp}}(\omega) = a_{\mathrm{lin}}(\omega)\boldsymbol{T} \tag{5.21}$$

The theoretical work and the repeatability criterion would still be valid as, according to Perlin and Bustamante (2016): *The similarity parameter Q has been normalized so that its value does not change if the signals get re-scaled by a common factor*.

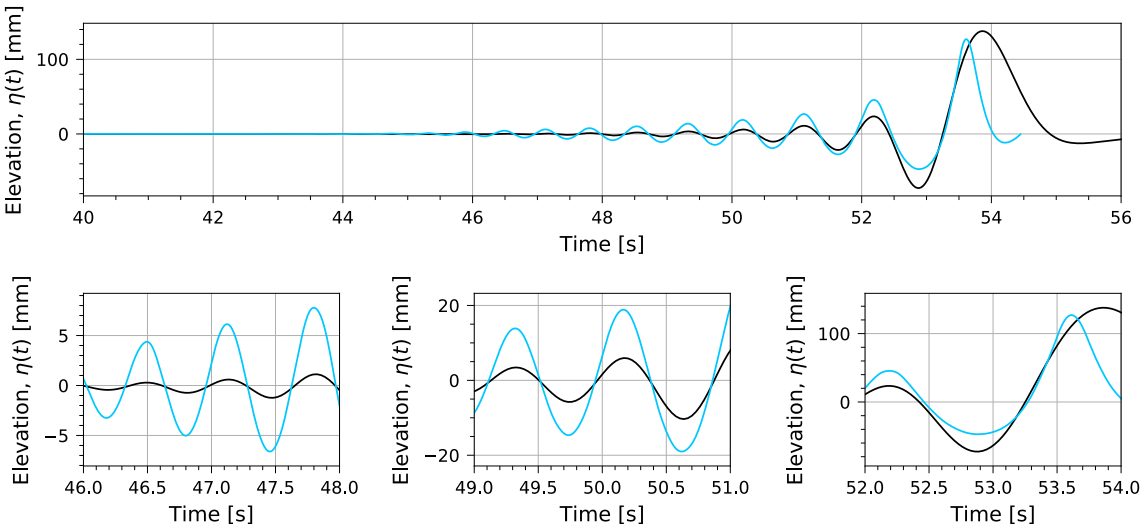

(a) Free surface elevations at $x = -4.8\mathrm{m}$.

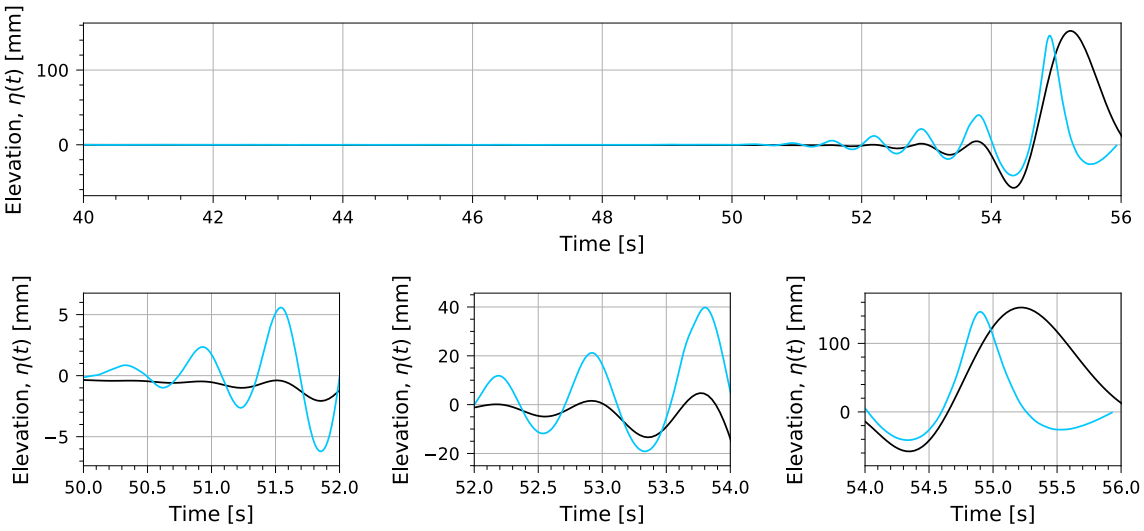

(b) Free surface elevations at $x = -2.3\mathrm{m}$.

Figure 5.3: Comparison of the free surface elevations obtained numerically (——) and experimentally (——) at camera positions.

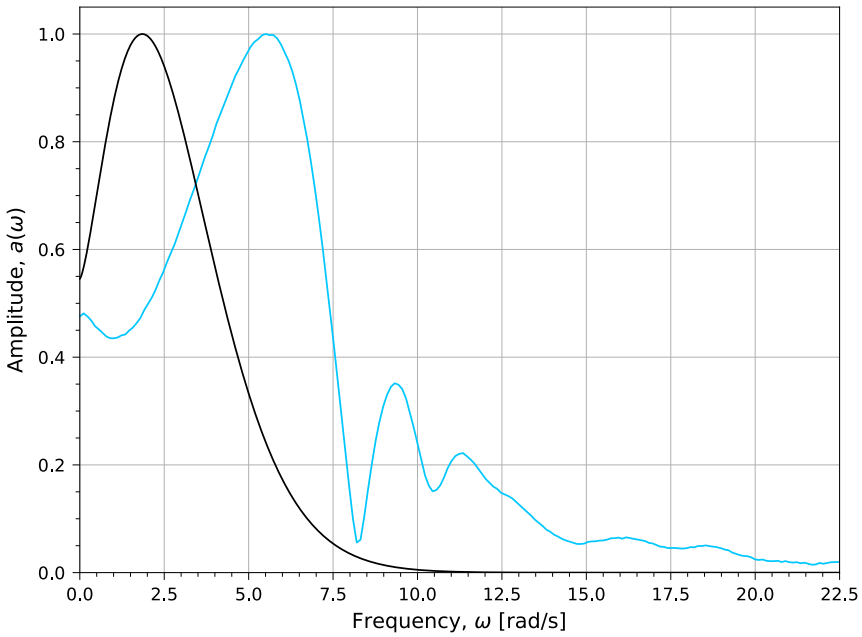

Figure 5.4: Comparison of the normalized theoretical amplitude spectrum (——) and the amplitude spectrum of the measurements (——).

Chapter 6

Experimental results and analysis

Multiple wave impact tests were performed during this study to evaluate the repeatability of the global flow of breaking waves in the Multiphase Wave Lab (MWL) at MARIN. The MWL is an unique facility built from the results of the Sloshel Joint Industry Project (Bogaert, 2018). Bogaert concluded that, to experimentally study the multiphase dynamics on sloshing impact loads, the governing parameters of each multiphase dynamic must be varied one at a time. After investigating different technical solutions to perform wave impact tests in an environment that allowed such systematic investigation, the decision was to install a wave flume inside a high-end autoclave. A graphical representation of the design is presented in Figure 6.1.

Initial experiments in the facility were carried out to determine the parameters of the spectrum that define specific wave characteristics, gaining insight in how they control certain aspects of the wave (thickness and stability of the wave crest, impact type, gas pocket size and wave crest height). Once the waves of interest were established with assistance from Olivier Kimmoun, several number of experiments were run at different temperature and pressure conditions (only the results obtained from different pressure conditions will be shown in this thesis). Image processing techniques were then required to obtain measurements of the wavemaker motion and the wave elevations at two positions along the flume. These measurements were compared to the repeatability criteria derived in the previous chapters to evaluate the global flow repeatability.

In this chapter, a brief introduction to the MWL and the experimental setup is given first, section 6.1. Next, the waves used during the experiments and observations about how the spectrum affects the wave shape are presented, section 6.2. It follows a description of the image processing algorithms used to obtain measurements from the recordings, section 6.3; and, lastly, the results from the experiments are presented and evaluated, section 6.4.

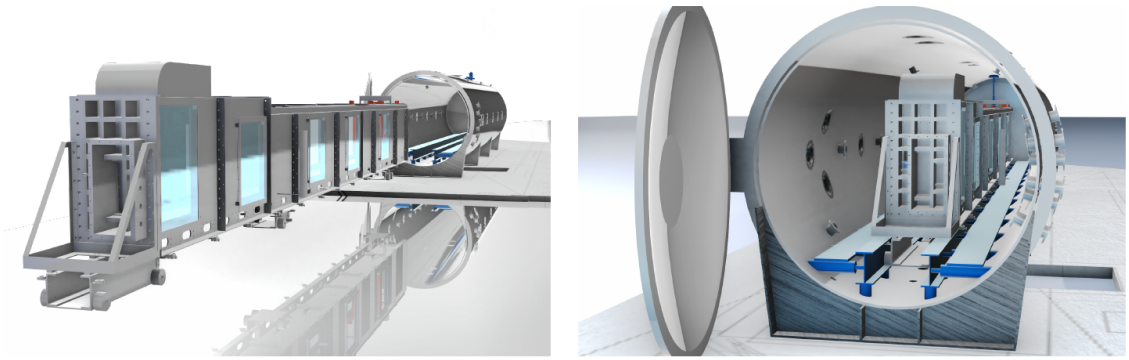

Figure 6.1: Basic design of the MWL flume and the $15\mathrm{m}$ long autoclave (Bogaert, 2018).

6.1 Experimental set-up

The MWL consists of a $15\mathrm{m}$ long $\times$ $2.5\mathrm{m}$ diameter autoclave with observation windows, gas and liquid supply systems and a heating and cooling system for the autoclave environment and the water in the flume tank. These systems allow a range of temperature from $5\,℃$ to $180\,℃$ and an absolute pressure from $5\mathrm{mbar}$ to $10\mathrm{bar}$. The gas inside the autoclave can be a mixture of air, water vapor, He, N_2 and SF_6.

Flume tank

The flume is a $12.5\mathrm{m} \times 0.6\mathrm{m} \times 1.2\mathrm{m}$ tank made of steel with five glass panels on one side for observation and five light diffuser panels on the other. The glass panels are marked in the middle with two columns of laser printed reference dots spaced vertically every $50\mathrm{mm}$ and $100\mathrm{mm}$ horizontally. Demineralized water is used in the flume to avoid corrosion that could damage the different subsystems or that could lead to the presence of particles in the water. Due to the harsh environmental conditions inside the autoclave—and the use of demineralized water—resistive measurement devices cannot be used. In addition, vacuum conditions make impossible the use of sound based devices. In consequence, a mechanical water depth sensor is placed in a pipe parallel to the flume not disturbing the flow field. The resolution of the sensor is $0.1\mathrm{mm}$. Water depth is continuously monitored and automatically controlled when need be through the Overall Control System (OCS) of the facility.

Wavemaker

A position-controlled piston type wavemaker is located at one end of the flume. Its zero position is defined such that the distance from its front surface to the impact wall is $10\mathrm{m}$. The wavemaker can be automatically controlled through the OCS via recipes—predefined functions that send a series of commands—or manually through the proprietary software developed by the company in charge of its design. A very useful feature of the software is the automatic generation of motion correction files. Usually, when a control signal is sent to the wavemaker control system, it results in an 'erratic' motion either due to wave reflections, friction or environmental conditions. Some wave components are slightly out of phase and/or their amplitudes are not as prescribed. The tool compares the measured position of the paddle with the control signal and automatically computes a correction signal in the frequency domain. Once the correction is applied, the paddle motion closely follows the position of the control signal. The design acceptance values of the wavemaker motion error had been presented in Table 4.2.

The wavemaker is driven by a $10\mathrm{A}$ electric motor located outside the autoclave on top of the wavemaker. An encoder in the electric motor gives the position of the paddle with a resolution of approximately $0.06\mathrm{mm}$. A tracking pattern has also been stuck to the side surface of the paddle, allowing for camera measurements of its position. Behind the wavemaker, a stainless steel beach is found, reducing sloshing impacts in the back surface of the paddle due to reflections.

Camera systems

Two high speed cameras are placed outside the autoclave focused at the impact wall. One of them captures the breaking wave in a plane parallel to the direction of wave propagation and perpendicular to the impact wall. The second camera is positioned at an angle such that the transversal development of instabilities or other phenomena is captured. The cameras shoot at $1\mathrm{kHz}$ to $5\mathrm{kHz}$ depending on the uncertainties in the focal time—$5\mathrm{kHz}$ recordings require accurate predictions of the focal time, which were not available at all times due to the different control signals tested. These cameras were used for wave modelling—tuning the wave spectrum to get a specific wave shape/impact—and for global flow comparisons.

Two slow speed cameras are positioned along the length of the flume, placed at $5.2\mathrm{m}$ and $7.7\mathrm{m}$ from the wavemaker. These two cameras record the wave elevations at $200\mathrm{Hz}$ and $100\mathrm{px} \times 1920\mathrm{px}$ resolution as only a narrow strip is required to compute the wave elevations, which saves postprocessing time and storage capacity.

Two additional slow speed cameras were placed at the wavemaker position which were used to record the motion of the wavemaker. The focal length was set at 25mm and 69mm. With this configuration, high resolution in the smaller amplitude motions is achieved—approximately 0.09mm with 69mm focal length—and sufficient horizontal field of view for the larger motions is obtained—about 450mm with 25mm focal length.

Synchronization

The facility is equipped with a Meinberg IRIG-B time generator. Wavemaker, cameras and data acquisition (not used during this research) are started at the desired moment through the trigger system connected to the Meinberg card, giving a synchronization uncertainty of 0.5ms. However, while the trigger system generates a synchronized IRIG-B signal to the wavemaker, the signal passes through the wavemaker control system before the wavemaker starts moving. This was found to increase the synchronization uncertainty of the wavemaker to approximately 50ms. Therefore, an IRIG-B–wavemaker synchronization was required to compare different experiments.

6.2 Selection of waves

In Chapter 2 the definition of the wave amplitude spectrum was introduced. From the investigation of the amplitude spectrums most commonly used in coastal and marine engineering, it was concluded that neither of them was a good candidate to achieve good quality focused waves due to reflections of the shorter wave components, propagating at the wave front, before focusing occurs, Figure 2.7. The Ricker spectrum was found to be ideal, as the leading shorter waves are removed from the wavelet. Additionally, it was proven to perform exceptionally well in wave focusing experiments as presented by Kimmoun et al. (2010), resulting in a stable and smooth wave shape.

Using the Ricker amplitude spectrum formulation presented in this thesis, eq. (2.35), and the phase speed method as the wave focusing technique, section 2.4; five parameters are found that control the breaking wave shape: (1) the peak frequency of the amplitude spectrum, ω_p, (2) the wave crest height, H_c, (3 and 4) the amplitude distribution of the spectrum in the lower and higher frequencies, determined by β_l and β_h; and (5) the focal point, x_p. During the first campaign of experiments, the goal was to obtain a set of waves presenting differing characteristics that were of interest not only for this thesis but also for future research in the facility. Olivier Kimmoun was assisting during wave modelling and wave selection (observations on wave modelling are given at the end of this section). Three waves were sought:

C3. A wave with a rounded wave crest and a gas pocket size that were rather small. Numerical and experimental studies in wave focusing have shown that a small part of the mechanical energy of the liquid is progressively given to the gas as the breaking wave gets closer to the impact wall. The larger the density ratio gas-liquid, the larger the transfer of energy (Etienne et al., 2018). The result is a delay in the wave front for increasing density ratios. Results extracted from Karimi et al. (2016) showing the effect are presented in Figure 6.2. As pressure variations were intended, increasing/reducing the density ratio, the wave was selected such that the shift in the wave front does not result in extremely unstable wave crests when the DR is increased.

    The chosen wave is a focused wave at $x_\text{f} = 9.955\text{m}$ with a wave crest height of $H_\text{c} = 155\text{mm}$ and a peak frequency $\omega_\text{p} = 1.85\text{rads}^{-1}$. The distribution of the amplitude is given by $\beta_\text{l} = 0.70$ and $\beta_\text{h} = 0.60$, which leads to a small gas pocket size and a rounded wave crest.

C12. A wave with a quasi-unstable wave crest and a large gas pocket size at ambient conditions. This wave is intended to give understanding on the influence of the DR in the development of wave crest instabilities.

    The wave is achieved by an increase of the wave crest height to $H_\text{c} = 170\text{mm}$, a shift of the focal point to $x_\text{p} = 10.045\text{m}$ and a decrease of the amplitude in the lower and higher frequencies, $\beta_\text{l} = 0.6$ and $\beta_\text{h} = 0.5$; while keeping the peak frequency at $\omega_\text{p} = 1.85\text{rad s}^{-1}$.

C13. A wave representative of a flip-through impact (a focused wave with a flat wave front). No

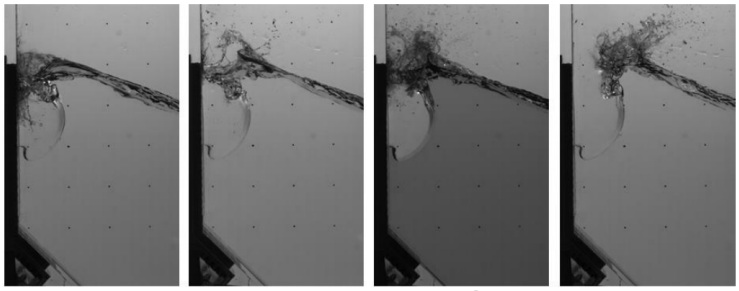

(a) Water + Helium (DR=0.0003) (b) Water + air (DR=0.001) (c) PST + (SF_6+N_2) (DR=0.001) (d) Water + (SF_6+N_2) (DR=0.004)

Figure 6.2: Effects of the density ratio in the breaking wave due to transfer of energy (Karimi et al., 2016).

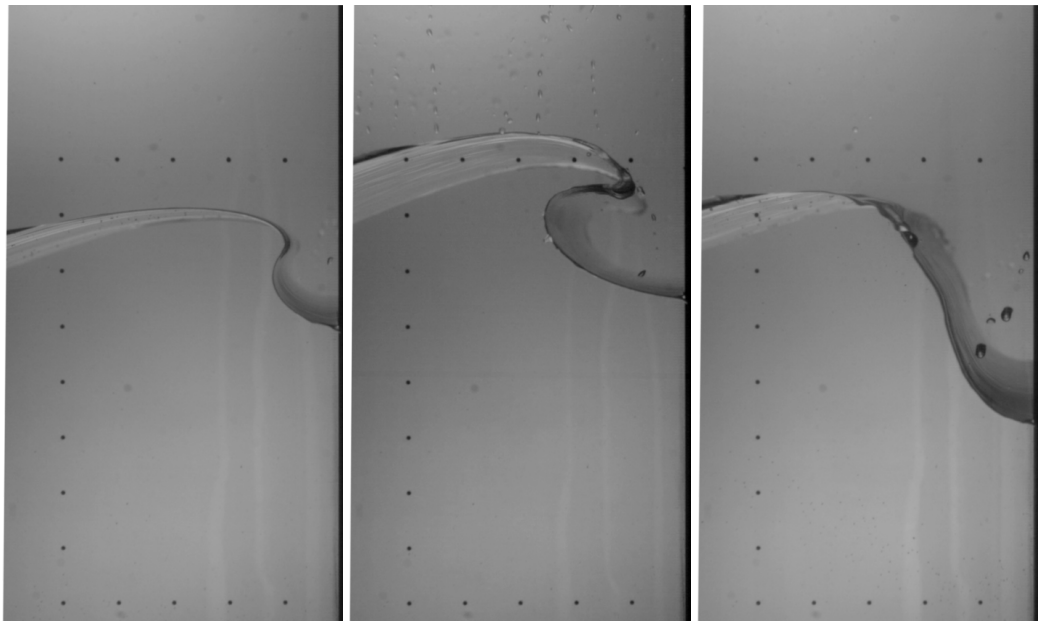

(a) Wave C3. **(b)** Wave C12. **(c)** Wave C13.

Figure 6.3: The three different waves chosen for the experiments carried out in the MWL.

gas pocket is present in this kind of waves.

The wave is challenging to get with the Ricker wave spectrum. In the literature, this kind of wave is often obtained after the early breaking of the small wave components leading the wave train. However, early breaking was barely observed using the Ricker spectrum, requiring combinations of wave height and amplitude of the higher frequencies larger than usual. In addition, early breaking introduces free surface instabilities in front of the wave before it focuses, resulting in a perturbed wave crest shape, which was avoided. The closest result with the Ricker spectrum was obtained for a focal point $x_\mathrm{p} = 9.945\mathrm{m}$, a wave crest height $H_\mathrm{c} = 180\mathrm{mm}$, increasing the peak frequency $\omega_\mathrm{p} = 2.08\mathrm{rads}^{-1}$, and the same amplitude distribution as C3, $\beta_\mathrm{l} = 0.70$ and $\beta_\mathrm{h} = 0.60$.

Waves C3, C12 and C13 at ambient conditions are presented in Figure 6.3.

6.2.1 Observations during wave selection

The time invested in wave modelling was useful to gain insight in how the five parameters defining a focused wave affect its characteristics. A summary of the general trend of the wave shape when varying these values is presented below:

- Wave breaking occurs at lower amplitudes than predicted by Miche's criterion, eq. (2.31). The expression returns a minimum breaking height of approximately $H_\mathrm{b} = 340\mathrm{mm}$, whereas the wave height used during the experiments (trough to crest) is below $H < 200\mathrm{mm}$. As discussed in section 2, the expression is valid for one steady wave. When several wave components are present, wave breaking occurs at smaller wave heights.
- When the wave crest height is set too high—for instance over Miche's criterion—early breaking of the shorter wave components occurs before focusing, usually resulting in a flip-through impact if the focal point is set appropriately. Nevertheless, the free surface is perturbed.
- Reducing the peak period while keeping the amplitude distribution constant generally translates to a thicker wave crest; and increasing the peak period results in a thinner wave crest.
- Wave crest stability is closely related to the amplitude distribution and the focal point. Increasing the amplitude of lower frequencies while keeping or reducing the amplitude of the higher frequencies gives stability to the wave crest—the opposite also applies. However, when the focal point is far from the impact wall, the wave crest loses its stability.
- From the previous point, a control signal that removes almost completely the higher frequencies was run with the expectation of a thicker and more stable wave crest. It resulted in a surging wave. It was concluded that higher frequencies—unwanted due to the difficulty of their accurate generation—are required to achieve wave breaking.
- As mentioned before, it was observed a shift of the experimental focal point with respect to the theoretical one. Wave focusing occurred about $100\mathrm{mm}$ before the predicted location by linear theory. Nevertheless, a true definition of the experimental focal point does not exist. Once the wave surpasses the breaking wave height, it becomes impossible to determine if the wave components are in phase.

6.3 Image processing

The wide range of conditions for which the MWL was designed prevents the use of typical measurement devices inside the autoclave. In wave flumes, the free surface elevation is usually measured with resistive wave gauges, which operate by measuring the resistance of the water between a pair of parallel rods—the resistance is proportional to the immersion depth. As mentioned at the beginning of the chapter, demineralized water is used for the experiments in the MWL, which spoils the basic principle of the instrument: electric conductivity. In those applications that require non-intrusive techniques, sound and laser based devices are often used for the measurement of the free surface elevation. However, vacuum conditions and the use of water impede their use in the MWL. Measurements of the wavemaker motion are also required. At first, it was measured with a LVDT (Linear Variable Differential Transformer). A electromechanical transducer that converts the rectilinear motion of the paddle to a corresponding electrical signal. However, the apparatus rely on the magnetic field generated by an internal winding. Initial suspicions about its nonlinear behavior on high temperatures were confirmed during the commissioning of the heating system, so the device was removed from the autoclave. In this scenario, the best choice for measuring the free surface elevation and the paddle motion is by means of video recordings, meeting the requirements of a non-intrusive and temperature/pressure/gas-composition insensitive device. Two image processing algorithms were developed to obtain measurements of the free surface elevation and the paddle motion from the slow speed cameras. The basis of the techniques used are described in the following sections.

6.3.1 Wavemaker motion

The lateral surface of the wavemaker was fitted with 4×4 chessboard patterns. The chessboard provides a region were the intensities of the gray-scale image are highly distinguishable from its surroundings and, therefore, the wavemaker motion can be accurately measured. While thresholding would be a very simple method to implement for segmenting the images into binary images—which can then be used to perform object recognition—it requires a clean image, good lighting conditions and fine tuning of the threshold value to perform accurate object tracking—conditions that are not always met. Droplets are quite often found on the glass in front of the

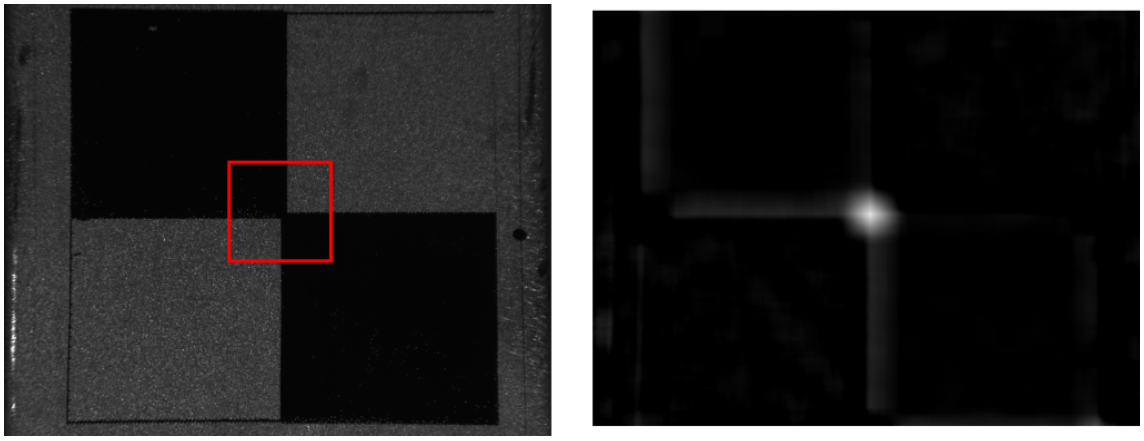

Figure 6.4: Example of the cross-correlation method for wavemaker tracking on a 2×2 sticker. The pattern was updated to a 4×4 chessboard later on to increase the correlation points.

chessboard pattern and condensation on the observation windows when increasing the temperature lead to light reflections and a blurred image. Therefore, thresholding was discarded as the image processing method for this application. Instead, a cross correlation method was preferred. It computes the sliding inner-product of a reference image over the obtained data. The location of the maximum value from the cross-correlation is the position where the reference image matches the most with the given data. To increase the tracking accuracy, the reference image is directly obtained from the data, therefore being subjected to the same lighting/perspective conditions as the original image, which maximizes the correlation value. An example of the method is shown in Figure 6.4 at the first frame of a recording. The left image in the figure shows the original image and the area chosen for the cross-correlation marked by red edges. On the right, the result of the cross correlation is shown. The highest intensity value in the right image is the tracking point. The efficiency of the algorithm improves when the size of the reference image (red square) increases, being maximum when the reference image is the same size as the image data. The reason is that the number of passes that the algorithm needs to perform in the cross correlation decreases as the height/width increases.

The image processing method described above was used for the two slow speed cameras recording the wavemaker motion. The algorithm tracks the wavemaker motion using the zoomed-in camera until the moment the chessboard pattern is out of the field of view. In that moment, the position of the wavemaker is given by the zoomed-out camera. The position of the wavemaker is given again by the zoomed-in camera when it passes through its field of view.

Once the position of the paddle is determined in the image (in pixels), it is scaled with a calibration file. Different methods were implemented to perform the calibration during the research In the end, reference marks were sticked to the glass covering the entire field of view, and the calibration file was generated from the position of the marks in the image knowing the distance between them.

6.3.2 Wave elevations

Getting the wave elevations required a more complex image processing technique based on the Hough transform, a technique used in image analysis, computer vision and digital image processing for feature extraction—the identification of arbitrary shapes, most commonly lines, circles and ellipses. Nevertheless, many solutions were tried in an attempt to get accurate measurements of the free surface elevation before the Hough transform was used. These can be grouped in two main techniques described below. Consider Figure 6.5 as the image to process.

- Intensity based technique: from an initial evaluation of the data, it was observed that there were two areas clearly differentiated: (1) the wet region, demarcated by very low values of intensity and (2) the dry region above the free surface line, where the values of intensity cover a wide range. The free surface line delimits both areas, being darker than the surrounding areas, see Figure 6.6.

Figure 6.5: Example of a camera image from where the free surface must be detected. Rotated counter-clockwise for a better use of space. The sharp dark line in the mid-bottom region (→) is the free surface line in the foreground. The blurred dark line in the mid-top region (→) is the free surface line in the background.

The main idea was to follow the peak in intensity of the meniscus using the free surface elevation from the previous frame to determine its new elevation. However, the presence of particles[1] in the water led to misdetections that affected the detection in the next images. Blurring, gradient of intensities and polinomial extrapolation from the previous detections were applied unsuccessfully. Further information on intensity based techniques can be found in Basu (2002) and on its application in Spinka IV et al. (2009).

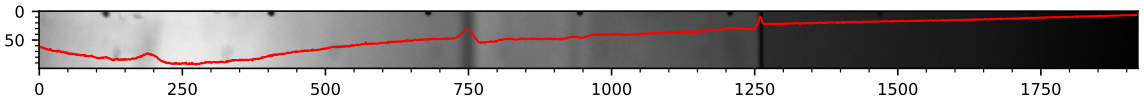

Figure 6.6: Intensities along the centerline of the image.

- Edge detector technique: the Canny edge detector—a multi-stage algorithm to detect a wide range of edges in images—was used. The algorithm returns a binary image with the detected edges. Particles, the reference dots in the glass and any other feature of the image are nicely detected if the two threshold values required by the Canny algorithm are well calibrated. The binary image was then used as input in a contour function that identifies each feature and stores them in different variables. As a result, the edges could be sorted by length such that small size detections were removed. However, there were two issues with the technique: (1) the selection of the threshold values. Due to the small difference in intensities between the free surface line and the wet region, low threshold values are required, leading to the detection of many edges in the image; and (2) identifying the free surface line from the detected contours. In the absence of dirt in the water, the free surface is perfectly detected and easily identifiable, see Figure 6.7. Nevertheless, when particles are found, and they are close to the free surface, they are grouped as one contour line and, therefore, cannot be removed when sorting by length; which results in a hardly identifiable free surface line, see Figure 6.8. For details on the Canny edge detector see Rong et al. (2014) and on its application Spinka IV et al. (2009).

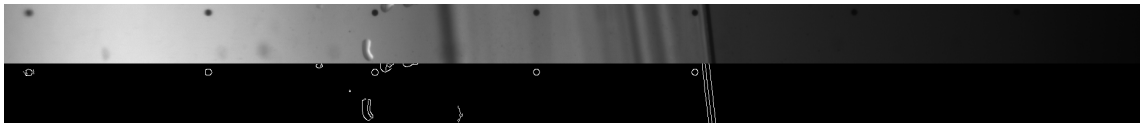

Figure 6.7: Canny edge detector applied to an image with clean water.

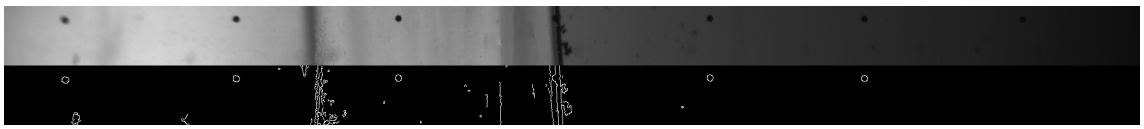

Figure 6.8: Canny edge detector applied to an image with dirt in the water.

[1] The origin of these particles is unknown at the moment of writing.

Table 6.1: Number of repetitions each wave was run at each pressure condition.

Wave	Absolute pressure										
	0.4	0.5	0.6	0.7	0.8	0.9	1.0	1.3	1.7	2.0	bar
C3	1	–	1	–	1	–	–	–	–	–	#
C12	1	1	2	1	2	1	1	2	2	2	#
C13	1	–	1	–	1	–	–	–	–	–	#

The Hough transform

The solution was a combination of image processing techniques mainly using the OpenCV library for Python (Bradski, 2000). First of all, a bilateral filter was applied to the image. The result is a blurred image, which removes unwanted noise, while keeping the edges—the free surface—fairly sharp. Then, adaptive thresholding is applied to compute the edges of the image while removing the lighting difference between the wet and dry region. The threshold value is calculated automatically for each pixel from the Gaussian mean of the neighborhood values. The binary image goes then through a dilation kernel—a matrix that, when multiplied by the image, increases the size of the detected edges—ensuring that all detected points in the free surface are connected. Lastly, the Hough (lines) transform of the image is computed, returning all detected lines in the image. Due to the camera orientation, the line of interest is always the bottommost one, the other detected lines are discarded. The result of the detection in the same image as before is shown in Figure 6.9. As the method only detects lines in the binary image, particles or any other feature are not detected by the algorithm, resulting in a more reliable method for measuring the wave elevations. The free surface elevation is taken at the centerline of the image and scaled with a calibration file generated from the laser-printed reference dots in the glass.

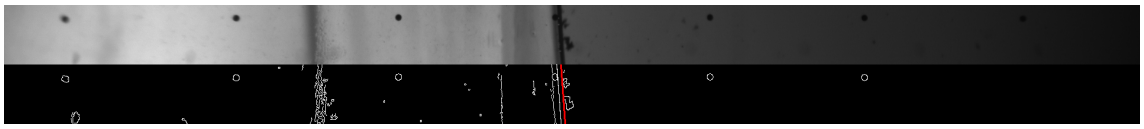

Figure 6.9: Free surface elevation detected using the Hough transform with dirt in the water.

6.4 Results and analysis

A total of 140 waves were run in the facility during the thesis. Nevertheless, as the facility was still in the commissioning phase, most of them were used for the evaluation of the different systems. In addition, the algorithms for measuring the wavemaker motion and the wave elevations have been developed in parallel with the experiments, suffering from continuous modifications. As a result, meaningful data was collected only for the last 20 experiments (tests 114 to 130 and 132 to 138) from the 140 total waves. These experiments were run at different pressure conditions, ranging from 0.4bar to 2bar, over a period of two days. One breaking wave was generated approximately every 20 minutes. Table 6.1 shows the number of repetitions at each pressure condition. As can be seen, two repetitions with the same pressure conditions are only found for wave C12. The named wave is also the only one that was run at higher pressures due to schedule constrictions. The measured water depths are shown in Table 6.2.

The results will be presented in the following order: the repetitions of wave C12 at the same conditions are analysed in section 6.4.1, evaluating the repeatability of the paddle motion and the repeatability of the global flow of the breaking wave; and in section 6.4.2, the wave C12 at different conditions is evaluated from which conclusions about the effect of pressure in wave propagation are drawn. Waves C3 and C13 will not be considered due to the lack of repetitions. The experiments will be referred to as Cxx-yy-n, where 'xx' is the wave type, 'yy' the absolute pressure and 'n' the repetition, for instance: C12-07-0 is wave C12, pressure 0.7bar, repetition 0.

Table 6.2: Water depth measured before wave generation.

Wave	Rep.	Absolute pressure										
		0.4	0.5	0.6	0.7	0.8	0.9	1.0	1.3	1.7	2.0	bar
C3	0	399.2	–	399.2	–	397.2	–	–	–	–	–	mm
C12	0	399.4	399.4	399.3	399.4	399.4	399.4	399.7	400.0	400.2	400.1	mm
	1	–	–	398.5	–	397.2	–	–	400.1	400.3	399.9	mm
C13	0	399.3	–	398.4	–	397.2	–	–	–	–	–	mm

6.4.1 Wave C12 – same pressure

The results obtained from the two repetitions at pressures $P_{\mathrm{a}} = (0.6,\ 0.8,\ 1.3,\ 1.7,\ 2.0)\mathrm{bar}$ using wave C12 are presented and discussed in this section. The water depth difference between repetitions was kept below $0.2\mathrm{mm}$ for waves generated at pressures above atmospheric pressure. Less care was taken below atmospheric pressure[2], with differences that reached $\Delta h = 2.5\mathrm{mm}$, see Table 6.2.

C12-06-0 and C12-06-1

The wavemaker motion compared to the steering signal is shown in Figure 6.10a. Three subplots were included to adequately compare both signals. Additionally, the time shift required to have the wavemaker synchronized with the IRIG-B time is shown in the caption. $1\mathrm{s}$ of the synchronization time was a delay manually set in the control panel. About $0.8\mathrm{s}$ was found to be the mean delay between the trigger signal and the wavemaker motion; and approximately $50\mathrm{ms}$ is the actual uncertainty in the starting time of the wavemaker.

The wave elevations are depicted in Figure 6.10b (elevation at $x = -4.8\mathrm{m}$ from the focal point) and Figure 6.10c (elevation at $x = -2.3\mathrm{m}$ from the focal point) with three details each. The similarity parameter as defined in the previous chapter is also included in the caption. The resulting wave shapes at four different instants separated by $10\mathrm{ms}$ are shown in Figure 6.11.

Many things draw the attention in these results. To keep a clear direction of analysis, the results will be evaluated from the observable differences in the breaking wave, Figure 6.11, to the reasons these differences are observed; a direction from general to details. Three differences are observed in the wave shape in Figure 6.11: (1) the size of the gas pocket at the moment of impact, (2) the wave crest height, which is more apparent in the leftmost frames; and (3) presence of more wave instabilities in the upper part of the gas pocket in wave C12-06-1. The experiments were run with a difference in the water depth of $0.8\mathrm{mm}$—which is twice the maximum allowable difference derived theoretically in the previous chapter, Table 4.6. With this difference, the conclusions given in the previous chapter were that the longer waves propagating in shallower water would arrive later at the focal point and, additionally, the focal point would get closer to the impact wall the shallower the water is. The measurements of the wave elevations show that, indeed, the last wave of the train in Figure 6.10c, arrives around $5\mathrm{ms}$ later when the water depth is shallower (barely appreciable in the figure). These results might seem contradictory at first: the wave elevations show that the wave propagates slower and, therefore, the focal point should be closer to the wall; and, however, the wave propagating in the shallower water (C12-06-01) has the larger gas pocket. To understand the reason this is happening, one should avoid relating the focal point with the gas pocket size. As stated in the previous chapter: there is no clear definition of focal point in experiments; being these two waves a good example. Water depth has a larger effect in the longer wave components forming the wave train. Thus, the longer wave components in C12-06-1 will be farther from the focal point than the longer wave components in C12-06-1, while the theoretical focal point of the shorter waves will remain unchanged. In consequence, the wave crest height at the focal time for wave C12-06-0 will be larger than C12-06-1 (think of summation of wave components with the largest wave at different phase). This is observed in the first frame in Figure

[2] Accurately controlling the water depth took longer than expected—the different subsystems had to be controlled manually at the moment—and the facility was under a tight schedule, therefore limiting the available time for water depth adjustments.

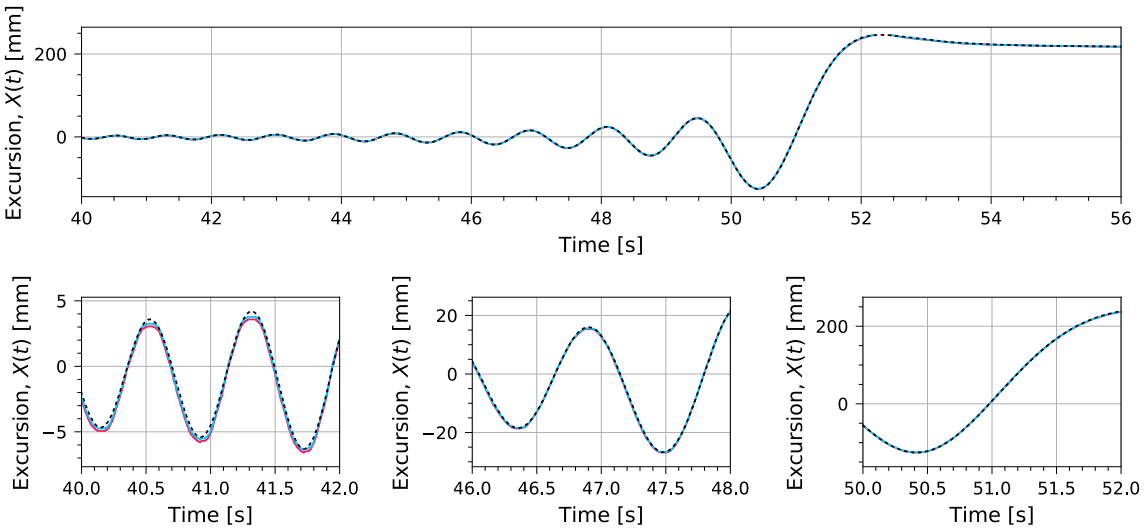

(a) Comparison of the wavemaker motion. Control signal (- - -). Δt(—)= $+1.840$s. Δt(—)= $+1.839$s

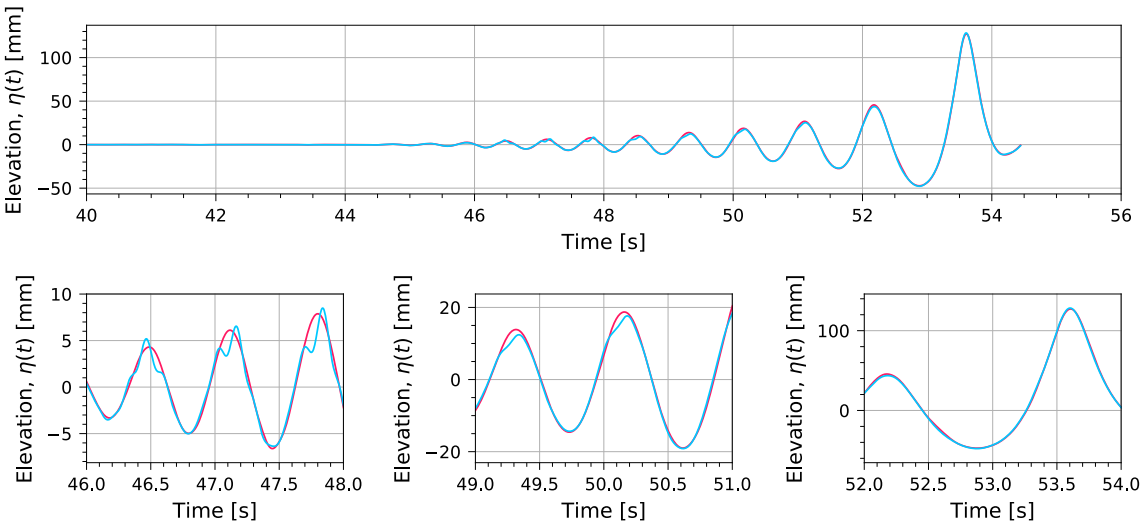

(b) Wave elevations at $x = -4.8$m ($Q = 0.018$)

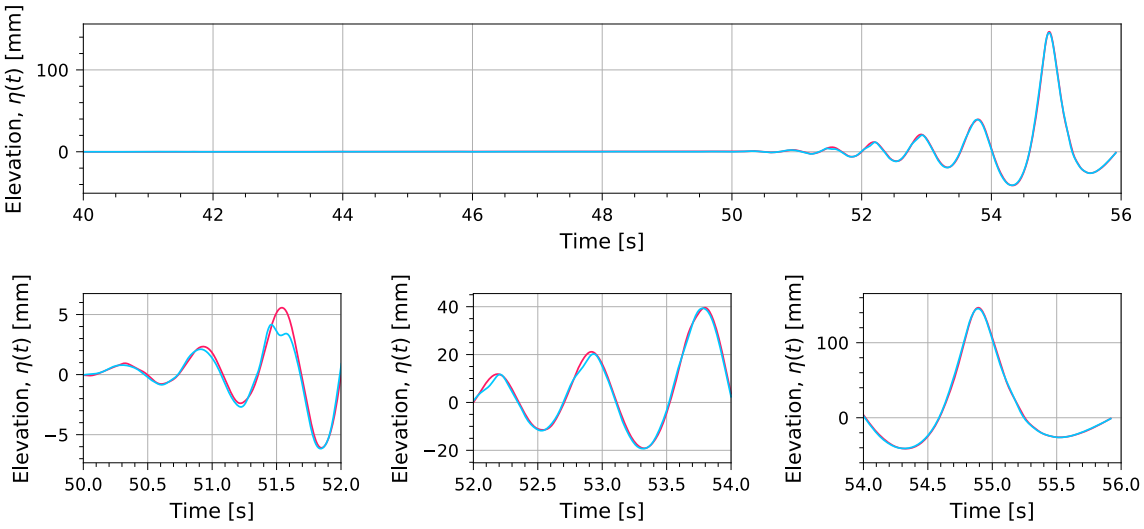

(c) Wave elevations at $x = -2.3$m ($Q = 0.018$).

Figure 6.10: Results from runs C12-06-0 (—) and C12-06-1 (—).

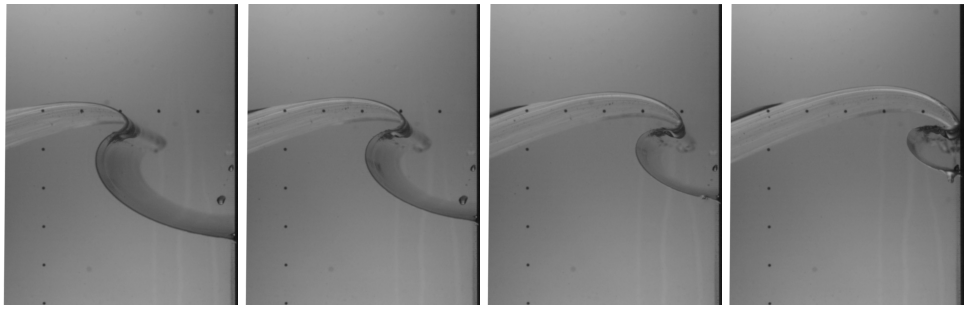

(a) C12-06-0

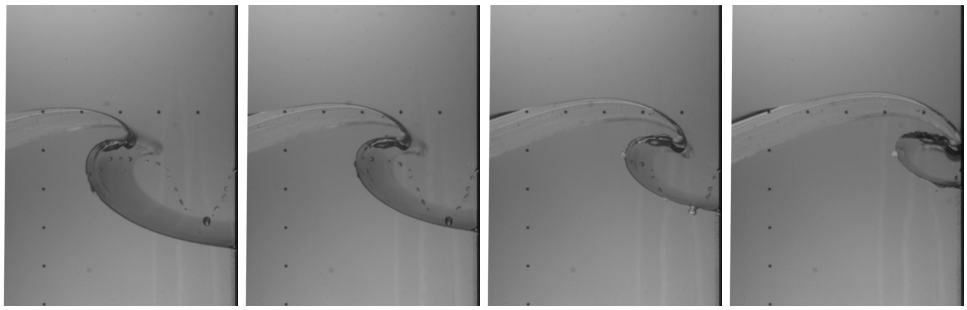

(b) C12-06-1

Figure 6.11: Wave shapes at different instances before impact ($\Delta t = 10\text{ms}$) for wave C12 at $P_\text{a} = 0.6\text{bar}$.

6.11. In addition, when the shorter wave components reach the focal point, the height of the wave is already above the breaking height—independently of whether the larger wave components are in phase or not—and the wave starts overturning. As wave C12-06-1 is missing energy from the larger wave components in the wave crest, this becomes thinner and more unstable, which is shown in the following frames. The gas pocket becoming larger is also related to wave energy. When the wave loses energy in the lower frequencies, the spectrum of the wave shift towards higher frequencies. As a result, the peak period characterizing the wave gets shorter—smaller wavelength. Entering in Miche's criterion with this wave characteristics results in a lower breaking wave height, which means the wave starts breaking earlier. Altogether, the gas pocket becomes larger.

Figure 6.10 also shows some interesting details. First of all, the similarity parameter, Q, is three times larger than the maximum value for repeatable results derived in the previous chapter, $Q_\text{exp} \leq 0.006$. With the repeatability of the wavemaker still not discussed, having a water depth difference that is twice the theoretical maximum allowable explains the dissimilarity.

Another phenomena that draws the attention are the fluctuations of the free surface elevations in the crests, for instance at $t \in [46, 48]\text{s}$. While it was thought to be a problem in the detection algorithm, the wabbles are consequence of surface tension effects in the meniscus—which is the line used for detection of the free surface. When a wave propagates through the flume, the side walls are being wet by the wave crest. The following wave in the wave train is higher and, therefore, the wave trough propagates in a wetted surface while the wave crest does it over a dry surface. Looking at this effect at a specific longitudinal position—like the camera does—a column of water propagates in height first over a wetted glass, and then over a dry glass. In the transition, the meniscus 'sticks' for a time to the dry glass, which explains the oscillation. An example is shown in Figure 6.12

Considering the wavemaker motion, 'large' relative differences are appreciable in the lower amplitude motions in Figure 6.10a. Nevertheless, the magnitude of the difference is not clear. Figure 6.13 shows the five seconds average error w.r.t. the steering file measured from the camera and compares them with the design criteria established by MARIN, Table 4.2. It is also included the

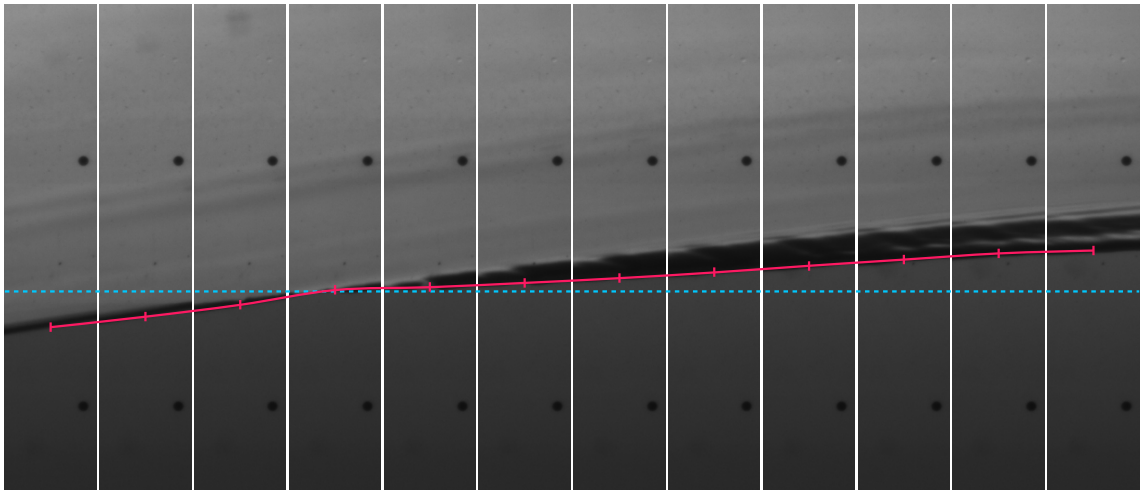

Figure 6.12: Example of the meniscus effect shown in the wave elevation measurements consequence of the friction difference when the wave crest propagates on a dry wall. (- - -) represents the intersection from wet to dry glass and (——) the free surface elevation. $\Delta t = 10\text{ms}$.

difference between the two signals as it might occur that large wavemaker motion errors are found but the error is repeatable, leading to zero motion error between experiments. As can be seen, larger errors than the design criteria are found for the smaller amplitudes, $X(t < 45\text{s}) < 7.5\text{mm}$. The error of the motion between experiments gets closer to the design criteria, so it can be concluded that the errors in the wave shape are mainly consequence of the water depth difference.

C12-08-0 and C12-08-1

The wavemaker motion compared to the steering signal for wave C12 at $P_\text{a} = 0.8\text{bar}$ are shown in figures 6.14a and 6.16. The wave elevations at $x = -4.8\text{m}$ in Figure 6.14b, and at $x = -2.3\text{m}$ in Figure 6.14c. The resulting wave shapes at four instance before impact are depicted in Figure 6.15.

The result of a larger difference in the water depth, $\Delta h = 2.2\text{mm}$, results in larger values of the similarity parameter, $Q(x = -4.8) = 0.023$ and $Q(x = -2.3) = 0.028$. The mean five seconds averaged wavemaker motion errors compared to the control signal are above the maximum motion error specified by the design criteria, while the difference of the paddle motion between the two repetitions is below the design criteria. This was found to be a constant during the experiments. The design requirements in the higher frequencies seem to be too high to be complied.

The results in the breaking wave shape are evident in Figure 6.15. As before, the wave crest height is lower in C12-08-1, the wave crest is thinner and the gas pocket size is slightly larger as consequence of the shallower water depth.

C12-13-0 and C12-13-1

The results of the waves generated with approximately the same water depth conditions bring more conclusions to the table. First of all, the differences in the global flow of the wave are smaller and the wave crest thickness is very similar, though some differences are still appreciable in the tip of the crest (considered local flow), see Figure 6.18. Regarding the wavemaker errors, Figure 6.17a, while the mean five seconds error of the paddle motion is still above the design criteria, it is found that the differences between the two repetitions are very low. With a difference in the water depth equal to $\Delta h = 0.1\text{mm}$ and the difference in the paddle motion negligible, it is expected the value of the similarity parameter, Q, to be below the repeatability criteria $Q_\text{exp} \leq 0.006$. Nevertheless, when the quotient is computed from the wave elevations, Figure 6.17b and Figure 6.17c, the value is still above the repeatability criteria, $Q(x = -4.8) = 0.017$ and $Q(x =$

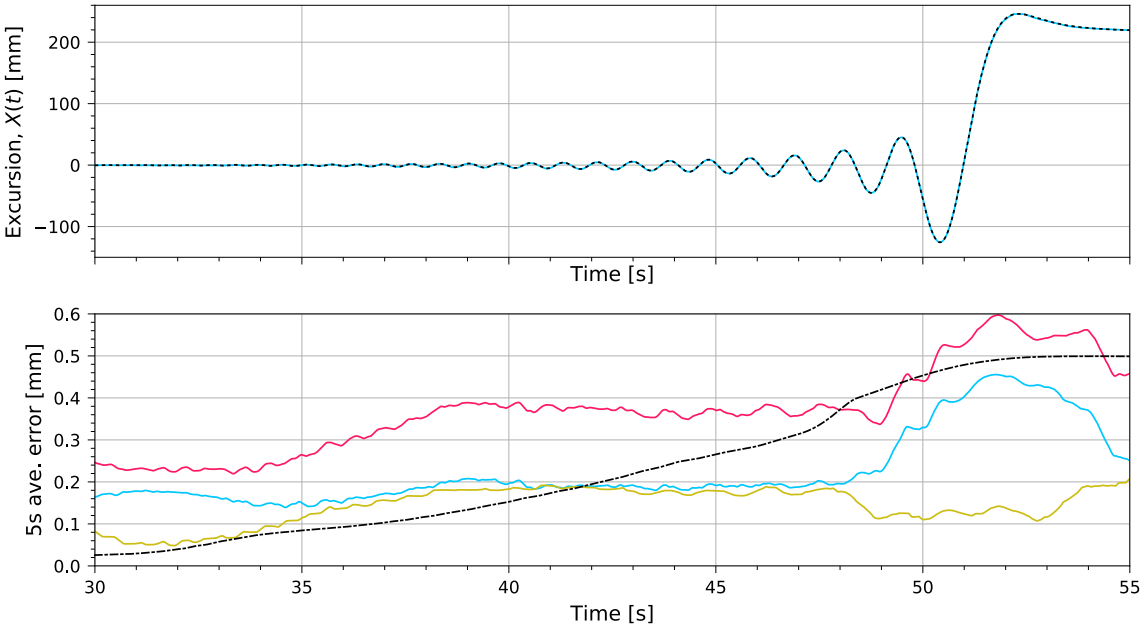

Figure 6.13: Five seconds average error of the paddle motion for waves C12-06-0 (——) and C12-06-1 (——) w.r.t the control signal (- - -). The maximum allowable five seconds average errors, Table 4.2, are also plotted (-·-·-). The difference of the wavemaker motion errors is included to check the variability of the error (——).

$-2.3) = 0.010$. It was found that the presence of the meniscus effect in the measurement of the wave elevation leads to these larger values as will be shown at $P_{\mathrm{a}} = 2.0\mathrm{bar}$.

C12-17-0 and C12-17-1

Due to synchronization errors in the slow speed cameras, results of the free surface elevation and paddle motion are not available for these waves. The high speed images will be included when evaluating the pressure effects in the wave shape in section 6.4.2.

C12-20-0 and C12-20-1

This set of waves confirmed the speculation of the similarity parameter being highly affected by the meniscus phenomenon in the wave elevations. Figure 6.20b and Figure 6.17c show the wave elevations at the camera positions. This time, two measurements of the wave elevations without the meniscus phenomenon were taken. In addition, the paddle motion difference between the experiments was close to zero. As a result, the values of the similarity parameter were below the repeatability criteria, $Q(x = -4.8) = 0.004$ and $Q(x = -2.3) = 0.005$—as expected when the difference in water depth is below the maximum derived in the previous chapter, Table 4.6, and the error in the paddle motion is negligible. The resulting focused waves are shown in Figure 6.21. No apparent difference is appreciable in the global flow from the images. To further prove that the differences in the global flow are very low, Figure 6.23 shows both images overlapped with one of the images color-shifted by the same amount towards the red and the other towards cyan. When the intensity values of both images match, the resulting image is a gray-scale image. To help understanding how well both images overlap, wave C12-06 is also included.

Observations and conclusions

A series of observations and conclusions can be made from the analysis of the data shown in the previous paragraphs:

- It was found curious that the meniscus phenomenon always occurred in the initial wave—repetition 0—and it vanished the second time the wave was run. There was only one case when both measurements of the wave elevations were taken without the effect, wave C12-20. A

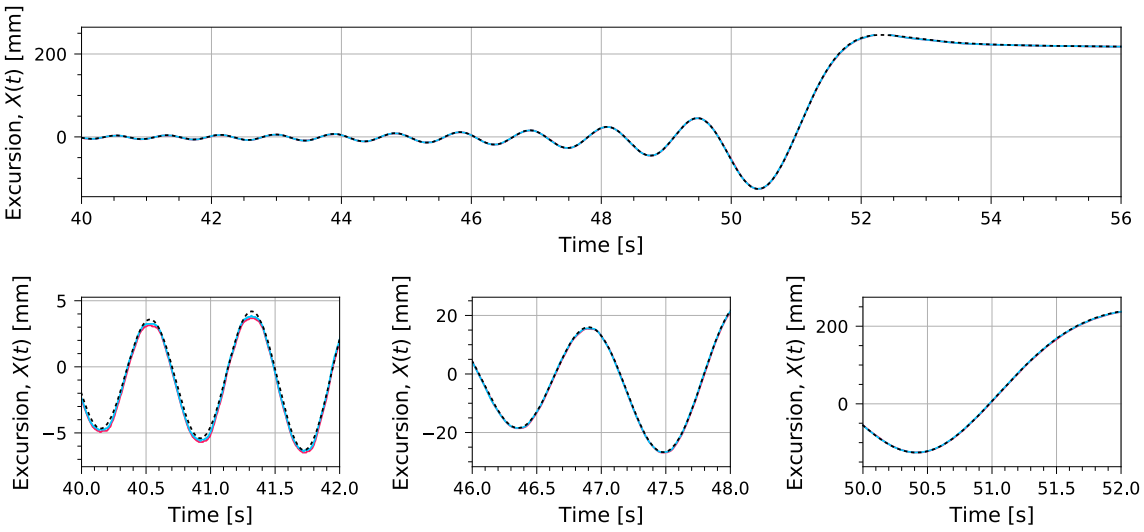

(a) Comparison of the wavemaker motion. Control signal (- - -). Δt(—)= $+1.779$s. Δt(—)= $+1.790$s

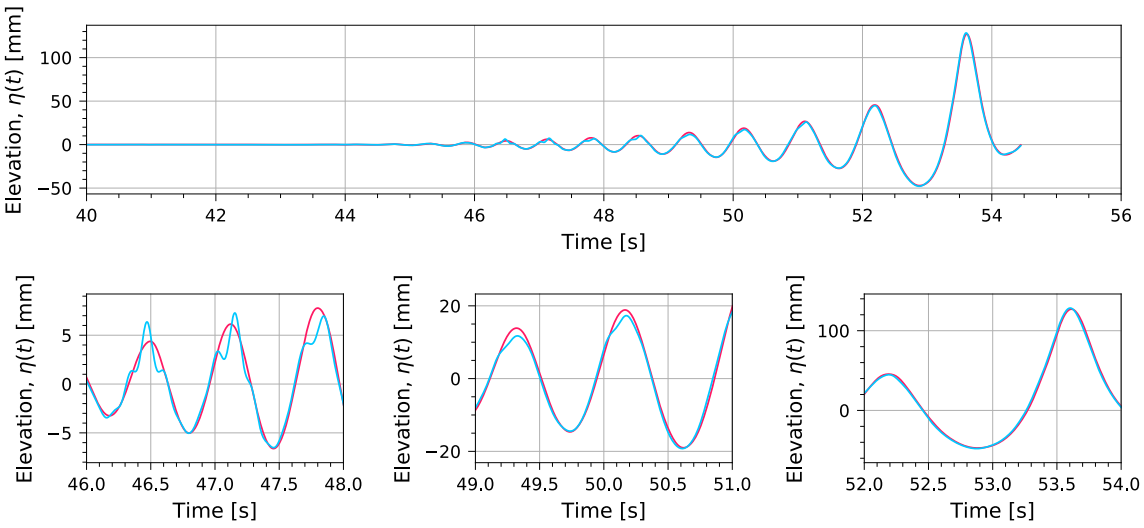

(b) Wave elevations at $x = -4.8$m ($Q = 0.023$)

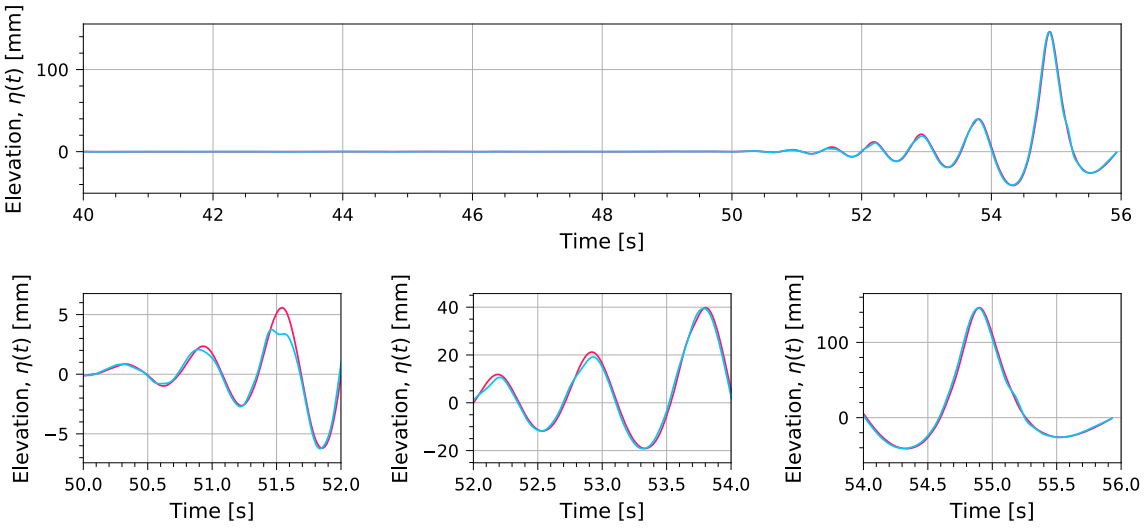

(c) Wave elevations at $x = -2.3$m ($Q = 0.028$).

Figure 6.14: Results from runs C12-08-0 (—) and C12-08-1 (—).

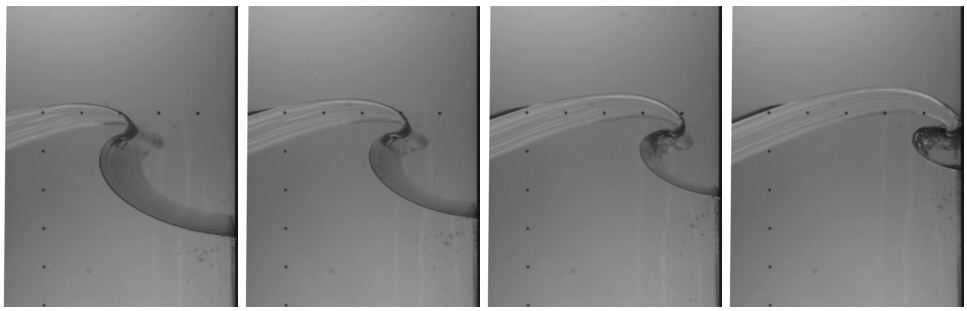

(a) C12-08-0

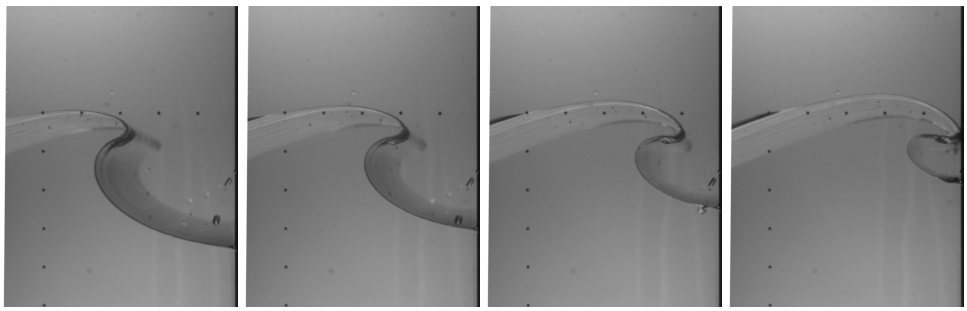

(b) C12-08-1

Figure 6.15: Wave shapes at different instances before impact ($\Delta t = 10\text{ms}$) for wave C12 at $P_{\text{a}} = 0.8\text{bar}$.

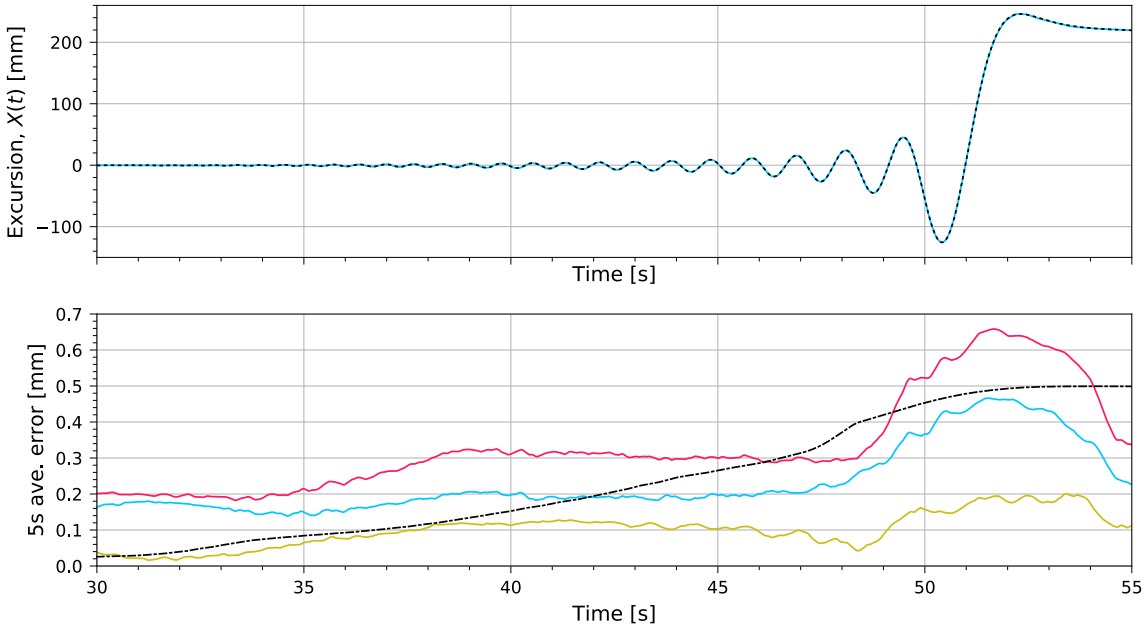

Figure 6.16: Five seconds average error of the paddle motion for waves C12-08-0 (——) and C12-08-1 (——) w.r.t the control signal (- - -). The maximum allowable five seconds average errors, Table 4.2, are also plotted (-·-·-). The difference of the wavemaker motion errors is included to check the variability of the error (——).

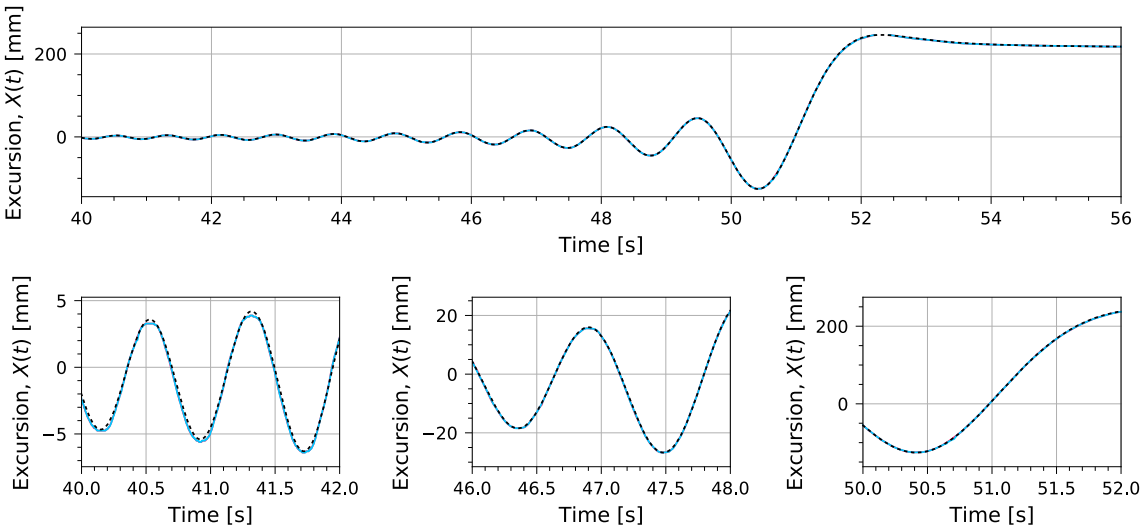

(a) Comparison of the wavemaker motion. Control signal (- - -). Δt(—)= $+1.755$s. Δt(—)= $+1.811$s

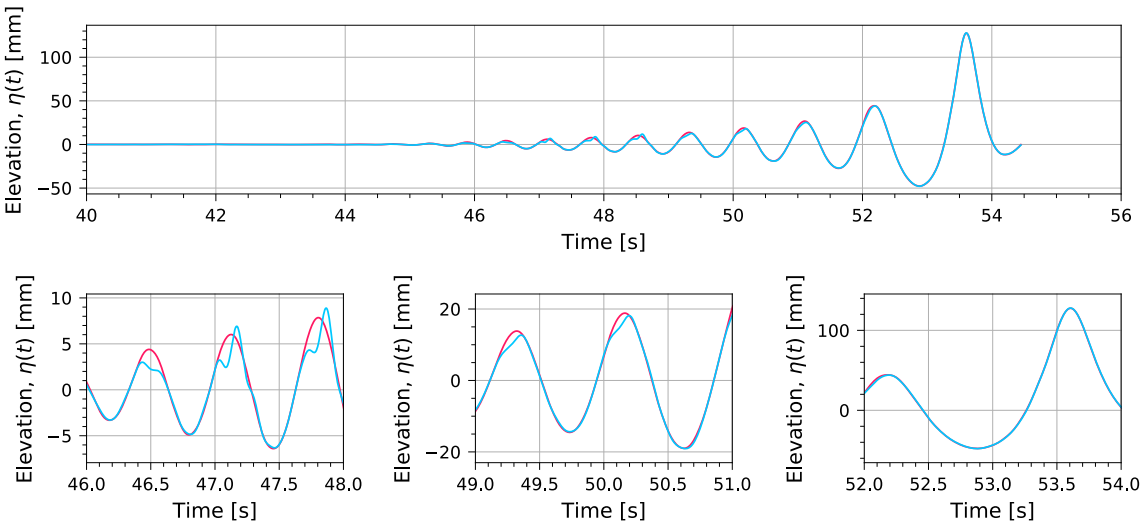

(b) Wave elevations at $x = -4.8$m ($Q = 0.017$)

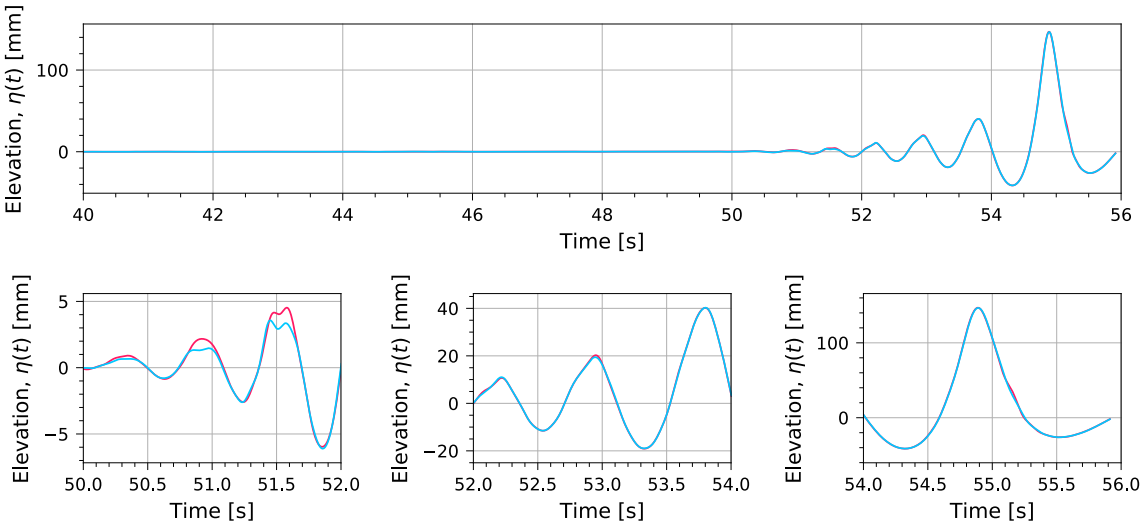

(c) Wave elevations at $x = -2.3$m ($Q = 0.010$).

Figure 6.17: Results from runs C12-13-0 (—) and C12-13-1 (—).

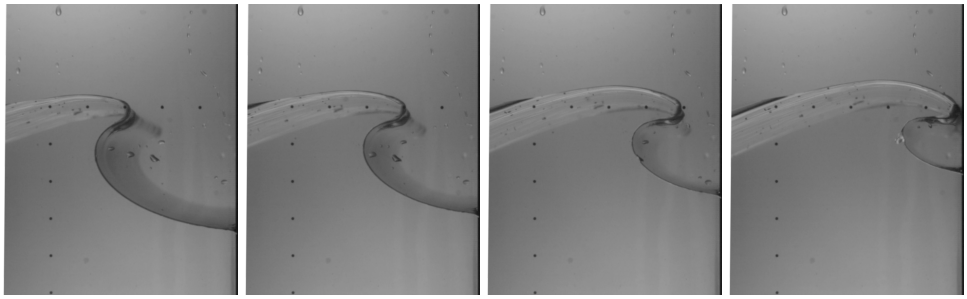

(a) C12-13-0

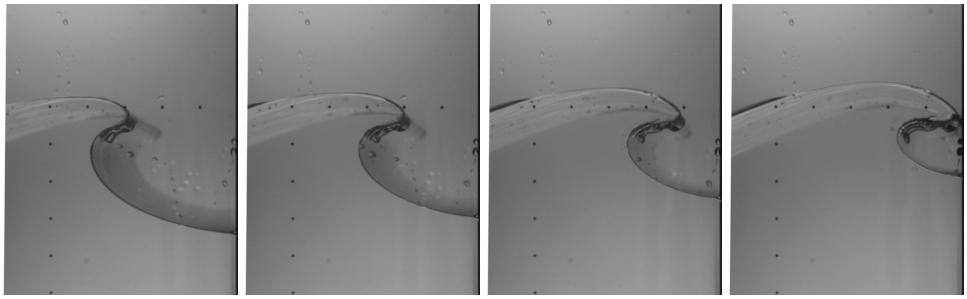

(b) C12-13-1

Figure 6.18: Wave shapes at different instances before impact ($\Delta t = 10\text{ms}$) for wave C12 at $P_\text{a} = 1.3\text{bar}$.

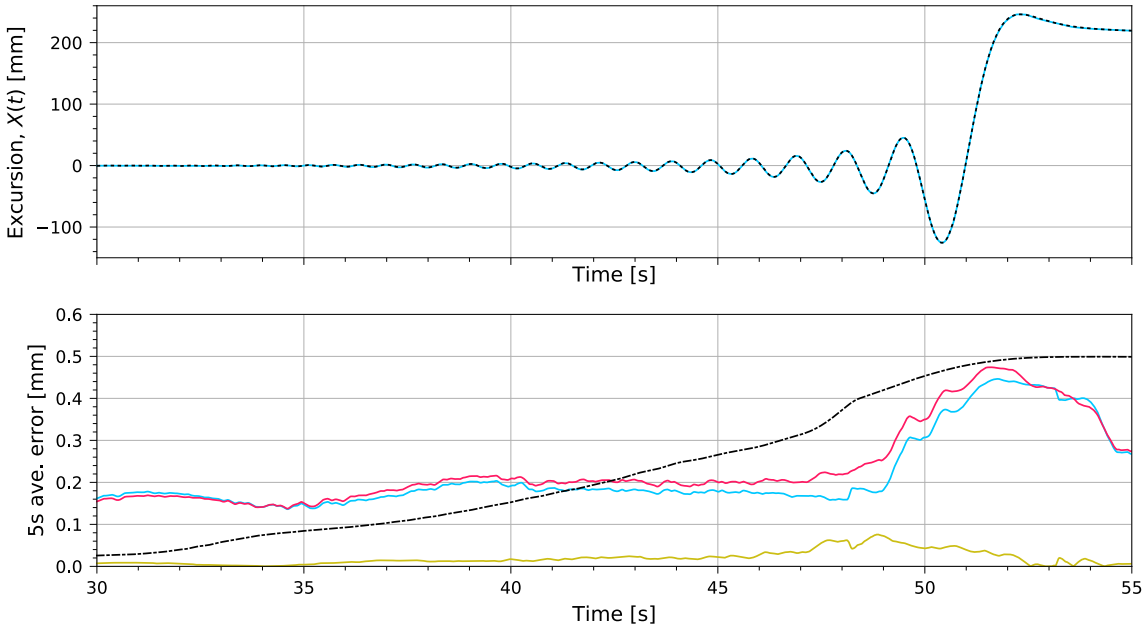

Figure 6.19: Five seconds average error of the paddle motion for waves C12-13-0 (——) and C12-13-1 (——) w.r.t the control signal (- - -). The maximum allowable five seconds average errors, Table 4.2, are also plotted (-·-·-). The difference of the wavemaker motion errors is included to check the variability of the error (——).

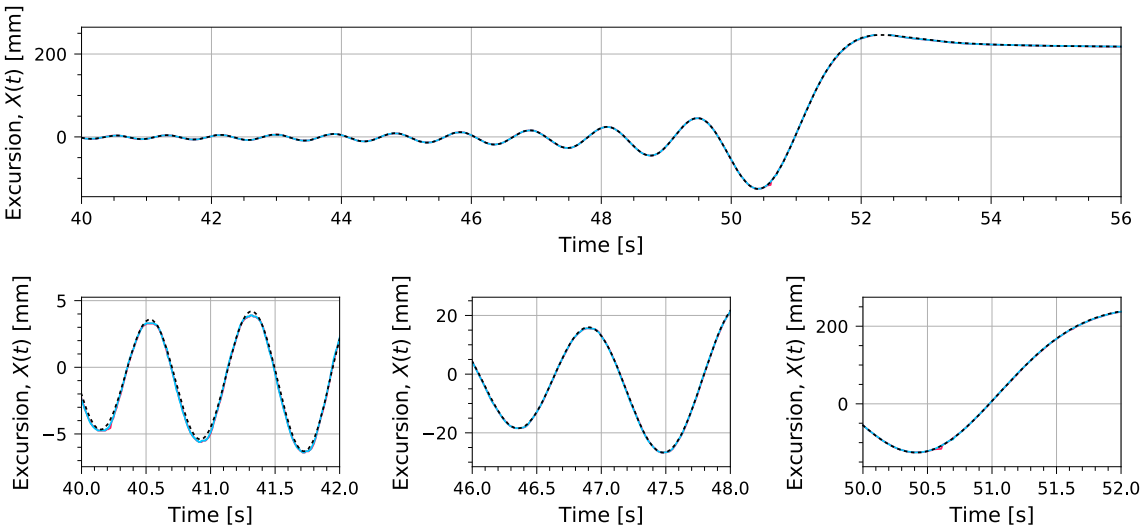

(a) Comparison of the wavemaker motion. Control signal (- - -). Δt(—)= $+1.798$s. Δt(—)= $+1.850$s

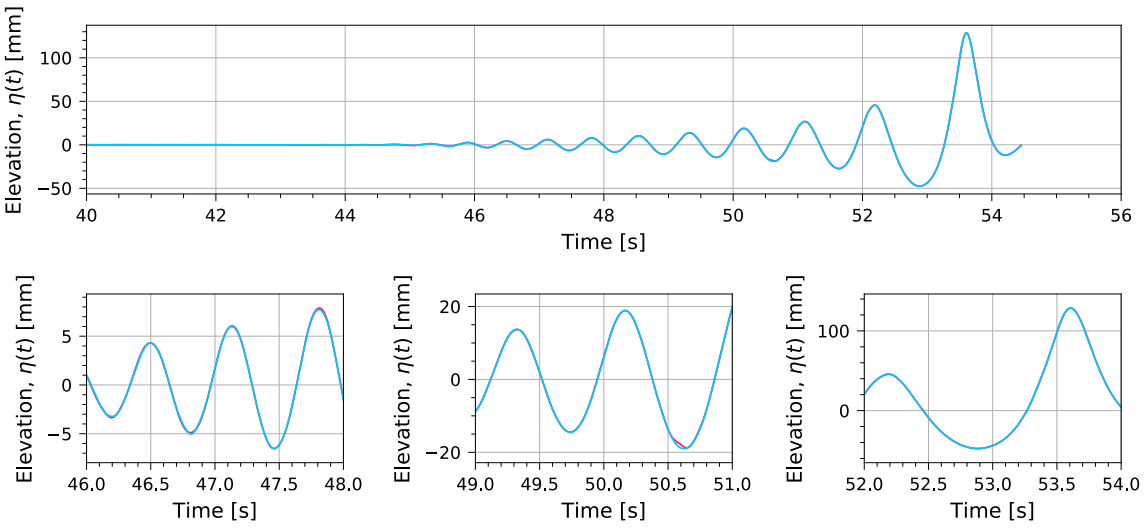

(b) Wave elevations at $x = -4.8$m ($Q = 0.004$)

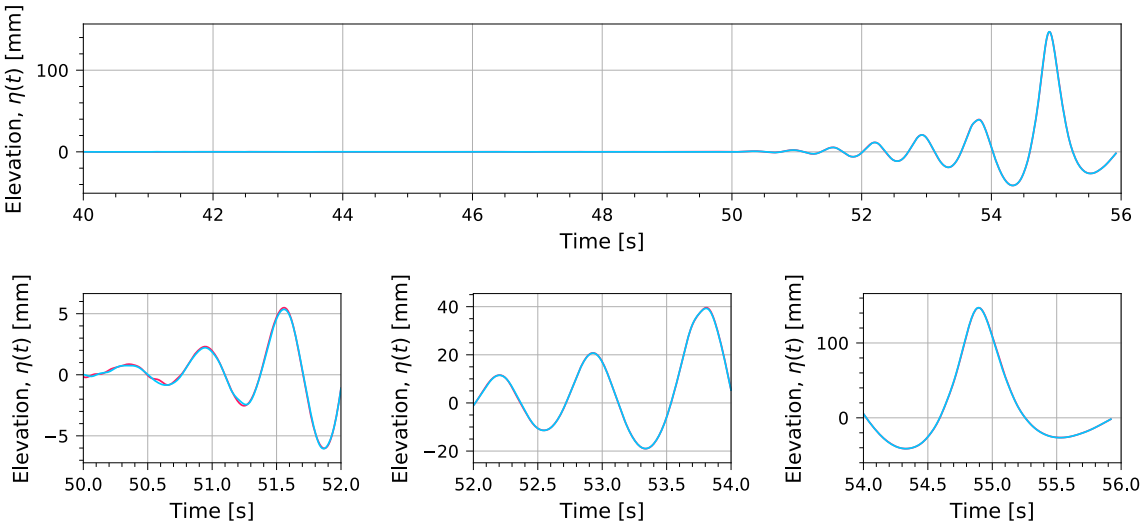

(c) Wave elevations at $x = -2.3$m ($Q = 0.005$).

Figure 6.20: Results from runs C12-20-0 (—) and C12-20-1 (—).

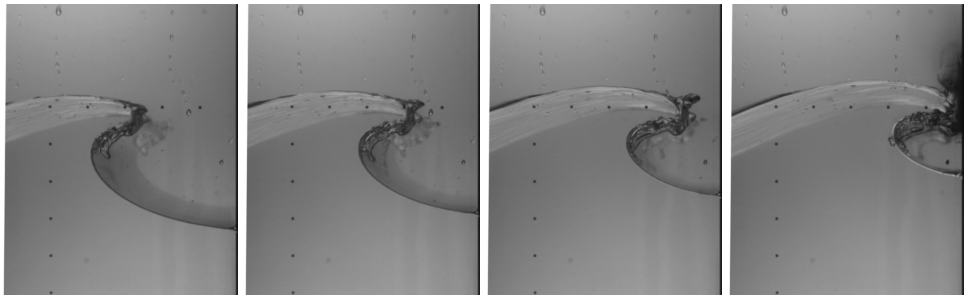

(a) C12-20-0

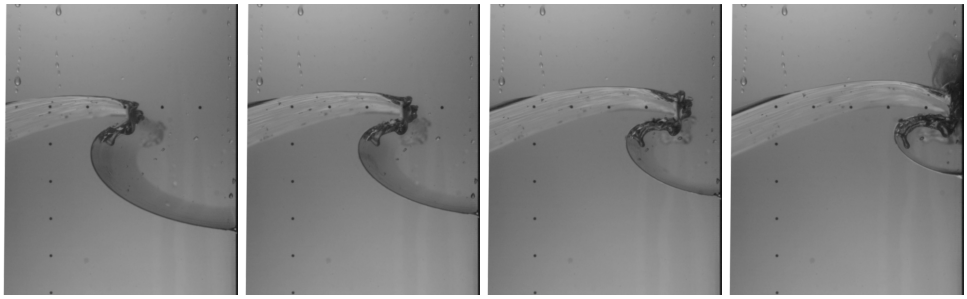

(b) C12-20-1

Figure 6.21: Wave shapes at different instances before impact ($\Delta t = 10\text{ms}$) for wave C12 at $P_\text{a} = 2.0\text{bar}$.

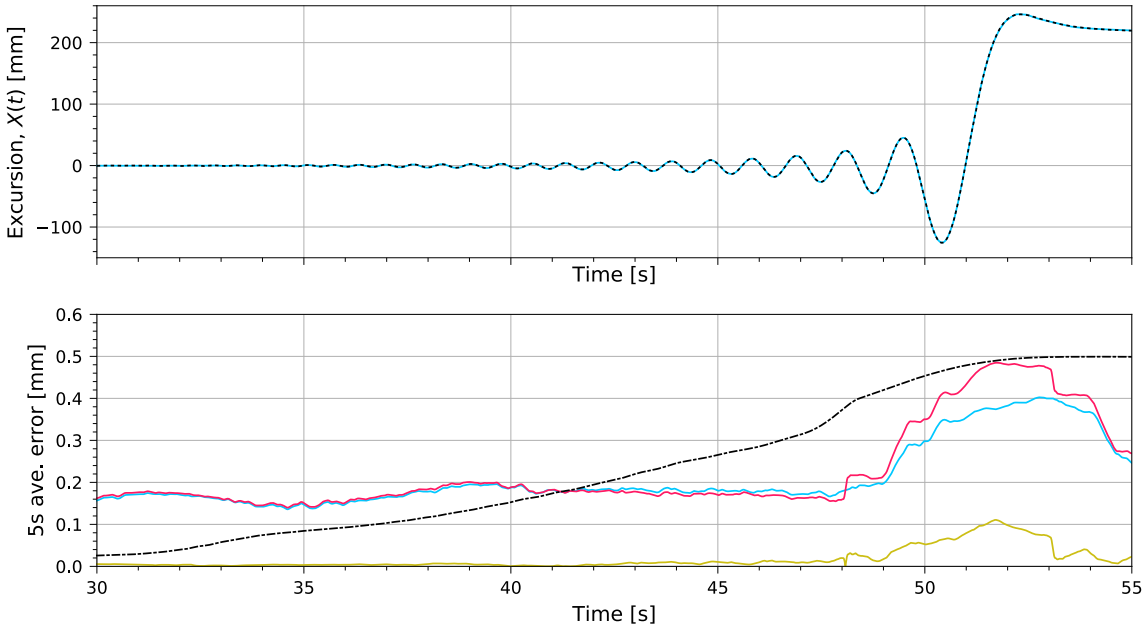

Figure 6.22: Five seconds average error of the paddle motion for waves C12-20-0 (——) and C12-20-1 (——) w.r.t the control signal (- - -). The maximum allowable five seconds average errors, Table 4.2, are also plotted (- · - · -). The difference of the wavemaker motion errors is included to check the variability of the error (——).

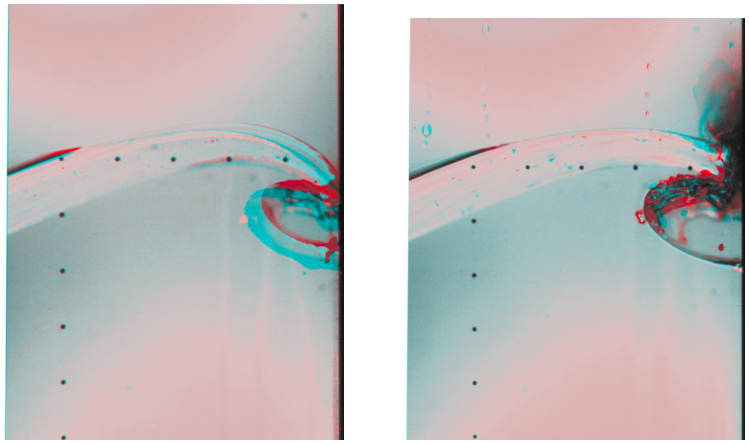

Figure 6.23: Impact moment of waves C12-06 (left) and C12-20 (right).

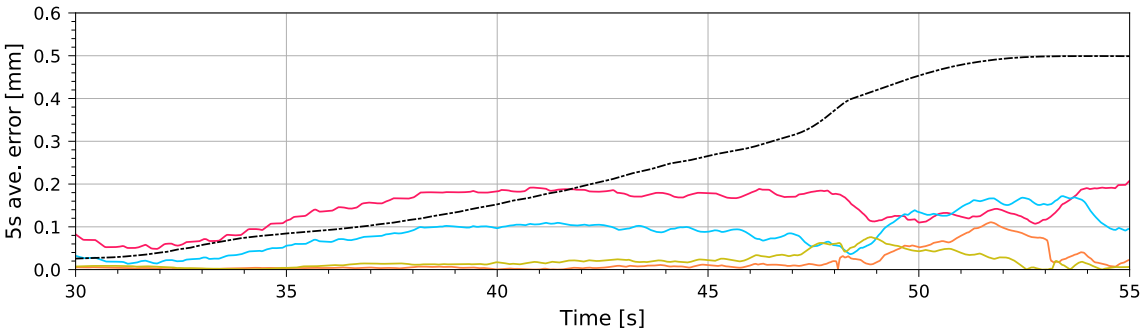

Figure 6.24: Wavemaker motion error between experiments as a function of the water depth difference. $\Delta h = 2.2\text{mm}$ (—), $\Delta h = 0.8\text{mm}$ (—), $\Delta h = 0.2\text{mm}$ (—), $\Delta h = 0.1\text{mm}$ (—).

further investigation of the experiments history showed that a third wave was actually run at 2.0bar before the presented ones. This effect is, therefore, self-explanatory. The waiting times between pressure changes were too long (approximately 40 minutes) which made the first wave of the two repetitions propagate on dry side walls. 20 minutes later, the second wave is generated and a thin layer of water (probably) remains on the side walls, so the effect does not occur. It is therefore recommended to run a dummy wave before the formal tests so that the effect disappears.

- It was observed that the wavemaker motion error is dependent on the water depth. Those experiments that were run at approximately the same water depth, $\Delta h < 0.2\text{mm}$, showed negligible paddle errors between experiments. See Figure 6.24 for a comparative of the wavemaker motion error as function of the water depth difference between experiments. On the other hand, the wavemaker error w.r.t. the control signal was, with no exception, larger than the design criteria set by MARIN. It is apparent that either the controller of the wavemaker or the proprietary method for the generation of correction files needs to be improved.

- Despite of the similarity parameter being highly affected by the wabbles in the free surface measurements, it is evident that provides a fast and easy method for the evaluation of global flow repeatability. In addition, it seems that the repeatability criteria theoretically derived, $Q_{\text{exp}} \leq 0.006$, is appropriate to discern repeatable and non-repeatable global flows in the MWL. As a matter of fact, undistinguishable global flows were obtained the only time the similarity parameter was below the limit, see Figure 6.23.

6.4.2 Wave C12 – different pressure

The wave shapes at absolute pressures $P_{\text{a}} = (0.4,\ 0.6,\ 1.7,\ 2.0)\text{bar}$ are depicted in Figure 6.26. Repetition 0 was chosen for all waves as they minimize the difference in water depth,

$\Delta h_{\max} = 0.9\mathrm{mm}$. Two trends can be observed in the figure: (1) the stability of the wave crest increases as the pressure (DR) drops, and (2) the size of the gas pocket increases with the pressure, consequence of the transfer of momentum liquid-gas as presented by Karimi et al. (2016). Regarding the effect of pressure in wave propagation, it is observed in Figure 6.25 that at $P_{\mathrm{a}} = 2.0\mathrm{bar}$ the wave train propagates slower than the waves at lower pressures—as the wave shapes are synchronized at the impact time it cannot be directly observed in the focused wave. This is not consequence of the water depth difference. In fact, the water depth is deeper at $P_{\mathrm{a}} = 2.0\mathrm{bar}$ which means that the wave is being delayed even when the water depth is increasing the propagation velocity of the wave train.

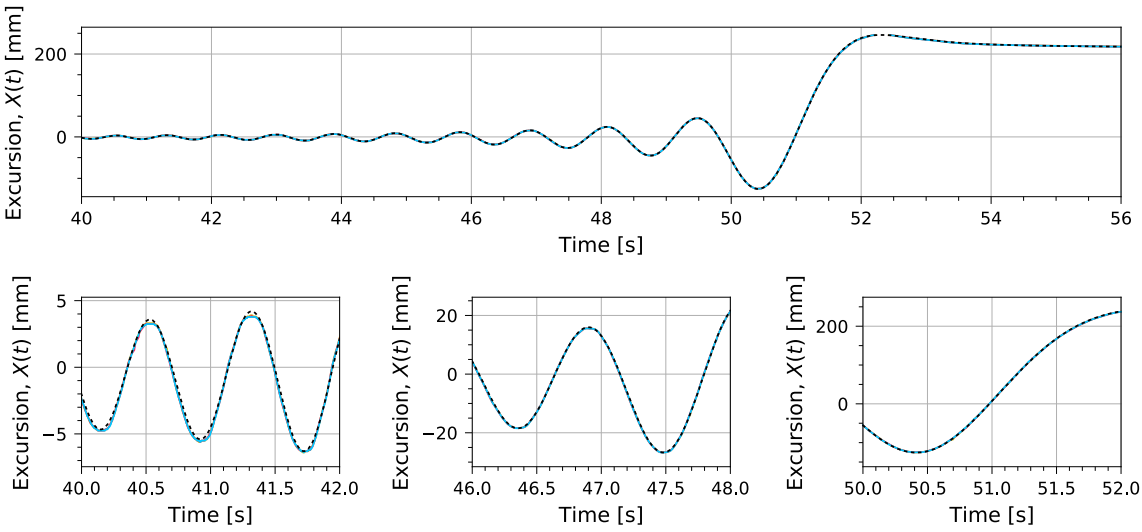

(a) Comparison of the wavemaker motion. Control signal (- - -). Δt(—)= $+1.840$s. Δt(—)= $+1.825$s. Δt(—)= $+1.798$s.

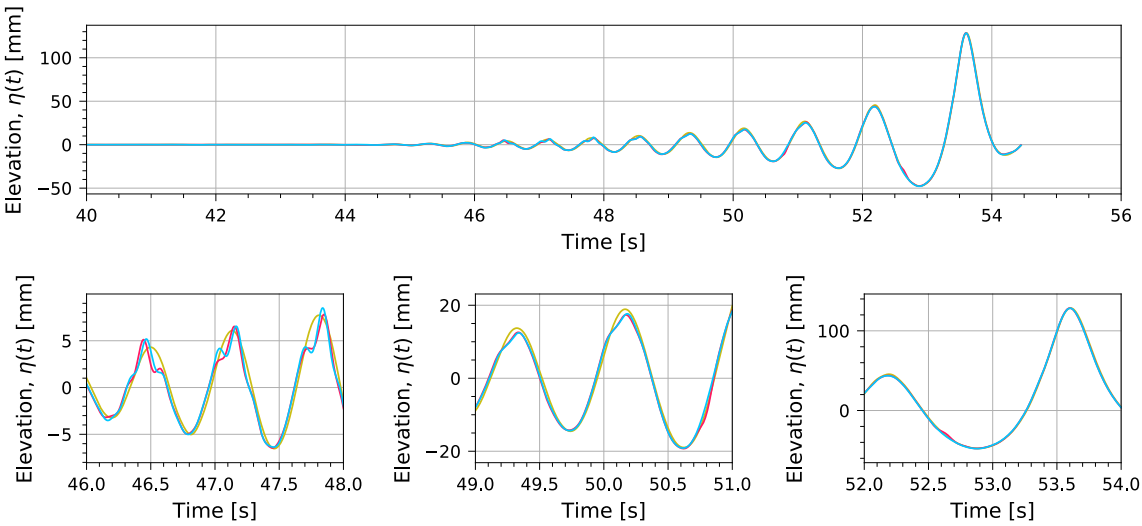

(b) Wave elevations at $x = -4.8$m. Q(—)= 0.010. Q(—)= 0.021.

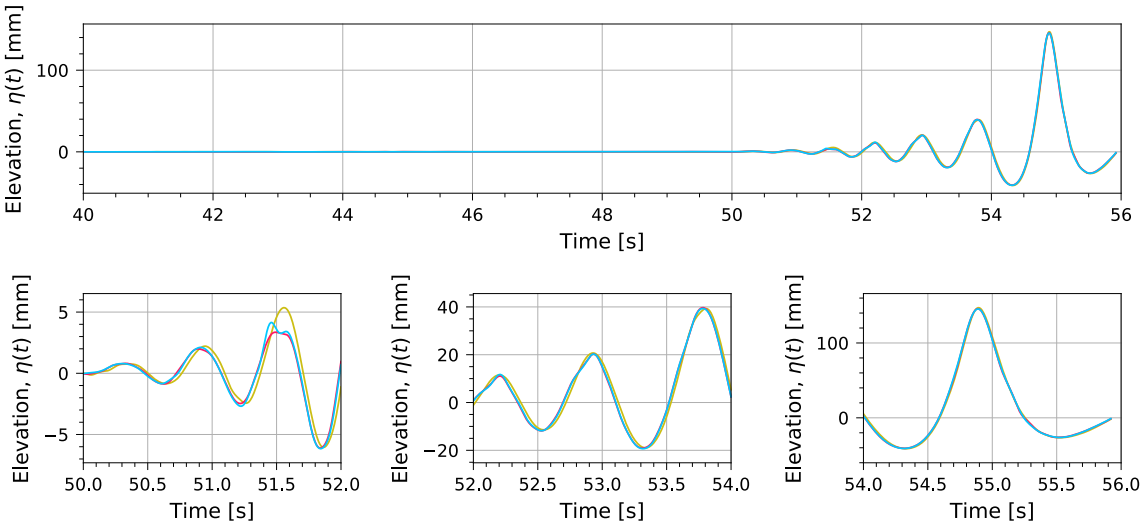

(c) Wave elevations at $x = -2.3$m. Q(—)= 0.007. Q(—)= 0.026.

Figure 6.25: Results for waves C12-04-0 (—), C12-06-0 (—) and C12-20-0 (—) at different pressures (there is no wave elevation data for wave C12-17-0).

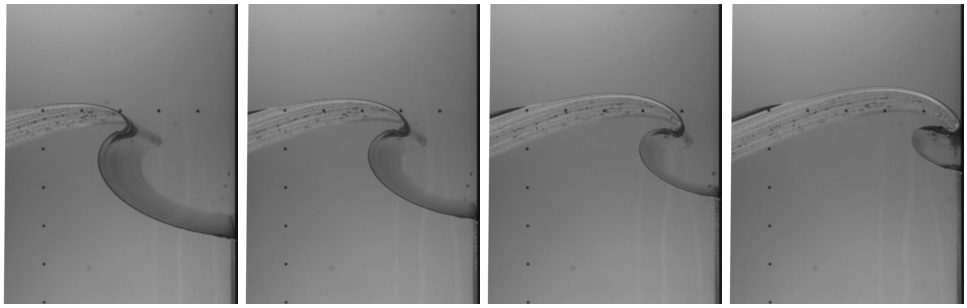

(a) C12-04-0

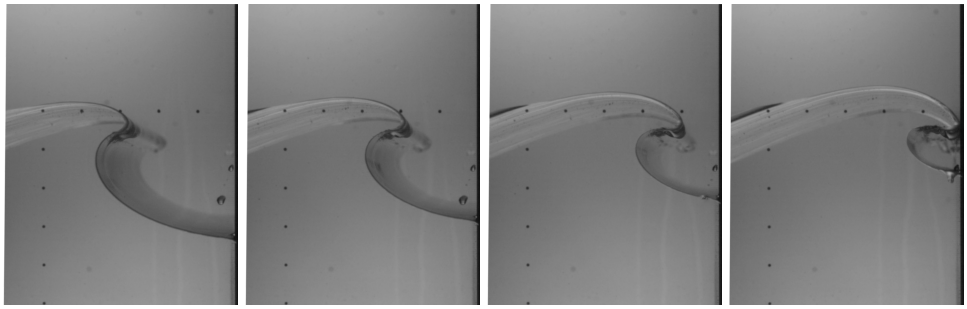

(b) C12-06-0

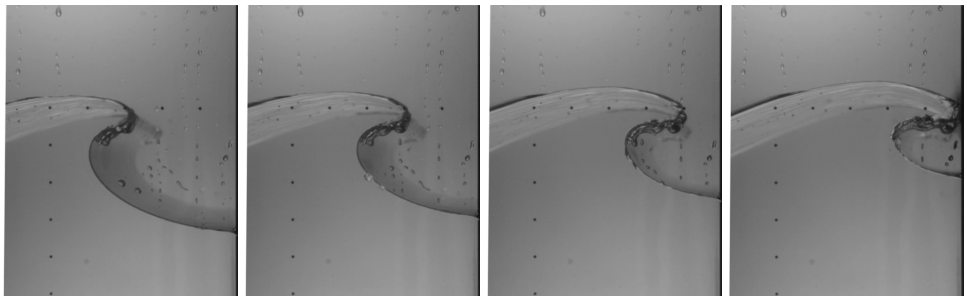

(c) C12-17-0

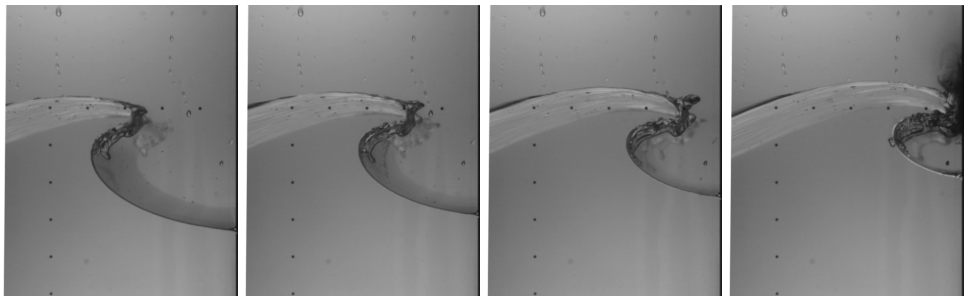

(d) C12-20-0

Figure 6.26: Wave shapes at different instances before impact ($\Delta t = 10\text{ms}$) for wave C12 at $P_\text{a} = (0.4,\ 0.6,\ 1.7,\ 2.0)\text{bar}$.

Chapter 7

Conclusions

In the LNG industry, particularly in the transportation of LNG overseas, wave impact test are performed to design the structure of the cargo containment system (CCS) of the vessels. The state-of-the-art methodology, based on a probabilistic approach, requires many repetitions of the test conditions to obtain a converged probability distribution of the load maxima, which are then compared to the structural capacity of the CCS. However, measurements taken by Lund-Johansen et al. (2011) on board of a $148.000\mathrm{m}^3$ LNG carrier showed that the methodology is globally conservative—the maximum expected pressure for a long period is larger than what is experience in reality—while the short term statistics showed that values at model scale are not always larger than at full scale.

In an investigation to better understanding the physics of wave impacts, Bogaert (2018) divided the flow into two parts: the global and local flow. The global flow being considered as the solution of the incompressible Euler equations for the liquid and gas in the tank; and the local flow as a perturbation of the global flow. The research was focused on the the local flow and its link to the impact pressures, and the structural response of the CCS. Nevertheless, the author found to be a challenge to generate repeatable global flows and, therefore, to determine the contribution of the variability of the local flow in the impact pressure variability. As a result, a new facility was designed and built in MARIN in the framework of the SLING project to further investigate the physics of sloshing impacts: the Multiphase Wave Lab (MWL).

In this context, this thesis aimed to identify and evaluate the sources of variability of the global flow. Based on a theoretical analysis of the variability introduced at different positions along the wave flume, a criterion to experimentally define global flow repeatability was derived from the Sobolev norm of the Fourier space of the free surface elevations at a distance from the focal point. By defining the criterion sufficiently far from the focal point, the local flow variability is assumed to be negligible and, in consequence, perfect repeatability of the wave elevations at these positions would result in the same global flows at the focal point. Wave impact tests were also performed to evaluate the validity of the mathematical model and the repeatability criterion. While more repetitions are required to confidently conclude about the validity of the criterion, the experimental results showed that when the 'dissimilarity' value was below the theoretical maximum, exceptional repeatability of the global flow before impact was obtained.

Section 7.1 summarizes the main conclusions of this thesis and section 7.2 provides recommendations for future research on the used techniques and procedures.

7.1 Main conclusions

In the course of the thesis, a series of assumptions and decisions have been made in the development of the theoretical model for the evaluation of the sources of variability, and in the development of the tools used to obtain the experimental measurements. This section summarizes the conclusions and findings of the parts in which the thesis is divided.

7.1.1 Wave focusing

The phase speed method and linear wave theory were used to to derive the wave train the wavemaker must generate to obtain a focused wave. The amplitude distribution of the frequencies was obtained from a modified Ricker spectrum formulation, which included two parameters that control the distribution of energy in the lower and higher frequencies. The resulting wavelet, suppresses the small leading and trailing waves typical from other spectrum shapes that produce reflections in the impact wall and that usually lead to early breaking of the wave front. Regardless of the simplicity of the method and the use of linear theory, good quality breaking waves were obtained, characterized by a smooth and round wave shape. Validation of the method showed that wave propagation velocity is accurately predicted while discrepancies in the amplitude of the wave train are obtained.

7.1.2 Wave generation

Linear wave making theory was used for the derivation of the wavemaker control signal from the free surface elevation at the wavemaker location. By using the Ricker amplitude spectrum formulation, the last part of the control signal resembles the solution of a solitary wave and, therefore, no tweaking was necessary to add energy to the last stroke like in Hofland et al. (2011). Nevertheless, the amplitude spectrum formulation is characterized by a non-zero amplitude of the zero frequency and, as consequence, the required number of wave components becomes larger, slightly increasing the computational cost. Validation of the model comparing the amplitude spectrum of the measurements w.r.t. Ricker amplitude spectrum showed a global shift of the spectrum towards higher frequencies, which is in accordance with higher order wave theories—real waves are characterized by a flatter trough and a sharper crest (higher frequencies).

7.1.3 Sources of variability

Variability was theoretically evaluated by systematically generating and propagating the wave train produced by a control signal over different water depths, currents and residual wave amplitudes. Wave repeatability was defined in function of the accuracy of the wavemaker. Two waves are considered repeatable when the sources of variability introduce a combined time-averaged error at the focal point smaller than the time-averaged error introduced by maximum wavemaker motion error. Theoretical results showed that the water depth difference between experiments must be kept below $\Delta h_{\max} \approx 0.45\mathrm{mm}$ to obtain repeatable results. On the other hand, the theoretical work showed that long bounded waves (seiching)—and their induced current—are less important in the generation of repeatable global flows. However, both are related since an accurate measurement of the water depth requires a still water free surface.

Since waves overturn at the focal point experimentally, the definition of the time-averaged error theoretically derived cannot be used. Thus, a similarity parameter based on the Sobolev norm of the Fourier space of the free surface elevations was used to derive the experimental repeatability criterion at the camera positions. The quotient, Q, sets the maximum error of the Fourier space of two signals to be considered repeatable. In the MWL, the maximum 'dissimilarity' value between two experiments is $Q_{\max} 0.006$.

7.1.4 Experimental results

In total 140 waves were generated during the the thesis. However, most of them were used for the commissioning of the different systems of the facility and, therefore, only 20 waves were meaningful for the evaluation of repeatability. These experiments ranged from $P_{\mathrm{a}} = 0.4\mathrm{bar}$ to $P_{\mathrm{a}} = 2.0\mathrm{bar}$ and three different waves were generated (C3, C12 and C13) with different wave shape characteristics.

The wavemaker motion and the free surface elevations at two positions along the flume were recorded with four slow speed cameras at $200\mathrm{Hz}$ with a synchronization uncertainty of $0.5\mathrm{ms}$, two cameras combined for the wavemaker and two for the wave elevations. Measurements were taken by means of image processing techniques with a resolution of $\Delta x \approx 0.09\mathrm{mm}$ for the wavemaker motion and $\Delta \eta \approx 0.2\mathrm{mm}$ for the wave elevations. The wavemaker position was detected using a cross correlation technique, which led to reliable measurements even in conditions were condensation in the observation windows were found. Getting the free surface elevations required a

combination of different techniques, being the core of the algorithm a Hough transform of the image to detect the free surface line. Due to meniscus/surface tension effects, some 'misdetections' occurred, apparently when the waiting times between experiments were too large, though the real cause must be further investigated.

The analysis of the data showed that, when the difference in water depth between experiments was above $\Delta h_{\max}$, the values of the similarity parameter, Q, were above the maximum 'dissimilarity' value. Recordings from the high speed cameras at the moment of impact show that, indeed, when $Q_{\exp} > Q_{\max}$ relatively large differences are obtained and the global flow of the waves is not repeatable. However, the similarity parameter was below the maximum value when the water depth difference was kept below $\Delta h_{\max}$, resulting in undistinguishable global flows, although more repetitions are required to confidently state that the repeatability criterion $Q_{\max} = 0.006$ is appropriate to discern between repeatable and non-repeatable global flows in the MWL. The results also showed dependency of the wavemaker error in the water depth. In those experiments where the differences in water depth was $\Delta h < 0.2\mathrm{mm}$, the error in the wavemaker motion between experiments was negligible, whereas errors larger than the design acceptance errors were obtained when the difference in water depth was larger.

7.2 Recommendations

While the thesis has been focused in the investigation of the sources of variability and the repeatability of the global flow in wave impact tests, the research also required to gain knowledge in wave generation and image processing techniques. In this section, a series of recommendations based on the findings and challenges encountered are given.

Regarding wave generation and propagation, linear theory was found to be sufficient to obtain focused waves and accurately predict their focal time. Nevertheless, the experimentally measured amplitude spectrum differs from the theoretical amplitude spectrum. For the case of wave impacts, the relevance of the amplitude spectrum is not that important as long as wave focusing occurs. If the application requires the generation of a specific spectrum, a higher order wave/wavemaking theory must be used.

With respect to the image processing algorithm developed to detect and measure the free surface elevations, the technique currently used led to some misdetections when the meniscus 'stuck' to the glass panel in the transition from wet to dry glass, leading to a deviation of the elevations at the wave crests which increases the similarity parameter Q. From the experiments, it was found that these misdetections always occurred in the first repetition at each condition, suggesting that when the waiting times are too large the glass panels dry out and the effect is found. The recommendations are: (1) to develop an algorithm that detects the free surface elevation at a position not affected by the surface tension effects of the meniscus, or (2) to keep the waiting times between experiments uniform and, if longer waiting times are required due to a change in the autoclave conditions, a dummy test wave must be generated before taking any measurement.

About the wavemaker motion error, it was observed that the wavemaker error w.r.t. the control signal was, with no exception, larger than the design acceptance values set by MARIN. Thus, either the controller of the wavemaker or the method for the generation of correction files (or both) need to be improved. However, the error was found to be dependent on the water depth and, when the differences in water depth were insignificant, the wavemaker motion error between experiments was negligible. Therefore, while the wavemaker performance is not as good as designed, keeping the water depth carefully controlled allows to reduce the importance of the wavemaker motion errors.

Bibliography

M. Basu. Gaussian-based edge-detection methods-a survey. *IEEE Transactions on Systems, Man, and Cybernetics, Part C (Applications and Reviews)*, 32(3):252–260, 2002.

H. Bogaert. *An experimental investigation of sloshing impact physics in membrane LNG tanks on floating structures*. PhD thesis, Delft University of Technology, 12 2018.

G. Bradski. The OpenCV Library. *Dr. Dobb's Journal of Software Tools*, 2000.

L. Eça and M. Hoekstra. Verification and validation for marine applications of cfd. *International Shipbuilding Progress*, 60(1-4):107–141, 2013.

L. Eça and M. Hoekstra. A procedure for the estimation of the numerical uncertainty of cfd calculations based on grid refinement studies. *Journal of Computational Physics*, 262:104–130, 2014.

C. Eckart. The approximate solution of one-dimensional wave equations. *Reviews of Modern Physics*, 20(2):399, 1948.

S. Etienne, Y.-M. Scolan, and L. Brosset. Numerical study of density ratio influence on global wave shapes before impact. In *ASME 2018 37th International Conference on Ocean, Offshore and Arctic Engineering*. American Society of Mechanical Engineers Digital Collection, 2018.

J. Fenton. Nonlinear wave theories. *The Sea-Ocean Engineering Science*, 9:3–25, 1990.

H. Fernández, S. Venkatachalam, S. Schimmels, M. Budzik, and H. Oumeraci. Focused wave generation in laboratory flumes over uneven bottom. *Coastal engineering*, 2014.

C. J. Galvin Jr. Wave-height prediction for wave generators in shallow water. Technical report, COASTAL ENGINEERING RESEARCH CENTER VICKSBURG MS, 1964.

E. Gervaise, P.-E. de Sèze, S. Maillard, et al. Reliability-based methodology for sloshing assessment of membrane lng vessels. *International Journal of Offshore and Polar Engineering*, 19 (04), 2009.

M. C. Haller and R. A. Dalrymple. Rip current instabilities. *Journal of Fluid Mechanics*, 433: 161–192, 2001.

N.-E. O. Hansen, S. E. Sand, H. Lundgren, T. Sorensen, and H. Gravesen. Correct reproduction of group-induced long waves. In *Coastal Engineering 1980*, pages 784–800. 1980.

T. Havelock. Forced surface-wave on water. *Philosophical Magazine*, VIII:569–576, 1929.

T. Hedges. An empirical modification to linear wave theory. *Proc. Inst. Civ. Eng*, 61(3):575–579, 1976.

T. Hedges and Ursell. Regions of validity of analytical wave theories. *Proceedings of the Institution of Civil Engineers-Water Maritime and Energy*, 112(2):111–114, 1995.

B. Hofland, M. Kaminski, and G. Wolters. Large scale wave impacts on a vertical wall. volume 1, 02 2011.

L. H. Holthuijsen. *Waves in oceanic and coastal waters*. Cambridge university press, 2010.

John R. Chaplin. On Frequency-Focusing Unidirectional Waves. *International Journal of Offshore and Polar Engineering*, (June), 1996. ISSN 1053-5381.

M. Karimi, L. Brosset, J.-M. Ghidaglia, and M. Kaminski. Effect of ullage gas on sloshing, part ii: Local effects of gas–liquid density ratio. *European Journal of Mechanics-B/Fluids*, 57:82–100, 2016.

O. Kimmoun, A. Ratouis, and L. Brosset. Sloshing and scaling: Experimental study in a wave canal at two different scales. *Proceedings of the International Offshore and Polar Engineering Conference*, 3:33–43, 01 2010.

J. T. Kirby and R. A. Dalrymple. An approximate model for nonlinear dispersion in monochromatic wave propagation models. *Coastal Engineering*, 9(6):545–561, 1986.

H. Lamb. On water waves due to disturbance beneath the surface. *Proceedings of the London Mathematical Society*, 2(1):359–372, 1923.

B. Le Méhauté. *An introduction to hydrodynamics and water waves*. Springer Science & Business Media, 2013.

Z. Liu, N. Zhang, and Y. Yu. An efficient focusing model for generation of freak waves. *Acta Oceanologica Sinica*, 30(6):19–26, 2011.

Ø. Lund-Johansen, T. Østvold, C. Berthon, and K. Pran. Full scale measurements of sloshing in lng tanks. *Proceedings of Gastech*, 2011.

C. C. Mei. *The applied dynamics of ocean surface waves*, volume 1. World scientific, 1989.

M. Miche. Mouvements ondulatoires de la mer en profondeur constante ou décroissante. *Annales de Ponts et Chaussées, 1944, pp (1) 26-78,(2) 270-292,(3) 369-406*, 1944.

M. Perlin and M. D. Bustamante. A robust quantitative comparison criterion of two signals based on the sobolev norm of their difference. *Journal of Engineering Mathematics*, 101(1):115–124, 2016.

A. B. Rabinovich. Seiches and harbor oscillations. In *Handbook of coastal and ocean engineering*, pages 193–236. World Scientific, 2010.

P. J. Roache. *Verification and validation in computational science and engineering*, volume 895. Hermosa Albuquerque, NM, 1998.

W. Rong, Z. Li, W. Zhang, and L. Sun. An improved canny edge detection algorithm. In *2014 IEEE International Conference on Mechatronics and Automation*, pages 577–582. IEEE, 2014.

H. A. Schäffer. Second-order wavemaker theory for irregular waves. *Ocean Engineering*, 23(1): 47–88, 1996.

L. W. Schwartz. Computer extension and analytic continuation of stokes' expansion for gravity waves. *Journal of Fluid Mechanics*, 62(3):553–578, 1974.

H. N. Southgate. Wave breaking-a review of techniques for calculating energy losses in breaking waves. 1988.

K. Spinka IV, L. Morissette, and N. Zemlak. Digital image processing using matlab. 2009.

J. Spinneken and C. Swan. Second-order wave maker theory using force-feedback control. part i: A new theory for regular wave generation. *Ocean Engineering*, 36(8):539–548, 2009.

W. Sulisz and R. Hudspeth. Complete second-order solution for water waves generated in wave flumes. *Journal of Fluids and Structures*, 7(3):253–268, 1993.

C. Swan. Convection within an experimental wave flume. *Journal of Hydraulic Research*, 28(3): 273–282, 1990.

S. Unoki and M. Nakano. On the cauchy-poisson waves caused by the eruption of a submarine volcano (iii). *Papers in Meteorology and Geophysics*, 4(3-4):139–150, 1953.

M. J. G. van den Boomgaard. Wave focussing in a laboratory flume. Master's thesis, Delft University of Technology, 2003.

S. S. van der Walt. Chris colbert and gaël varoquaux. *The NumPy Array: A Structure for Efficient Numerical Computation, Computing in Science & Engineering*, 13:22–30, 2011.

S. Wang, B. le Mehaute, and C. C. Lu. Effect of dispersion on impulsive waves. *Marine Geophysical Researches*, 9(1):95–111, 1987. ISSN 00253235. doi: 10.1007/BF00338252.

Y. Wang. Frequencies of the ricker wavelet. *GEOPHYSICS*, 80:A31–A37, 02 2015.

B. Wilson. Seiches. advances in hydrosciences, 8, 1972.